Multiscale modelling and simulation of slip boundary conditions at fluid-solid interfaces

Thanh Tung Pham

To cite this version:

Thanh Tung Pham. Multiscale modelling and simulation of slip boundary conditions at fluid-solid interfaces. Other. Université Paris-Est, 2013. English. NNT : 2013PEST1138 . tel-00980155

HAL Id: tel-00980155
https://theses.hal.science/tel-00980155

Submitted on 17 Apr 2014

Université PARIS-EST
École doctorale : Sciences, Ingénierie et Environnement

THÈSE
pour obtenir le grade de
Docteur de l'Université PARIS-EST

Spécialité : Mécanique des fluides

Thanh Tung PHAM

Multiscale modelling and simulation of slip boundary conditions at fluid-solid interfaces

Thèse dirigée par Guy LAURIAT et Quy Dong TO

Date de soutenance : le 25 Septembre 2013

Membres du jury :

Guillaume Galliéro	Professeur	Univ. de Pau	Rapporteur
Guy Lauriat	Professeur	Univ. Paris-Est MLV	Directeur de thèse
Céline Léonard	Professeur	Univ. Paris-Est MLV	Examinateur
Irina Martin Graur	Professeur	Univ. d'Aix-Marseille	Rapporteur
Bernard Rousseau	Dir. Recherche CNRS	Univ. Paris-Sud 11	Président
Quy Dong To	M. de Conférence	Univ. Paris-Est MLV	Examinateur

A mes chers parents,
Dinh Hue et Nguyet Hoa.

Remerciements

Ce travail de thèse a été réalisée au sein du laboratoire Modélisation et Simulation Multi Echelle (UMR 8208 CNRS) de l'université Paris-Est et il n'aurait probablement jamais été mené à terme sans le soutien d'un grand nombre de personnes que je tiens vivement et très sincèrement à remercier.

Je commencerai d'abord par remercier Monsieur Guy Lauriat qui a dirigé cette thèse dans la continuité de mon stage de master. La pleine confiance qu'il m'a accordée dès le début m'a permis de progresser régulièrement. Je voudrais aussi le remercier pour le temps qu'il m'a consacré et la patience avec laquelle il a accompagné mon travail.

Je remercie particulièrement Monsieur Quy Dong To, mon co-encadrant de thèse, pour sa grande contribution à ce travail, son soutien, sa bonne humeur ainsi que l'amitié qu'il m'a témoignée tout au long de ces trois années.

Je voudrais également remercier Madame Céline Léonard pour sa collaboration sur la partie de la Chimie théorique de ma thèse et son aide en général.

Je tiens à remercier les membres du jury, M. Bernard Rousseau, M. Guillaume Galliéro et Mme. Irina Martin Graur pour avoir accepté d'évaluer mes travaux et de siéger à ma soutenance de thèse. Je les remercie de plus de leurs remarques positives et constructives.

J'adresse mes chaleureux remerciements à l'ensemble des membres du personnel du laboratoire MSME pour m'avoir offert un cadre et une atmosphère de travail agréable. Merci également à mes camarades de l'équipe TCM : Thanh Long, Chahinez, Benoît, Paulin, Li, ... pour leur bonne humeur et leur gentillesse.

Ma reconnaissance et mon affection totales vont à mes chers parents pour tout leur amour, leur soutien inconditionnel et leurs encouragements tout au long de ma scolarité. Ils ont toujours su dire le bon mot au bon moment et je ne les en remercierai jamais assez. Merci à mes soeurs pour leurs aides et pour les bons moments passés ensemble quand on peut se retrouver. En particulier, merci à Mai Anh, ma copine pour son amour et sa bonne humeur et tout ce qui fait qu'elle me rend la vie plus simple et belle.

Contents

Résumé

Dans les systèmes micro ou nano-fluidiques, le glissement de vitesse à l'interface fluide-parois est un phénomène important. Pour modéliser cet effet à l'échelle macroscopique, les conditions aux limites de Navier ont été introduites, avec la longueur de glissement comme paramètre. Lorsque le fluide est un gaz, cette longueur est liée au coefficient d'accommodation tangentiel (TMAC) et au libre parcours moyen, selon le modèle de Maxwell. Le but de ce travail est de traiter systématiquement ce modèle par une approche multi-échelle et de l'étendre en incorporant la morphologie et l'anisotropie de la surface.

La thèse est composée de cinq chapitres.

Après l'Introduction, les notions de base de la théorie cinétique des gaz, l'équation de Boltzmann et les solutions associées (Navier-Stokes-Fourier, Burnett, Grad, Direct Simulation Monte Carlo...) sont rappelées dans le Chapitre 1. Les modèles d'interaction gaz-paroi ainsi que les modèles de glissement introduits dans le cadre de la mécanique des fluides sont aussi rappelés. Le chapitre se termine par la description de la méthode de calcul par dynamique moléculaire (MD) utilisée dans ce travail.

Le Chapitre 2 est dédié au développement d'une technique simple afin de simuler les écoulements induits par la pression. Le principe est de se baser sur les formules atomistiques du tenseur des contraintes (Irving Kirkwood, Méthode de Plan, Contraintes Virielles) et de modifier les conditions périodiques, tout en maintenant la différence entre l'énergie cinétique des atomes à l'entrée et à sortie du domaine de calcul. Plusieurs types de conduite sont étudiés avec cette technique. Les résultats (température, vitesses...) sont discutés et comparés.

Le Chapitre 3 concerne l'étude du potentiel d'interaction gaz-paroi par la méthode ab-initio. Le code CRYSTAL 09 est utilisé pour obtenir le potentiel entre un atome d'argon (Ar) et une surface de platine (Pt) <111> en fonction de la distance. Ensuite, le potentiel atome/surface est décomposé en potentiel binaire et approché par une fonction analytique. Cette fonction est ensuite implémentée dans un code MD pour simuler les collisions gaz-paroi et déterminer le coefficient TMAC.

Dans le Chapitre 4, l'effet de morphologie est étudié. Le potentiel multi-corps Quantum Sutton Chen (QSC) est utilisé pour le solide Pt <100> et un des potentiels binaires étudié dans le chapitre précédent pour le couple Ar-Pt. Le potentiel QSC est nécessaire pour reproduire l'effet de surface qui affecte le résultat final. Différentes surfaces sont traitées : surface lisse, surface nanostructurée, surface aléatoire obtenue par déposition de vapeur (CVD). Le coefficient TMAC est déterminé de façon généralisée, c.à.d en fonction de l'angle du flux d'atomes incidents sur la surface. Les anisotropies de surface et le noyau

de collision sont également examinés.

Dans le Chapitre 5, on propose un modèle de glissement anisotrope pour les fluides en fonction du tenseur d'accommodation. Le modèle est obtenu par les calculs analytiques approchés développés dans le cadre de la théorie cinétique. On a ainsi généralisé l'équation de Maxwell en montrant que le tenseur de longueur de glissement est directement lié au tenseur d'accommodation. Le modèle est en bon accord avec les résultats de la méthode MD. Concernant la simulation MD, on a développé une technique pour reproduire l'anisotropie du tenseur d'accommodation.

Le mémoire de thèse se termine par une synthèse des résultats obtenus. Des perspectives pour de futures études sont proposées.

Abstract

In most applications concerning a fluid flowing over a solid surface, the no-slip velocity condition was widely used because it is simple and produces the results in agreement with experiments. However, this dynamical boundary condition is not appropriate when the flow under consideration is at a micro or nano length scale. In order to model this effect at the macroscopic scale, the Navier boundary conditions have been introduced, with the slip length as a parameter. When the fluid is a gas, this length is related to the tangential momentum accommodation coefficient (TMAC) and the mean free path, according to the Maxwell model. The aim of this work is to systematically address this model using a multi-scale approach and to extend it by incorporating both the morphology and the anisotropy of a surface.

The thesis consists of five chapters.

In Chapter 1, the basics of the kinetic theory of gases, the Boltzmann equation and related solutions (Navier-Stokes-Fourier, Burnett, Grad, Direct Simulation Monte Carlo ...) are briefly presented. The models of gas-wall interaction and slip models introduced in the fluid mechanics are also recalled. The chapter ends with a description of the computational method used for the molecular dynamics simulations performed in this work.

Chapter 2 is dedicated to the development of a simple technique to simulate the pressure driven flows. The principle is to rely on the atomistic formulas of the stress tensor (Irving Kirkwood, Method of Plane, Virial Stress) and to modify the periodic conditions by maintaining the difference between the kinetic energy of the ingoing and outgoing particles of the simulation domain. Several types of channels are studied with this technique. The results (temperature, velocity ...) are discussed and compared.

Chapter 3 deals with the study of the gas-wall interaction potential by the ab-initio method. The code CRYSTAL 09 is used to obtain the potential between an atom of argon (Ar) and a surface of platinum Pt(111) as a function of distance. Then the gas-wall potential is decomposed into binary potential and approached by an analytic function. This function is then implemented in a MD code to simulate the gas-wall collisions and determine the TMAC coefficient. In Chapter 4, the effect of morphology is studied. The multi-body Quantum Sutton Chen (QSC) potential is used for Pt(100) solid and the binary potential proposed in the previous chapter for the Ar-Pt couple is employed. The QSC potential is needed to reproduce the surface effects that affect the final results. Different surfaces are treated : smooth, nanostructured surface and, random surface obtained by Chemical vapor deposition (CVD). The TMAC is determined using a generalized approach, i.e. depending on the angle of incident flux of gas atoms on the surface. The surface anisotropy and the scattering kernel are also examined.

In Chapter 5, we propose a model of anisotropic slip for fluids based on accommodation tensor. The model is obtained by the analytical approximate calculations developed in the framework of the kinetic theory. We thus generalize Maxwell's equation by showing that the slip length tensor is directly related to the accommodation tensor. The model is in good agreement with the MD results. Thanks to our MD simulations, we develop a suitable technique for reproducing the anisotropy of the accommodation tensor .

The thesis ends with a conclusion section in which we suggest some perspectives for a continuation of this work.

Nomenclature

$B(\mathbf{v}', \mathbf{v})$	scattering kernel $[d.u.]$
$\mathbf{b}$	slip length tensor $[m]$
C_p, C_v	heat specific at constant pressure and volume $[J.K^{-1}.Kg^{-1}]$
C_1, C_2	first and second order slip coefficients $[d.u.]$
$\bar{c}$	thermal speed $[m.s^{-1}]$
D_e	dissociation energy parameter $[J]$
E_p, E_c	potential and kinetic energy $[J]$
Ec	Eckert number $[d.u.]$
$\mathbf{e}_r$	unit normal vector of surface element dS_r $[d.u.]$
$\mathbf{F}$	external force $[Kg.m.s^{-2}]$
$f(\mathbf{x}, \mathbf{v}, t)$	probability density function $[d.u.]$
f_0	Maxwellian distribution function $[d.u.]$
$I(v_r, \Omega)$	differential cross section of the collision $[m^2]$
Kn	Knudsen number $[d.u.]$
k_B	Boltzmann constant, $k_B = 1.3806503 \times 10^{-23}$ $[Kg.m^2.s^{-2}.K^{-1}]$
k_w	rigidity of harmonic springs $[Kg.s^{-2}]$
L_s	slip length $[m]$
L, B, H	length, width and height of the channel $[m]$
l, h	length and height of the wall rib $[m]$
$\mathbf{M}$	surface mobility tensor $[d.u.]$
m	molecular mass $[Kg]$
$\mathbf{N}$	accommodation tensor in the current basis Oxy $[d.u.]$
Pr	Prandtl number $[d.u.]$
$\mathbf{Q}(\varphi)$	rotation transformation matrix
Q	molecular physical quantities
$\overline{Q}$	macroscopic physical quantities
Re	Reynolds number $[d.u.]$
r_{ij}	distance between particles i and j $[m]$
r_c	cut-off radius $[m]$
r_v	Verlet radius $[m]$
S_r	cross surface $[m^2]$
T	Temperature $[K]$
t	time $[s]$
$\mathbf{u}$	stream velocity $[m.s^{-1}]$
$\mathbf{u}_s$	slip velocity tensor $[m.s^{-1}]$
V	interaction energy $[J]$
$\mathbf{v}(v_1, v_2, v_3)$	velocity space $[m.s^{-1}]$
$\mathbf{v}_i$, $\mathbf{v}_r$	incident and reflected velocity $[m.s^{-1}]$
$\mathbf{x}(x_1, x_2, x_3)$	physical space $[m]$
(x, y, z)	cartesian coordinate $[m]$

Greek symbols

$\alpha_x, \alpha_y, \alpha_z$	momentum accommodation coefficients along x, y, z axes$[d.u.]$
δt	time step $[s]$
$d\Omega$	solid angle $[sr]$
ϵ	depth of the potential well $[J]$
η	viscosity $[Kg.m^{-1}.s^{-1}]$
$\boldsymbol{\gamma}$	external force field $[Kg.m.s^{-2}]$
κ	thermal conductivity $[W.m^{-1}.K^{-1}]$
λ	mean free path $[m]$
μ_i	percentage of the elementary kernel B_i $[d.u.]$
Φ^-, Φ^+	incoming and outcoming flux at the wall
$\psi_1, \psi_2, ...$	functions in Chapman and Enskog model
ω	vertical harmonic vibrational frequency $[J]$
ρ	number density $[m^{-3}]$
σ	distance at which the inter-particle potential is zero in Lennard Jones potential $[m]$
σ_t	tangential momentum accommodation coefficient $[d.u.]$
σ_n	normal momentum accommodation coefficient $[d.u.]$
σ_T	energy accommodation coefficient $[d.u.]$
$\boldsymbol{\tau}$	shear stress vector $[Pa]$
θ, ϕ	zenithal and azimuthal angles $[rad]$
ξ	damping coefficient in Langevin equation $[d.u.]$

Indices

an	effective anisotropic
dir	directional
e	equilibrium
fcc	face centered cubic
g	gas
i, j	particles
iso	effective isotropic
s	solid
w	wall
$+$, $-$	upper and lower walls

Special symbols

$\langle . \rangle$	ensemble average
$\otimes$	dyadic product

Introduction

Over the past decades, micro/nanofluidic systems have developed rapidly as the result of continuous progresses in micro/nanofabrication technologies. Such systems contribute to a technological revolution in many areas such as the cooling of electronic components, micro electro mechanical systems (MEMS), biotechnology and medicines. One of the most successful commercial application of microfluidics is the inkjet printhead which consist of an ink reservoir fabricated from silicon, a heating element to drive the fluid, and a nozzle (Fig. 1). Droplets created by this system is generally about 50 μm. According to Tabeling, tens of millions of inkjet printers use MEMS and billions of documents are written and read thanks to microfluidics [1].

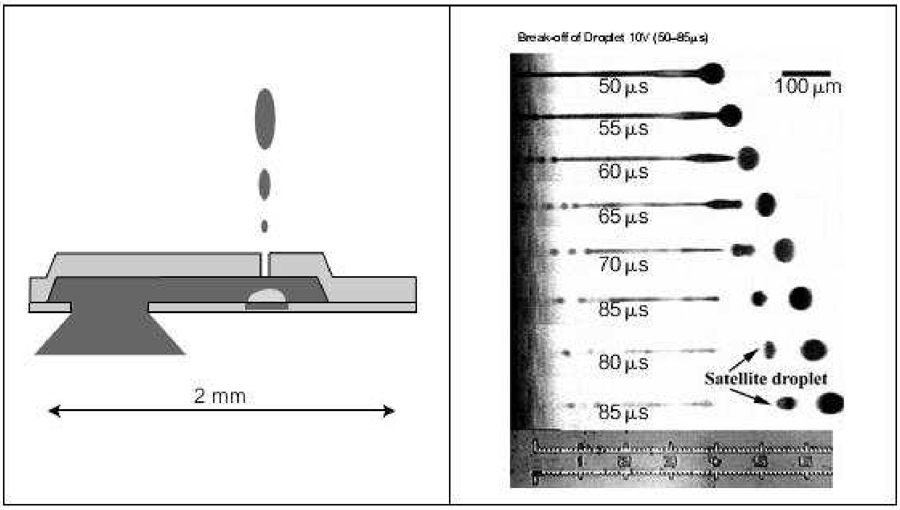

Figure 1: An inkjet printhead (left) and the visualization of droplets of ink projected onto a target (right) [1], [2].

Another examples of microfluidic systems which can be found in computer science, mechanical and chemical engineering are chemostats, pumps, conducts, mixers, filters, and valves (Fig. 2). Besides, the actual technologies permit also the construction of microdevices containing multiple components with different functionalities. A single integrated chip could perform many works concerning the biological or chemical processing from the sampling, pre-processing, and measurement in an assay. This leads to save time and reduce the reagent consumption. Nowadays, lab-on-a-chip devices are used for abundant fields including analysers of air and water quality, diagnostics of illnesses, and devices that replace many functions of components of human body. The economic possibilities of this field have been estimated at tens of billions of dollars per year [1].

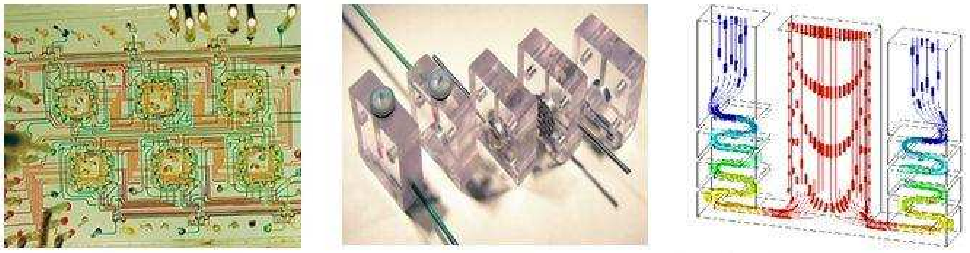

μ-chemostat μ-pump μ-conduct

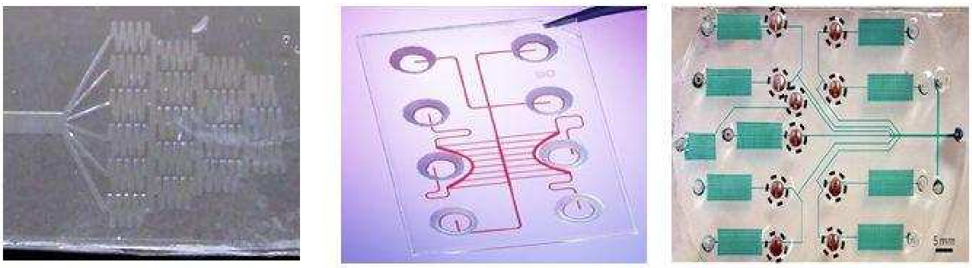

μ-mixer μ-filter μ-valve

Figure 2: Examples of micro/nanofluidic systems.

Figure 3: This chip is commercialized by Agilent Technologies and permits the identification of specific genetic sequences in a 1-μl sample of roughly purified DNA. The process time is just about 10 min [1].

As many investigators pointed out, physics that apply to nanotechnology scale is different from that on a human scale. Indeed, in the macroscopic scale, the surface/volume ratio is on the order of unity while in nanoscale, it rises to nearly a million. Such large ratios allow the surface effects dominate the physics and quantum effects begin to show and thus become important. The understanding of these physical effects at such small scales is therefore a vital interest in the manufacture and use of micro/nano electrodynamic systems.

At the same time, improvements in the numerical modeling are also needed to analyze the reliability of the systems. Depending on the nature of the problem, there are different suitable computational methods, such as those based on the Navier-Stokes and energy equations, the Burnett or Super Burnett models [3–5], or the molecular simulations. In the great family of molecular simulation methods, this is the Monte-Carlo method, which first appeared in 1953 with the work of Metropolis *et al.* [6]. This method is purely statistical and is well suited to the study of thermodynamic properties. The method is to successively change the movement of molecules randomly following a conditional probability by the thermodynamic state of the considered system. However, the classic Monte-Carlo method does not allow to study the dynamic aspects of systems. First proposed by Alder et Wainwrigth [7] in 1957 , the molecular dynamics (MD) simulation can overcome this obstacle. In general, there are two main types of MD simulation, which can be distinguished according to the way of interaction forces calculations. In *classical* MD simulations, the interaction forces are derived from the fixed empirical potentials, while in *ab initio* MD simulations, the quantum nature of the chemical bond is explicitly taken into account and the interaction forces are determined from the quantum chemistry. By integrating the equations of motion at time t, the molecular dynamics allows to evolve over time a system of particles defined by their positions, velocities and accelerations. As the user desires, the molecular properties can be sampled, averaged, and used to compute flow quantities, such as velocity, density, and viscosity. For micro/nanoflows, the MD method is one of the most accurate method since realistic interactions between particles or between particles and boundaries may be accounted for.

In most applications concerning a fluid flowing over a solid surface, the no-slip velocity condition was widely used because it is simple and produces the results in agreement with experiments. However, this dynamical boundary condition is not appropriate when the flow under consideration is at a micro or nano length scale. In order to model this effect at the macroscopic scale, the Navier boundary conditions have been introduced, with the slip length as a parameter. When the fluid is a gas, this length is related to the tangential momentum accommodation coefficient (TMAC) and the mean free path, according to the Maxwell model. The aim of this work is to systematically address this model using a multi-scale approach and to extend it by incorporating both the morphology and the anisotropy of a surface.

The thesis consists of five chapters.

In Chapter 1, the basics of the kinetic theory of gases, the Boltzmann equation and related solutions (Navier-Stokes-Fourier, Burnett, Grad, Direct Simulation Monte Carlo ...) are briefly presented. The models of gas-wall interaction and slip models introduced in the fluid mechanics are also recalled. The chapter ends with a description of the computational method used for the molecular dynamics simulations performed in this work.

Chapter 2 is dedicated to the development of a simple technique to simulate the pressure driven flows. The principle is to rely on the atomistic formulas of the stress tensor (Irving Kirkwood, Method of Plane, Virial Stress) and to modify the periodic conditions by maintaining the difference between the kinetic energy of the ingoing and outgoing particles of the simulation domain. Several types of channels are studied with this technique. The results (temperature, velocity ...) are discussed and compared.

Chapter 3 deals with the study of the gas-wall interaction potential by the ab-initio method. The code CRYSTAL 09 is used to obtain the potential between an atom of argon (Ar) and a surface of platinum (Pt)$\langle 111 \rangle$ as a function of distance. Then the gas-wall potential is decomposed into binary potential and approached by an analytic function. This function is then implemented in a MD code to simulate the gas-wall collisions and determine the

TMAC coefficient.

In Chapter 4, the effect of morphology is studied. The multi-body Quantum Sutton Chen (QSC) potential is used for Pt $\langle 100 \rangle$ solid and the binary potential proposed in the previous chapter for the Ar-Pt couple is employed. The QSC potential is needed to reproduce the surface effects that affect the final results. Different surfaces are treated : smooth, nanostructured surface and, random surface obtained by Chemical vapor deposition (CVD). The TMAC is determined using a generalized approach, i.e. depending on the angle of incident flux of gas atoms on the surface. The surface anisotropy and the scattering kernel are also examined.

In Chapter 5, we propose a model of anisotropic slip for fluids based on accommodation tensor. The model is obtained by the analytical approximate calculations developed in the framework of the kinetic theory. We thus generalize Maxwell's equation by showing that the slip length tensor is directly related to the accommodation tensor. The model is in good agreement with the MD results. Thanks to our MD simulations, we develop a suitable technique for reproducing the anisotropy of the accommodation tensor.

The thesis ends with a conclusion section in which we present some perspectives for continuations of this work.

Chapter 1

Theories and computation methods in microfluidics

1.1 Kinetic theory of gases

1.1.1 Velocity distribution function

A fluid is an ensemble of a large number of molecules that interact and move in space. The macroscopic behavior of the fluid can then be completely determined from the knowledge of the particle positions and velocities. However, such a description is not feasible when the number of molecules achieve the order of the continuum limit. A more cost effective way to model fluids, especially suitable for gases, is to use a single statistical distribution function [4].

Consider at time instant t and at location $\mathbf{x}(x_1, x_2, x_3)$ in the physical space, there are N fluid molecules occupying a differential volume $d\mathbf{x} = dx_1 dx_2 dx_3$. In addition to time and location, these molecules can also be classified by their velocity $\mathbf{v}(v_1, v_2, v_3)$. As a result, the probability density function $f(\mathbf{x}, \mathbf{v}, t)$ for the velocity can be defined by

$$dN = f d\mathbf{v}, \tag{1.1}$$

where dN is the number of particle in the sample with velocity in the range of $\mathbf{v}$ and $\mathbf{v} + d\mathbf{v}$. The term $d\mathbf{v} = dv_1 dv_2 dv_3$ denotes a differential volume in the velocity space (see Fig.1.1).

Knowing the distribution function f, the macroscopic properties $\overline{Q}$ (stresses, temperature,

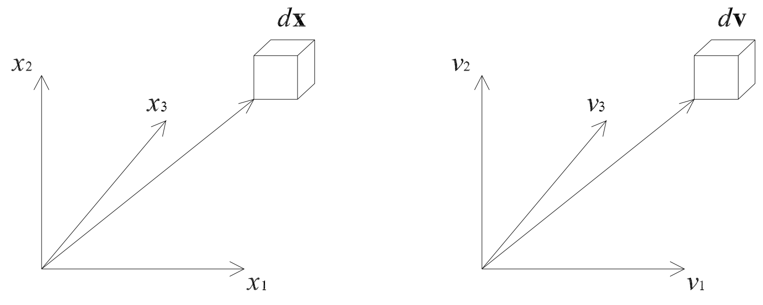

Figure 1.1: Elementary volume in physical and velocity space.

Table 1.1: Some relations between macroscopic physical quantities $\overline{Q}$ and molecular quantities Q. Here, m and $\rho = nm$ are respectively the molecular mass and the mass density

$\overline{Q}$	Q
Stream velocity $\mathbf{u}$	$\mathbf{v}$
Stress tensor $\boldsymbol{\sigma}$	$-\rho(\mathbf{v}-\mathbf{u})\otimes(\mathbf{v}-\mathbf{u})$
Heat flux $\mathbf{q}$	$\frac{\rho}{2}\lvert\mathbf{v}-\mathbf{u}\rvert^2(\mathbf{v}-\mathbf{u})$

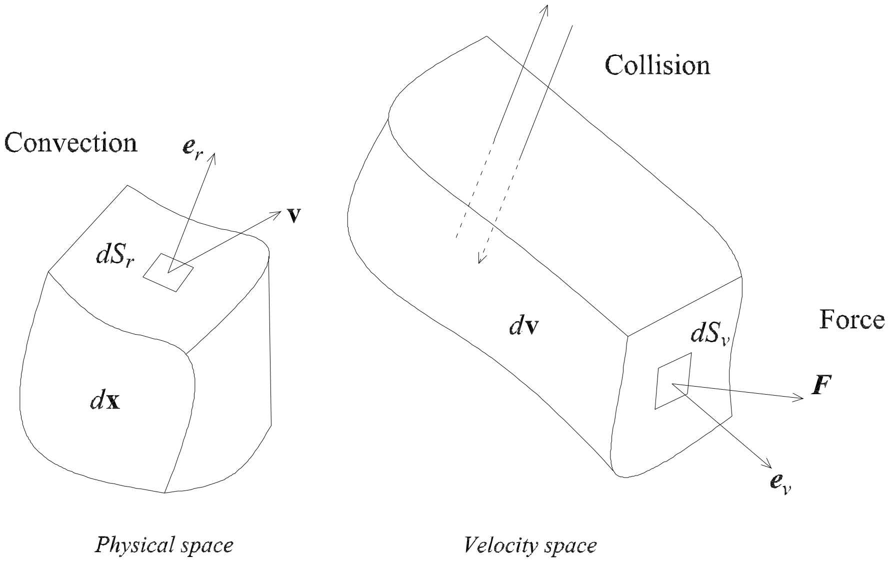

Figure 1.2: Phase space element

mean velocity, etc...) can be determined by means of average of the molecular quantities Q (velocity, momentum, energy, etc...)

$$\overline{Q} = \frac{1}{n}\int Qf d\mathbf{v}, \quad n = \int f d\mathbf{v}, \tag{1.2}$$

where n is the number density. Generally, these macroscopic quantities are moments of the distribution function f, as listed in Table 1.1.

1.1.2 The Boltzmann equation

The evolution of f with time in physical and velocity spaces can be studied on the basis of the conservative equations. For an element in the combined phase space $d\mathbf{v}d\mathbf{x}$ shown in Fig. 1.2, the local rate of change of the number particles at time t is

$$\frac{\partial f}{\partial t} d\mathbf{x} d\mathbf{v}, \tag{1.3}$$

The change in the number of particles within $d\mathbf{x}d\mathbf{v}$ can be caused by inflows of particles through each side of the phase space element. First, the net inflow of particles through the physical space element $d\mathbf{x}$ is due to the convection of particles across the surface S_r of $d\mathbf{x}$.

Considering class $\mathbf{v}$ particles, the convection inflow reads

$$-\int_{S_r}(f\mathbf{v})\cdot(\mathbf{e}_r dS_r)d\mathbf{v}, \tag{1.4}$$

with $\mathbf{e}_r$ being the unit normal vector of surface element dS_r. Using the Gauss theorem, the surface integral can be rewritten as the volume integral :

$$\int_{d\mathbf{x}}\nabla\cdot(f\mathbf{v})d\mathbf{x}d\mathbf{v}\ . \tag{1.5}$$

Since f and $\mathbf{v}$ are constant within $d\mathbf{x}$ and only particles of class $\mathbf{v}$ are considered, the equation becomes

$$-\mathbf{v}\cdot\frac{\partial f}{\partial \mathbf{x}}d\mathbf{x}d\mathbf{v}. \tag{1.6}$$

Secondly, the flux of particle across sides of $d\mathbf{v}$ can be caused by external force per unit mass $\mathbf{F}$. Similar to particle fluxes across side of $d\mathbf{x}$, the net inflow through the velocity space $d\mathbf{v}$ is written as

$$-\mathbf{F}\cdot\frac{\partial f}{\partial \mathbf{v}}d\mathbf{x}d\mathbf{v}. \tag{1.7}$$

In addition to the above processes, the local number of particles can be changed by intermolecular collisions in the velocity space. This effect is expressed via the integral operator

$$\left\{\frac{\partial f}{\partial t}\right\}_{coll}d\mathbf{x}d\mathbf{v}. \tag{1.8}$$

The collision term can be evaluated by considering the collision between two particles of different class, say $\mathbf{v}$ and $\mathbf{v}_1$ and their post collision velocities $\mathbf{v}'$ and $\mathbf{v}_1'$. Skipping the proof which is presented in many previous works [3, 4, 8], we admit the following final expression

$$\left\{\frac{\partial f}{\partial t}\right\}_{coll}d\mathbf{x}d\mathbf{v}=\left(\int_{-\infty}^{\infty}\int_{0}^{4\pi}v_r I(v_r,\Omega)(f'f_1'-ff_1)d\Omega d\mathbf{v}_1\right)d\mathbf{x}d\mathbf{v}, \tag{1.9}$$

where f_1, f' and f_1' is the velocity distribution function at $\mathbf{v}_1$, $\mathbf{v}'$ and $\mathbf{v}_1'$ class and v_r is the relative velocities between the particles before and after collision,

$$v_r=|\mathbf{v}-\mathbf{v}_1|=|\mathbf{v}'-\mathbf{v}_1'|. \tag{1.10}$$

The term $I(v_r,\Omega)$ is the differential cross section of the collision, in which the relative velocity of the colliding particles falls within the solid angle $d\Omega$.

Finally, the equation for the change of particle number of class $\mathbf{v}$ becomes

$$\frac{\partial f}{\partial t}+\mathbf{v}\cdot\frac{\partial f}{\partial \mathbf{x}}+\mathbf{F}\cdot\frac{\partial f}{\partial \mathbf{v}}=\int_{-\infty}^{\infty}\int_{0}^{4\pi}v_r I(v_r,\Omega)(f'f_1'-ff_1)d\Omega d\mathbf{v}_1. \tag{1.11}$$

which is the Boltzmann equation for a simple dilute gas.

1.1.3 Approximate solutions

For the gas in equilibrium, the velocity class must be constant with time and position. As a result, the collision term in the Boltzmann equation must vanish

$$\left\{\frac{\partial f}{\partial t}\right\}_{coll}=0. \tag{1.12}$$

Table 1.2: Approach equations of CE model for different order k of Kn.

Order k	Model equations
Kn^0	Euler
Kn^1	Navier-Stokes-Fourier
Kn^2	Burnett

That condition implies that

$$f'f_1' - ff_1 = 0 \quad \text{or} \quad \ln f' + \ln f_1' = \ln f + \ln f_1 \tag{1.13}$$

or $\ln f$ is a collision invariant. Thus, it is natural to express $\ln f$ as linear combination of linear momentum and kinetic energy since they are both collision invariant. Finally, we can derive the famous Maxwellian distribution f_0

$$f_0(\mathbf{v}) = n\left(\frac{m}{2\pi k_B T}\right)^{3/2} e^{\frac{-m|\mathbf{v}-\mathbf{u}|^2}{2k_B T}} . \tag{1.14}$$

with k_B being the Boltzmann constant. For nonequilibrium gases, the Boltzmann equation is mathematically difficult to solve due to the integral form of the collision term. In the literature, approximate solutions have been proposed based on the simplified treatment of the latter [9–11].

Bhatnagar, Gross and Krook (BGK) [9] replaced the collision operator by a difference between the sought distribution function f and a local equilibrium distribution f_0

$$\left\{\frac{\partial f}{\partial t}\right\}_{coll} = \frac{1}{\tau}(f_0 - f) , \tag{1.15}$$

where τ is the characteristic time of the evolution from the particle distribution to the equilibrium distribution. The basic idea of the BGK model is to see the collision process as a relaxation phenomenon and the main role of the collision term is to relax the distribution function into an equilibrium distribution. It is also assumed that the actual distribution function is not very far from the equilibrium distribution.

Using the Knudsen number, Chapman and Enskog (CE) [10] employed an asymptotic expansion of f

$$f = f_0(1 + \mathrm{Kn}\psi_1 + \mathrm{Kn}^2\psi_2 + ...) , \tag{1.16}$$

where $\psi_1, \psi_2, ...$ are functions of gas density, temperature and macroscopic velocity. By truncating the series at order k of Kn, we obtain the $k-$order constitutive equations from the Boltzmann equation as shown in Table 1.2.

An alternative approach is proposed by Grad [11], the Grad13 and Grad26 equations, taking higher order moments as variables in addition to the usual quantities temperature, density, etc.... Although these theories are very promising, the development is still underwork, dealing with issues such as boundary conditions, solution existence, etc...

At finite Knudsen number, the Boltzmann equation can be also solved numerically with Direct Simulation Monte Carlo (DSMC) method. Representative particles are used in a DSMC simulation instead of real molecules and the collisions between these particles are

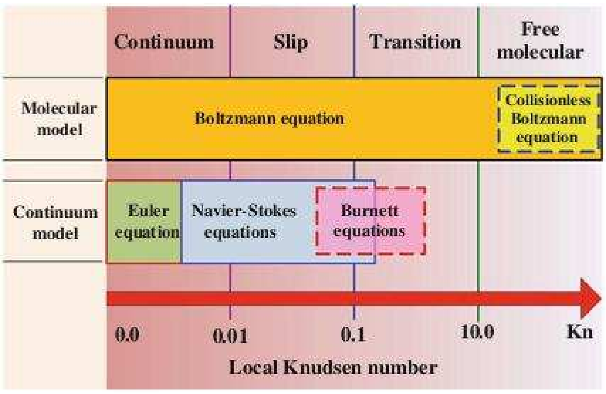

Figure 1.3: Classification of the gas flow regimes and governing equations over the range of Knudsen numbers (Zhang *et al.*, 2012)[13].

treated randomly. To date, the DSMC method is considered as the most accurate and efficient numerical method for rarefied gas flow simulation and has been widely used in practice.

1.1.4 Flow regimes and validity of models

A key nondimensional parameter for microflows is the Knudsen number, which is defined as the ratio

$$\mathrm{Kn} = \frac{\lambda}{H}, \tag{1.17}$$

where H is the characteristic length scale of flow and λ is the mean free path estimated by

$$\lambda = \frac{1}{\sqrt{2}n\pi\sigma^2} \ . \tag{1.18}$$

The quantity σ in Eq. 1.18 is the diameter of the fluid molecules. In the case of Lennard Jones (LJ) fluid, this diameter is approximately taken equal to the reference length σ appearing in the LJ interaction potential.

In rarefied gas dynamics, the Knudsen number is normally used as a measure of the degree of rarefaction. Rarefaction effects become more important as the Knudsen number increases and thus pressure drop, shear stress, heat flux and corresponding mass flow rate cannot be predicted by using models based on the continuum hypothesis [12]. A classification of the different flow regimes and the corresponding governing equations are shown in Fig. 1.3.

- $\mathrm{Kn} < 10^{-3}$: the flow is considered as a continuum and the transport phenomena can be modeled by Navier-Stokes and energy conservation equations.
- $10^{-3} < \mathrm{Kn} < 10^{-1}$: it is considered a slip flow. The Navier-Stoke and energy equations remain applicable but it is necessary to take into account the boundary conditions with slip velocity and temperature jump in the walls.
- $10^{-1} < \mathrm{Kn} < 10$: transition flow.
- $\mathrm{Kn} > 10$: free-molecular flow.

For gas flow with high Knudsen number ($> 10^{-1}$), the number of particle in a volume unit of gas decreases and the number of intermolecular collisions is probably not sufficient to form an equilibrium state. The behavior of individual particle become more important for the macroscopic behavior of gas flow as the Knudsen number increases. The continuum approximation used in the flows with small Knudsen number is then invalid and it is necessary to apply microscopic approaches like the Boltzmann equation, that recognize the molecular property of gases.

1.1.5 Gas-surface interface mechanisms

At the micro/nanoscale, the gas-surface interactions can have significant impacts on the overall flow behavior. In the near surface region, the gas cannot be considered as in equilibrium and the energy and momentum transfer between the gas particle and the surface should be examined. This area is called the Knudsen layer : a thermodynamically nonequilibrium region extending a distance of a few mean free path from the surface. For flows with small Knudsen number, the effect of Knudsen layer is not significant, the continuum approximation can be used by extrapolating the bulk gas flow towards the surface. At high Knudsen number, the collision frequency may be insufficient to reach an equilibrium state and the distribution function of gas will deviate from the Maxwellian distribution in the Knudsen layer.

The gas-surface interaction can be accessed via some averaged parameters such as the momentum and energy accommodation coefficients. While the tangential and normal momentum accommodation coefficients are used to characterize the momentum exchanges parallel and perpendicular to the surface, the thermal accommodation coefficient is used for the energy exchange.

The Tangential Momentum Accommodation Coefficient σ_t (abbreviated as TMAC) is defined as [14]

$$\sigma_t = \frac{v_{it} - v_{rt}}{v_{it} - u_w}, \tag{1.19}$$

where v_{it} and v_{rt} are respectively the tangential velocity of incident and reflected particles and u_w is the wall velocity.

When $\sigma_t = 0$, the reflection is purely specular. As a result, the tangential velocity component is unchanged, but the normal velocity component is reversed (see Fig. 1.4). This corresponds to an extreme case where the wall is *ideally smooth*. In the other extreme, the wall is *ideally rough* and the reflection is purely diffusive, i.e $\sigma_t = 1$. The reflection occurs at a random angle and the average tangential velocity of reflected particles is zero. In Maxwell's work, a mixed reflection mechanism is proposed: a portion of the particles reflect specularly and the remaining reflect diffusively.

Since it is impossible to predict theoretically the trajectories or distribution of the incident and reflected particles, σ_t is usually determined from experiments or numerical simulations As shown in the later sections, the coefficient depends on many factors such as gas-surface interaction potentials, the morphology of surface and temperature.

Unlike the TMAC, the Normal Momentum Accommodation Coefficient (NMAC) σ_n has

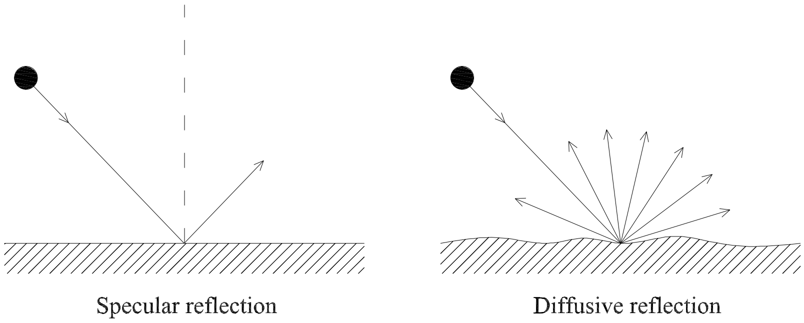

Figure 1.4: Specular reflection and diffusive reflection.

various forms of definitions as follows [14],

$$\sigma_n = \frac{|v_{in}| + |v_{rn}|}{|v_{in}| + |v_{wn}|}, \tag{1.20}$$

$$\sigma_n = \frac{|v_{in}| - |v_{rn}|}{|v_{in}| - |v_{wn}|}, \tag{1.21}$$

$$\sigma_n = \frac{|v_{in}| - |v_{rn}|}{|v_{in}|}, \tag{1.22}$$

$$\sigma_n = \frac{|v_{in}| + |v_{rn}|}{|v_{in}|}, \tag{1.23}$$

in which v_{in} and v_{rn} are the normal velocity of incident and reflected particles, respectively, and v_{wn} is given by :

$$v_{wn} = \sqrt{\frac{\pi k_B T_w}{2m}}, \tag{1.24}$$

where T_w is the wall temperature.

In Equation (1.21), σ_n is singular when $|v_{in}| = |v_{wn}|$, while in the other equations (1.20), (1.22) and (1.23), a singular σ_n can be avoided. However, the expressions of (1.22) and (1.23) only show the relative normal momentum of incident and reflected particles but cannot represent the accommodation with the wall [14].

The energy transfer between the monoatomic gas particles and the surface can be characterized via the Energy Accommodation Coefficient (EAC) σ_T defined by

$$\sigma_T = \frac{v_i^2 - v_r^2}{v_i^2 - v_w^2}, \tag{1.25}$$

At first glance, the coefficients $\sigma_t, \sigma_n, \sigma_T$ appear to be identical for all collisions. However, with all the complexity of the wall structure at the atomic scale, $\sigma_t, \sigma_n, \sigma_T$ should be understood as effective quantities computed from a given fluxes of momentum and energy.

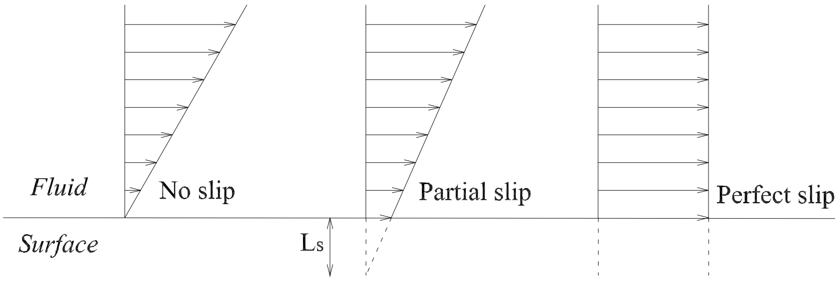

Figure 1.5: Interpretation of the Navier slip length L_s for Couette velocity profiles

1.1.6 Slip boundary conditions

One of the earliest fluid-solid boundary conditions was proposed by Navier [15], postulating that the tangential fluid velocity relative to the wall u_{slip} is proportional to the flow shear rate

$$u_{slip} = u_{fluid} - u_{wall} = L_s \left(\frac{\partial u}{\partial n}\right)_s , \tag{1.26}$$

where L_s is the slip length, u_{wall} the wall velocity and $\frac{\partial}{\partial n}$ the normal derivative at the wall surface. The slip length L_s is shown in Fig.1.5 with three cases : no-slip, partial slip and perfect slip. For a pure shear flow, L_s can be interpreted as the fictitious distance below the real surface where the no-slip boundary condition is satisfied.

According to Maxwell [16], the slip length can be estimated by a simple relation

$$L_s = \lambda \frac{2-\sigma_t}{\sigma_t}. \tag{1.27}$$

The slip equation is usually written in dimensionless form. When combined with thermal transpiration effect [17], it becomes

$$U_{slip} = \frac{2-\sigma_t}{\sigma_t} \mathrm{Kn} \left(\frac{\partial U}{\partial n}\right)_s + \frac{3}{2\pi} \frac{C_p - C_v}{C_p} \frac{Kn^2 Re}{Ec} \frac{\partial T}{\partial s} , \tag{1.28}$$

In (1.28), $\frac{\partial}{\partial s}$ implies tangential derivative at the wall surface, C_p and C_v the heat specific at constant pressure and volume, Re and Ec the Reynolds number and Eckert number.

The slip velocities in second order have also been proposed to extend the validity range of continuum equations for Knudsen numbers corresponding to the start of the transition regime. For the isothermal flows, they could be written in the general form as :

$$U_{slip} = C_1 \mathrm{Kn} \left(\frac{\partial U}{\partial n}\right)_s - C_2 \mathrm{Kn}^2 \left(\frac{\partial^2 U}{\partial n^2}\right)_s , \tag{1.29}$$

where C_1 and C_2 are the first and second order slip coefficients, respectively. For Maxwell's model in Equation 1.28, $C_1 = \frac{2-\sigma_t}{\sigma_t}$ and $C_2 = 0$.

The slip coefficients C_1 and C_2 available from the literature are listed in Tables 1.3 and 1.4 [13, 14]. Table 1.3 presents their values when $\sigma_t = 1$. There is no general agreement

Table 1.3: Values of first and second order slip coefficients in literature

References	Approach	C_1	C_2
Maxwell(1879) [16]	First-order model	1	0
Schamberg (1947) [18]	Second-order model	1	$5\pi/12$
Albertoni *et al.* (1963) [19]	BGK model	1.1455	0
Deissler (1964) [20]	Second-order model	1	9/8
Chapman and Cowling (1970) [10]	Linearized Boltzmann model	1	0.5
Loyalka (1971) [21]	BGK model	0.7252	0
Hsia and Domoto (1981) [22]	Second-order model	1	0.5
Loyalka and Hickey (1989) [23]	BGK based kinetic model	1.1019	0.0449
Mitsuya (1993) [24]	1.5-order model	1	2/9
Pan *et al.* (2000) [25]	First-order model	1.125	0
Karniadakis and Beskok (2002) [26]	Second-order model	1	-0.5
Wu and Bogy (2003) [27]	New second-order model	2/3	0.25
Hadjiconstantinou (2003) [28]	HS model	1.11	0.61
Cercignani and Lorenzani (2010) [29]	HS model	1.1209	0.2347
	BGK-based model	1.1366	0.69261
Li *et al.* (2011) [30]	Lattice Boltzmann model	1	0.8

on the results : C_1 is around unity while C_2 varies from -0.5 to 9/8. In Table 1.4, the expressions of two slip coefficients as function of σ_t are shown. These values could be derived from the Navier-Stokes equation as well as the Boltzmann equation. The first-order slip coefficients C_1 usually relate to σ_t, while the second-order slip coefficients C_2 are rather different.

Using a similar approach made for the slip velocity, von Smoluchowski also proposed a boundary condition for the temperature that can be written in the dimensionless form as,

$$T_{jump} = T_{fluid} - T_{wall} = \frac{2-\sigma_T}{\sigma_T}\left[\frac{2C_p}{C_p+C_v}\right]\frac{Kn}{Pr}\left(\frac{\partial T}{\partial n}\right)_s , \tag{1.30}$$

where σ_T is the thermal accommodation coefficient and Pr is the Prandtl number given by :

$$Pr = \frac{C_p\eta}{\kappa} , \tag{1.31}$$

in which η is the dynamical viscosity and κ is the thermal conductivity.

Table 1.4: Expressions of first and second order slip coefficients in literature

References	C_1	C_2
Maxwell (1879) [16]	$\frac{2-\sigma_t}{\sigma_t}$	0
Loyalka (1971) [21]	$\frac{2-\sigma_t}{\sigma_t}\frac{\sqrt{\pi}}{2}(1-0.1871\sigma_t)$	0
Cercignani (1988) [31]	$\frac{2}{\sqrt{\pi}}\frac{2-\sigma_t}{\sigma_t}(1+0.1621\sigma_t)$	$\frac{2}{\pi}(0.5+C_1^2)$
Jie *et al.* (2000) [32]	$\frac{2-\sigma_t}{\sigma_t}$	$-\frac{2-\sigma_t}{\sigma_t}\frac{Re}{Kn}$
Aubert and Colin (2001) [33]	$\frac{2-\sigma_t}{\sigma_t}$	9/8
Karniadakis and Beskok (2002) [26]	$\frac{2-\sigma_t}{\sigma_t}$	$-\frac{2-\sigma_t}{2\sigma_t}$
Lockerby *et al.* (2004) [34]	$\frac{2-\sigma_t}{\sigma_t}$	$\frac{9}{4\pi}\frac{Pr(\gamma'-1)}{\gamma'}$
Wu (2008) [35], $f = min[1/Kn, 1]$	$\frac{2}{3}\left[\frac{3-\sigma_t f^3}{\sigma_t} - \frac{3}{2}\frac{(1-f^2)}{Kn}\right]$	$\frac{1}{4}\left[f^4 + \frac{2}{Kn^2}(1-f^2)\right]$

1.2 Molecular Dynamics method

Molecular Dynamics was first introduced by Alder and Wainwright in the late 1950's to study the interactions of hard spheres [7]. This method consists in studying the trajectory of particles, simulating the spatial evolution of system over the time. In the simulation, each particle is considered as a point mass whose movement is determined by all the forces exerted on it by other particles. The laws of Newtonian classical mechanics applied to a particle i can be written as :

$$\mathbf{v}_i(t) = \frac{\partial \mathbf{r}_i}{\partial t} \ , \tag{1.32}$$

$$m_i \frac{\partial \mathbf{v}_i}{\partial t} = \mathbf{F}_i = -\frac{\partial V_{pot}}{\partial \mathbf{r}_i} \ , \tag{1.33}$$

in which $\mathbf{v}_i$, $\mathbf{r}_i$ and m_i are the velocity, position and mass of particle i, respectively. $\mathbf{F}_i$ is the force acting on the particle i and V_{pot} is the total potential energy of the system consisting of N particles.

The equations of motion could be integrated by breaking the computations into a series of very short time steps (normally about some femtoseconds). At each step t_i, the forces on the atom i are calculated and combined with the current position and velocity to determine its new position and velocity at time t_{i+1}. An updated set of forces is then computed for the new position, and so on the trajectory of particle versus time is totally known.

1.2.1 Interatomic potential

The interatomic potentials play an important part in the MD simulations since they govern the dynamics of the system and thus the accuracy of the results. The best known of pairwise potentials is the Lennard-Jones (LJ) 12-6. It represent the van der Waals forces with one repulsive term in r^{-12} and one attractive term in r^{-6}. For a pair of atoms i and j the potential energy is :

$$V(r_{ij}) = 4\epsilon \left[\left(\frac{\sigma}{r_{ij}} \right)^{12} - \left(\frac{\sigma}{r_{ij}} \right)^{6} \right], \quad r_{ij} = \mid \mathbf{r}_i - \mathbf{r}_j \mid \tag{1.34}$$

where the parameters ϵ and σ are the scales of energy and length, respectively. The interaction repels at close range, then attracts, and is eventually cut off at some limiting separation r_c.

Traditionally the Lennard-Jones potentials are the most used since the mathematical expression allows to derive forces between particles efficiently. However, although the attractive part depending on r^{-6} describes correctly the dispersion interaction between two particles, the repulsive part in r^{-12} has no theoretical justification. To overcome this drawback, the repulsive part can be replaced by $V_0 e^{-\alpha(r_{ij}-R_0)}$ which reproduces correctly the Pauli repulsion. The total pairwise potential should then be described by the Buckingham form [36]:

$$V(r_{ij}) = V_0 e^{-\alpha(r_{ij}-R_0)} - \frac{C_6}{r_{ij}^6}, \tag{1.35}$$

where R_0 is the position of the minimum of $V(r_{ij})$. Increases in R_0 decrease the corrugation of the gas-surface potential. V_0 and α must allow to reproduce the Pauli repulsion at short ranges, and C_6 is the van der Waals dispersion parameter.

Besides, for a metallic cluster or a nanoparticle, the Sutton-Chen potential is often employed to calculate the interaction between solid atoms. It has the form :

$$V_{pot} = \epsilon \left[\frac{1}{2} \sum_{i=1}^{N} \sum_{\substack{j=1 \\ j \neq i}}^{N} \left(\frac{a}{r_{ij}} \right)^{n} - c \sum_{i=1}^{N} \rho_i^{1/2} \right], \quad \rho_i = \sum_{\substack{j=1 \\ j \neq i}}^{N} \left(\frac{a}{r_{ij}} \right)^{m}, \tag{1.36}$$

where c is a dimensionless parameter and ρ_i is the local density of atom i. The parameters ϵ and a determine the scales of energy and length, respectively and, n and m the range and shape of the potential.

To save computational time, the interaction potential is often truncated at a cut-off distance of $r_c \approx 2.5\sigma$ to 5σ. This cut-off radius corresponds to the distance beyond which the interactions between the particles are negligible and not taken into account for the calculation of the forces. For example, at a typical cutoff distance of $r_c = 2.5\sigma$ the interaction energy of LJ potential is just about 0.0163 of the well depth. However, the use of truncated potential can pose a problem at small cut-off radius. It may cause a discontinuity in both the potential energy and the force near the cutoff value that effect to the energy conservation of system.

1.2.2 Boundary conditions

In order to conserve the macroscopic behavior of simulated system and save the computational time, the boundary condition should be treated in a reasonable manner. In

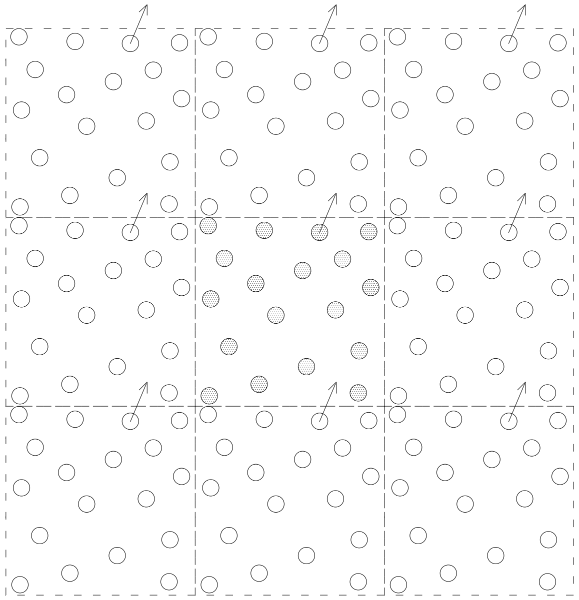

Figure 1.6: Periodic boundary conditions for a simulation box in two dimensions

molecular dynamic simulations, the most used method is periodic boundary conditions where the simulation region is divided into boxes and the central box is replicated in all directions to give a periodic array. An example of two dimensional box is plotted in Fig. (1.6). As seen in the figure, the central box is bounded by 8 neighbors; in three dimensions, the number of neighboring boxes would increase to 26. During the simulation, if a particle leaves the box, another particle having the same physical properties go through the opposite side. Hence, there are in fact no physical walls in boundaries of simulated box and the number of particles thus remains constant.

Another problem concerning the boundary condition is the interaction field between the particles. It is important to ensure that the particle cannot interact with its own image and, hence, influences its own behavior. This condition is known as the minimum image convention where the smallest box dimension must be greater than two times of the interaction range. In the minimum image convention, each particle detect at most just one image of every other particle of system which is repeated infinitely by the periodic boundary conditions [37]. As the minimum image convention is respected, the periodic boundary conditions allow to maintain the energy and momentum of the system.

1.2.3 Initial state

Before a simulation can be performed, it is necessary to set initial positions and velocities to all particles in the system. As the aim of the simulation is to study the equilibrium fluid state, the choice of the initial state should not have effects on the results of the simulation. Usually, the initial configuration of system can be started with simple lattices for the the gas atoms, such as the square or cubic lattice. On the other hand, the solid atoms are placed at the sites of a crystalline lattice, for example cubic, body-centered cubic, face-centered cubic, as shown in the Fig. 1.7. The lattice size should be chosen appropriately according to the type of system under study. The initial velocities are drawn from Maxwell-Boltzmann distribution corresponding to the average temperature of the system considered.

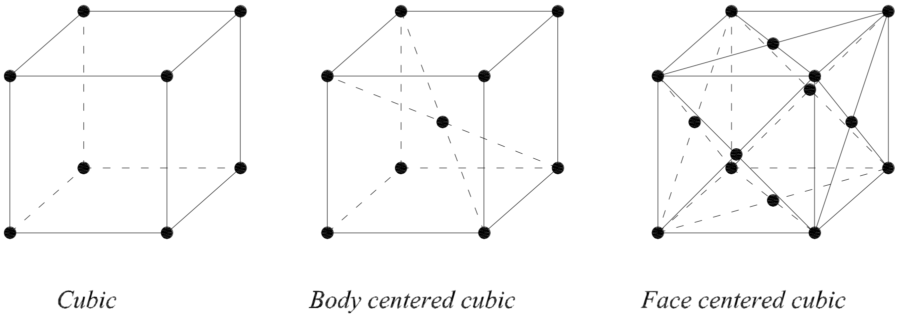

Figure 1.7: Typical initial configurations for the solid atoms

1.2.4 Integration of motion equations

The time integration of the Newton equations of motion allows the determination of the evolution of a system as function of time. We have the positions, velocities, and accelerations at time t and we want to calculate these values at time $t + \delta t$, where δt is the time step. A popular integration scheme which was widely used is the Verlet method and the Leapfrog algorithm [38]. The position of particle i at time $t+\delta t$ is derived from the Taylor expansion of the position at time t :

$$\mathbf{r}_i(t + \delta t) = \mathbf{r}_i(t) + \delta t \mathbf{v}_i(t) + \frac{\delta t^2}{2}\mathbf{a}_i(t) \ , \tag{1.37}$$

where $\mathbf{v}_i(t)$ and $\mathbf{a}_i(t)$ are the velocity and acceleration of particle i at time t, respectively. The next step is to evaluate the velocity at half time (i.e. $t + \delta t/2$) and to calculate the acceleration at time $t + \delta t$ from the interaction forces :

$$\mathbf{v}_i(t + \frac{\delta t}{2}) = \mathbf{v}_i(t) + \frac{\delta t}{2}\mathbf{a}_i(t) \ , \tag{1.38}$$

$$\mathbf{a}_i(t + \delta t) = -\frac{\mathbf{F}_i(t + \delta t)}{m_i} \ . \tag{1.39}$$

Finally, the velocity at time $t + \delta t$ is given by

$$\mathbf{v}_i(t + \delta t) = \mathbf{v}_i(t + \frac{\delta t}{2}) + \frac{\delta t}{2}\mathbf{a}_i(t + \delta t) \ . \tag{1.40}$$

The process is continued with successive time step δt and the evolution of a system is therefore completely calculated. In molecular dynamic simulations, typical values of δt are close to $1\, fs$.

1.2.5 Thermostats

During the simulation, at equilibrium or non-equilibrium state, it is helpful to work at a constant temperature, at which a thermostat should be used. The thermostat can be applied either on wall particles, fluid particles or all particles of the system. The thermostat methods are separated into global and local natures. The global thermostats, such as velocity scaling or the ones of Nosé-Hoover [39] and Berendsen [40], control the system temperature and dissipate the energy uniformly within the system. The local thermostats, including Andersen [41], Langevin and Dissipative particle dynamics (DPD) thermostats, dissipate energy on the spatially localized scale from a stochastic point of view [42].

In the present work, the Langevin thermostat is used for the solid walls. The motion of a particle i is governed by the equation

$$m_i \frac{d\mathbf{v}_i(t)}{dt} = -\xi \mathbf{v}_i(t) + \mathbf{f}_i(t) + \mathbf{R}_i(t) \ . \tag{1.41}$$

where ξ is a damping coefficient, $\mathbf{v}_i$ is the velocity and m_i is the mass of particle i. $\mathbf{f}_i$ and $\mathbf{R}_i$ are the interaction force and the random force applied on the particle i, respectively.

1.2.6 Calculation of physical properties

1.2.6.1 Statistical ensembles

In statistical physics, one of the basic concept is the ergodic hypothesis, in which the average values over time of the physical quantities are equal to the statistical average values of the quantities. This hypothesis is expressed by

$$\overline{Q} \equiv \frac{1}{\tau} \int_0^\tau Q(t)dt = \sum_i p_i Q_i \equiv \langle Q \rangle \ , \tag{1.42}$$

where $\overline{Q}$ and $\langle Q \rangle$ are the time average value and the ensemble average value of the quantity Q, respectively. p_i is the probability of finding the system in microscopic state i and Q_i is the value of Q at microscopic state i. Physical systems for which the ergodic hypothesis is valid are called ergodic systems.

Macroscopic systems containing many particles are complex systems. In principle, to completely characterize a system with N particles, we have to know three components of position and three component of velocity for each particle. It is practically impossible to obtain these $6N$ real numbers. However, not knowing all the information about all particles does not prevent to calculate the macroscopic properties of the system. In fact, quantities like energy, temperature, pressure ... are computed as statistical averaged quantities of a large enough number of particles.

Different macroscopic environmental constraints lead to different types of ensembles, with particular statistical characteristics [43]. As the Newton equations lead naturally to energy conservation, molecular dynamics simulation is traditionally performed under the microcanonical or NVE ensemble where the number of particles N, volume V and energy E of the systems are kept constant. However, other ensembles are sometimes used in molecular dynamics as NVT ensemble, NpT ensemble and μVT ensemble. The ensemble widely used for Monte Carlo simulation is canonical or NVT ensemble in which the number of particles, volume, and temperature are fixed. Generally, in large NVE systems, the fluctuations of temperature are small, and temperature may be considered approximately constant. Therefore, a rather small part of a system may be considered as a canonical system.

Closely related to the NVT ensemble is the isothermal-isobaric, or NPT ensemble, with the pressure P, rather than the volume V, kept fixed. While the microcanonical, canonical and isothermal-isobaric ensembles describe closed systems for which there is no change in the number of particles, the grand canonical or μVT ensemble is for an open system in which the number of particles can change and the chemical potential (μ), volume and temperature remain constant.

1.2.6.2 Physical quantities

Different from the kinetic theory, Molecular Dynamics methods describe explicitly all atoms in the system and the physical properties of the system can be computed accurately from their positions and velocities.

Energy
The internal energy is the sum of potential and kinetic energies

$$E = E_p + E_c \ . \tag{1.43}$$

For a system with N particles, the potential energy E_p and kinetic energy E_c are given by

$$E_p = \sum_{i=1}^{N} E_i^e + V_{pot} \ , \tag{1.44}$$

$$E_c = \frac{1}{2}\sum_{i=1}^{N} m_i(\mathbf{v}_i - \mathbf{v})^2 \ , \tag{1.45}$$

where E_i^e is the external interaction potential applied to particle i and V_{pot} is the internal total potential of the system as mentioned at the beginning of the present Chapter. In (1.45), $\mathbf{v}_i$ is velocity of particle i and $\mathbf{v}$ is barycentric velocity of flow.

Temperature
Unlike the canonical ensemble, in microcanonical ensemble, the temperature is not constant. It can be deduced from the kinetic energy of a system thanks to the theorem of the equipartition of energy as follows :

$$E_c = \frac{k_B T}{2}(3N - N_c) \ , \tag{1.46}$$

where N_c is the number of constraints on the system and k_B is the Boltzmann constant.

Pressure
For homogeneous fluids, the external pressure is expressed via the virial theorem as the sum of two terms, one that corresponds to the part of ideal gas and the other involves the interactions between the particles (virial) :

$$P = \frac{1}{V}\left[N k_B T - \frac{1}{3}\sum_{i=1}^{N}\sum_{j=i+1}^{N} \mathbf{r}_{ij}\mathbf{f}_{ij} \right] \ , \tag{1.47}$$

where $\mathbf{r}_{ij}$ is the vector joining particles i and j, and $\mathbf{f}_{ij}$ is the interaction forces between i and j.

For inhomogeneous fluids, the pressure may be calculated from the formulae of Irving and Kirkwood [44], Todd *et al.* [45] and the associated method of plane (MOP) by Evans *et al.* [46]. These issues will be dealt with in Chapter 2.

1.2.7 Optimization method for interaction computations

There are different methods to compute the interactions between particles, like : all-pairs, cell subdivision and neighbor list (or Verlet list). All-pairs method is easy to perform but is not efficient, at least when the interaction field r_c is small compared with the size of simulation region. Although the use of cutoff radius allows to reduce the number of calculated forces, the test number of interatomic distances remains unchanged in comparison with the case without cutoff radius (see Fig. 1.8). In the present work, we have combined cell subdivision and neighbor list methods in order to optimize the computational effort.

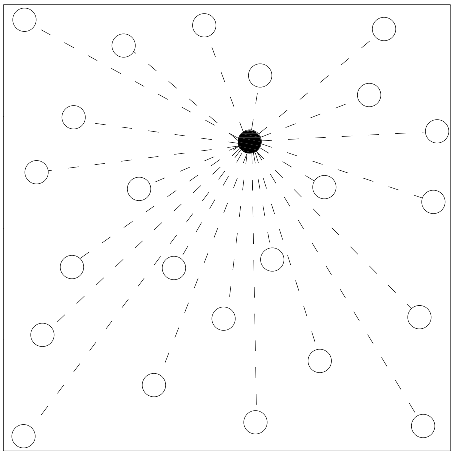

Figure 1.8: All-pairs method for interaction computations : in a simulation box, all pairs of particles should be examined.

1.2.7.1 Cell subdivision

This method consists in dividing the simulation region into many identical cubic cells whose side size is greater than the cutoff radius. Thus a given particle interacts only with the particles located either in the same cell or in the adjacent cells. An example of cell subdivision method is shown in Fig. 1.9 in the 2D case. The computational zone of interactions is bounded by the central cell and 8 neighboring cells. In three dimensions, the number of adjacent cells of a given cell is increased up to 26. However, because of symmetry, only half of cells needs be examined for the interatomic forces computations (i.e. 13 in 3D and 4 in 2D).

1.2.7.2 Neighbor list

During the simulation, the microscopic environment change slowly : the particles almost remain in the same region of space for some integration steps. Therefore, in parallel with the cell subdivision method, we have used the neighbor list method to create the lists of neighboring particles with new radius r_v. This radius is chosen such that a particle located outside the sphere bounded by r_v radius does not have the time, during the rebuild time of neighboring list, to enter into the interaction zone of the studied particle. The radius of the neighbor list is written as :

$$r_v = r_c + \Delta r \; . \tag{1.48}$$

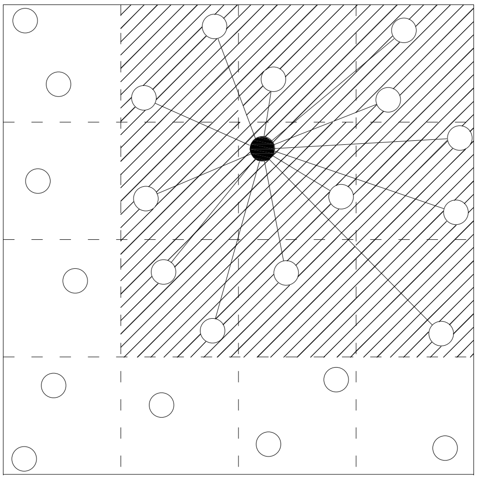

Figure 1.9: Representation of a simulation box in cell subdivision method in two dimensions.

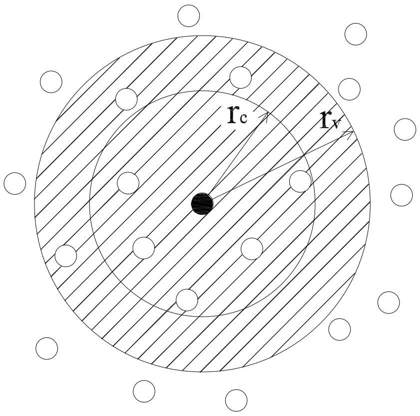

Figure 1.10: Truncated sphere interactions related to r_c and neighbor list related to r_v, of a given particle.

The value Δr is inversely related to the speed at which the list must be rebuilt, and it also determines the number of noninteracting pairs that are included in the list. It therefore has a certain influence on both processing time and storage. Typically, for the fastest computation at liquid densities, $\Delta r \approx 0.3\sigma$ to 0.4σ [47].

1.3 Parallelization of the calculations

A molecular dynamic code can be written using two programming models: sequential or parallel. In the sequential model, a program is carried out by a single process. This process running on a processor of a machine and has access to processor memory. However, for complexes problems with important number of particles, the memory of a single processor may be not large enough and/or the computation time is too high. To overcome these

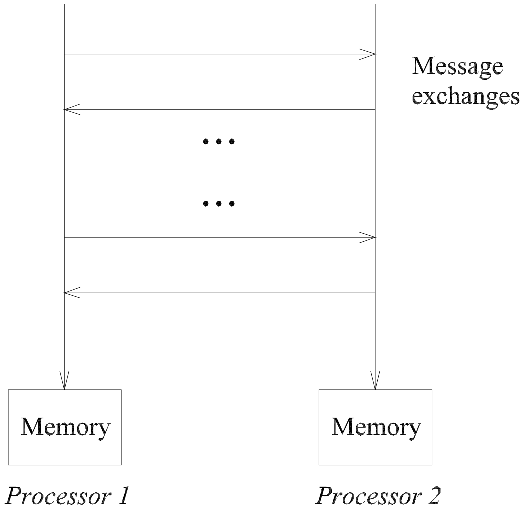

Figure 1.11: Diagram of an MPI application.

problems, we used the parallel calculation of MPI type (Message Passing Interface). This allows to distribute computation charges on multiple processors.

In a parallel programming model by exchanging messages (MPI), each processor executes a copy of the calculation program and has access to its own memory. Therefore, the program variables become local variables at each processor. In addition, a processor cannot access the memory of neighboring processors. However, it may send/receive information to/from other processors by passing messages between processors via library functions MPI. The communication cost consists in two parts: the time to get started a message transfer, and a transfer time that depends on the message length. In order to make the message transfer working efficiently, it is important that the communication cost should be low compared with the computation time of a processor. There is also the problem of charge balancing; obviously the computation is optimal if all processors can be kept busy doing useful computing. If some processors have less work to do than the others, the overall effectiveness is reduced [47].

The MD code used in this thesis is the parallel version described in Ref. [47]. The original code has been developed to match the aim of the present works. For the problems studied, the flow field is divided into several subregions which each processor handles. The number of subregions depends on the number of processors that will be used. In our simulations, the number of processors was only varied from 4 to 16 but it can easily be extended to higher numbers processors according to the machine architecture. Amongst the processors, there is a processor numbered ”0” having the responsibility of collecting the values from all the other processors, after each of theme has calculated its local values. Processor ”0” calculates then the total sums and send these values to each of the other processors.

The communication between two neighboring processors is shown in Fig.1.13. The subroutines *Detection* detects if a particle leaves the field of processor 1, it registers the particle number in *Table A* and then records the corresponding data as : position, velocities, accelerations of particle in *Table B* by subroutine *PackData*. Since a particular particle is no longer associated with a fixed memory location, so unlike the sequential version of the

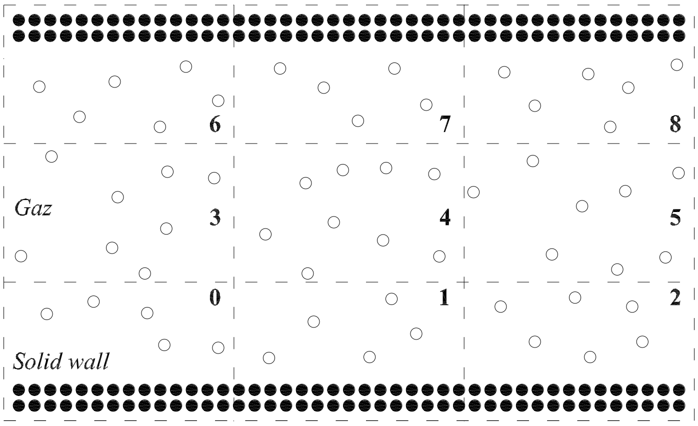

Figure 1.12: Spatial decomposition scheme in two dimensions : each cell is handled by a different processor.

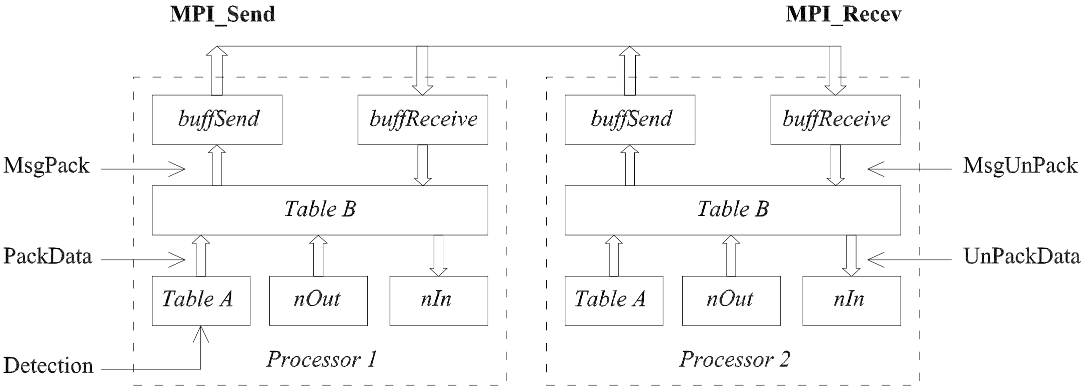

Figure 1.13: Communication between two neighboring processors.

program, each particle is numerated with a unique identifier. The subroutine $MsgPack$ sends the information stored in *Table B* to a buffer called $buffsend$. This buffer is often referred to as *envelope* because the data is being packed into a single message before transmission. After being sent and received between two processors via the MPI sending and receiving functions, the information is stored in the $buffreceive$. Then unpack the data, we finally have the information particle which just enters into the neighboring processor 2.

Chapter 2

Molecular dynamics simulation of Poiseuille flows

2.1 Introduction

One of the fundamental and practical problems in fluid mechanics is the Poiseuille flows between two parallel plates. In the case of Newtonian fluids, the problem has a simple analytical solution which has been used extensively as benchmarks for numerical methods, constitutive models and studies of boundary conditions (see [12] and the references cited therein). Generally, flows and related simulation methods can be classified as acceleration driven or pressure driven. Conventional MD simulations with periodic boundary conditions [48–51] and gravity-like force field are typical examples of the former class. Regarding the latter case, different techniques have been developed to mimic flows induced by pressure difference [52–54]. Lupkowski and Swol [52] placed two rigid walls at the inlet and outlet and applied a piston external forces on them. Li et al. [53] used a fictitious membrane which allows atoms to pass from one direction and forces atoms from the other direction to be elastically reflected with a given probability. Sun and Ebner [54] simulated 2D fluid flows in a long box while controlling the temperature at the two ends.

The present chapter presents a simple alternative procedure to simulate pressure driven flows with Molecular Dynamics method. Section 2.2 gives the problem statement, presents some approximate analytical solutions reported in the archival literature for Poiseuille flows. The pressure expression and the pressure difference from the atomistic point of view are also discussed in Section 2.3. Section 2.4 is focused on the implementation of periodic boundary conditions linked to the pressure difference concept, and its implementation in a MD code. The results of simulations are then compared with approximate analytical solutions of the Navier-Stokes and energy equations in Section 2.5. The application of the present method to fluids other than ideal gases and to rib-roughened channels are also discussed.

2.2 Poiseuille flows and analytical solutions

In the Cartesian coordinate system $Oxyz$, we assume that the flow direction is along the x-axis. The length, width and height of the channel are denoted by L, B and H in direction x, y and z, respectively. The channel width B being very large with respect to the other dimensions, it will be treated as infinite. The fluid can exchange energy with the channel walls which are maintained at constant temperature T_w.

The range of Kn chosen in the present study, $0.02 \leq \mathrm{Kn} \leq 0.1$, belongs to the slip flow regime according to [12], i.e the fluid continuum mechanics is still useful provided that slip boundary conditions are applied at the walls. The validity of the Navier-Stokes equations, as shown by many authors (see [49] for example), can therefore be extended to Poiseuille and Couette flows for the present range of Kn.

In what follows, the terms "pressure driven flow" and "acceleration driven flow" are employed to define two particular cases: i) the body force $\rho\gamma$ applied on a unit fluid volume is zero and the pressure p decreases along the flow direction, $\rho\gamma = 0$, $dp/dx \neq 0$ ii) the inverse situation where $\rho\gamma \neq 0$, $dp/dx = 0$. We shall also consider some available analytical solutions of the Navier-Stokes equations reported in the literature. For both flows, the fluid velocity v in a cross section which accounts for slip effects (Navier boundary conditions) at the wall admits the parabolic form

$$v(\hat{z}) = v(0)\left[1 - a_2 \hat{z}^2\right], \quad \hat{z} = \frac{z}{H}\,. \tag{2.1}$$

where a_2 is a positive dimensionless constant related to pressure gradient (or body force), viscosity, slip length, etc... It is noted that Eq. 2.1 is generally obtained for incompressible fluids but it is also valid for compressible fluid flows in a long channel [55]. In the latter case, all the quantities v, a_2 are functions of the streamwise coordinate x.

An approximation solution of the energy equation can be obtained by neglecting the convective term [56]. The temperature T becomes then a quartic function of the coordinate z

$$T(z) = T_w\left[b_0 - b_4 \hat{z}^4\right]. \tag{2.2}$$

Equation 2.2 is based on the incompressibility assumption. For compressible fluid flows in a long channel, Cai *et al.* [57] used a perturbation technique to derive the following temperature distribution

$$T(x,z) = T_w\left[c_0 - c_2 \hat{z}^2 - c_4 \hat{z}^4\right]. \tag{2.3}$$

The dimensionless coefficients c_i, b_i in Eq. 2.2 and Eq. 2.3 are related to pressure gradient (or body force), viscosity, conductivity, specific heat etc... In Eq. 2.3, the coefficients c_i depend on the position x. We also note that for acceleration driven flow, Todd and Evans [48] suggested a correction to the temperature profile given by Eq. 2.2 as a sextic function of z:

$$T(z) = T_w\left[d_0 - d_2 \hat{z}^2 - d_4 \hat{z}^4 - d_6 \hat{z}^6\right]. \tag{2.4}$$

In section 2.5, MD simulations are used to reexamine the validity of the velocity and temperature profiles given by Eq. 2.1-2.4 and to determine the coefficients a_i, b_i, c_i, d_i by curve fitting.

2.3 Pressure tensor and pressure difference

Before proceeding the molecular dynamics simulation, let us look at the definition of pressure tensor from the atomistic viewpoint. Using statistical mechanic theory, Irving and Kirkwood [44] derived the following pressure tensor decomposition (IK):

$$\mathbf{P} = \mathbf{P}_K + \mathbf{P}_V. \tag{2.5}$$

The kinetic term $\mathbf{P}_K$ depends on the molecular square velocity while the potential term $\mathbf{P}_V$ depends on pairwise interactions between molecules. In a system of N molecules, $\mathbf{P}_K$ and $\mathbf{P}_V$ read

$$\begin{aligned}\mathbf{P}_K(\mathbf{r}) &= \sum_{i=1}^{N} \langle m(\mathbf{v}_i - \bar{\mathbf{v}}) \otimes (\mathbf{v}_i - \bar{\mathbf{v}})\delta(\mathbf{r}_i - \mathbf{r})\rangle \\ \mathbf{P}_V(\mathbf{r}) &= -\frac{1}{2}\sum_{i}^{N}\sum_{j\neq i}^{N} \left\langle \mathbf{r}^{(ij)} \otimes \mathbf{f}^{(ij)} O_{ij}\delta(\mathbf{r}_i - \mathbf{r})\right\rangle \end{aligned} \tag{2.6}$$

The term inside the angular bracket $\langle . \rangle$ denotes the ensemble average and $\otimes$ denotes the dyadic product. The term $\mathbf{r}_i, \mathbf{v}_i, \bar{\mathbf{v}}$ are respectively the position vector, the velocity of the particle i and the mean velocity. The distance vector and interaction force vector between two molecules (i) and (j) are denoted respectively as $\mathbf{r}^{(ij)}$ and $\mathbf{f}^{(ij)}$. For LJ fluids, the two vectors $\mathbf{r}^{(ij)}$ and $\mathbf{f}^{(ij)}$ are colinear and the force magnitude $f^{(ij)}$ is derived from the interaction potential in function of the distance between the two molecules

$$f^{(ij)} = \frac{\partial \mathcal{V}(r^{(ij)})}{\partial r^{(ij)}} \ , \quad r^{(ij)} = \parallel \mathbf{r}_i - \mathbf{r}_j \parallel . \tag{2.7}$$

In Eq. 2.6, the notation $\delta(\mathbf{r}_i - \mathbf{r})$ is used for the delta Dirac function at $\mathbf{r}_i$ and the expression of the operator O_{ij} reads

$$O_{ij} = 1 - \frac{1}{2!}\mathbf{r}^{(ij)}\frac{\partial}{\partial \mathbf{r}} + ... + \frac{1}{n!}\left[-\mathbf{r}^{(ij)}\frac{\partial}{\partial \mathbf{r}}\right]^{n-1} + ... \tag{2.8}$$

Equations 2.8 and 2.6 show that the derivation of IK pressure tensor involves an infinite sum of high order derivatives of the delta function and ensemble average, not suitable for MD computations. A more convenient form of the pressure tensor and an associated calculation method, the method of plane (MOP), was proposed in Todd *et al.* [45] and Evans and Morriss [46]. When the fluid density is uniform, the operator O_{ij} is reduced to unity and equation 2.6 becomes (see [45, 58, 59]):

$$\mathbf{P}_K(\mathbf{r}) = \frac{1}{V}\sum_{i} m(\mathbf{v}_i - \bar{\mathbf{v}}) \otimes (\mathbf{v}_i - \bar{\mathbf{v}}), \quad \mathbf{P}_V(\mathbf{r}) = -\frac{1}{V}\sum_{i<j} \mathbf{r}^{(ij)} \otimes \mathbf{f}^{(ij)} \tag{2.9}$$

where V is the volume of the fluid element located at $\mathbf{r}$. In the literature, Eq. 2.9 is sometimes referred to as IK1 pressure [45, 46]. In Eq. 2.6 and 2.9, the pressure can be decomposed into two scalar quantities p_K and p_V as follows

$$p = p_K + p_V, \quad p_K = \frac{1}{3}\mathrm{tr}\ \mathbf{P}_K, \quad p_V = \frac{1}{3}\mathrm{tr}\ \mathbf{P}_V. \tag{2.10}$$

It is clear that for ideal gases, the potential part p_V vanishes and the pressure is reduced to the kinetic part p_K. For the other fluids, the potential part p_V cannot be neglected. The pressure difference Δp between two points at distance Δl reads

$$\Delta p = \Delta p_K + \Delta p_V = k_B \Delta(nT) + \Delta p_V \ . \tag{2.11}$$

The pressure components P_{xx}, P_{yy}, P_{zz}, number density n and stream velocity $\bar{\mathbf{v}}$ are invariant in direction y. From a microscopic point of view, taking $\Delta l = \Delta y$, we must have

$$\Delta\langle v_x^2\rangle = \Delta\langle v_y^2\rangle = \Delta\langle v_z^2\rangle = 0, \quad \Delta\langle v_x\rangle = \Delta\langle v_y\rangle = \Delta\langle v_z\rangle = 0 \ . \tag{2.12}$$

As it will be discussed in the following, all these conditions are satisfied in our MD simulation algorithm if we apply periodicity for the boundary conditions in the y direction. However, n, p, T can all vary in the flow direction x. We note that in the steady state regime, all quantities like T, p, p_V, n are stable with time, and thus their differences ΔT, Δp, Δp_V, Δn are also stable. In particular, equation (2.11) shows that the finite variation of temperature ΔT along x is related to those of other quantities via the expression

$$\Delta T = \frac{\Delta p - \Delta p_V - k_B T \Delta n}{k_B n + k_B \Delta n} \ . \tag{2.13}$$

If the stream velocity is much smaller than the thermal velocity, we can obtain a simplified expression for the temperature difference as

$$\Delta T = \frac{m}{3k_B} \Delta \langle \mathbf{v}^2 - \overline{\mathbf{v}}^2 \rangle \simeq \frac{m}{3k_B} \Delta \langle \mathbf{v}^2 \rangle \ . \tag{2.14}$$

The objective of the MD method discussed in what follows is to maintain the differences in squared velocity and, thus in temperature, in direction x. By that way, we can indirectly generate the pressure difference Δp. In the case where density ρ is invariant in x-direction (incompressible flow assumption), the temperature difference is proportional, for an ideal gas, to the pressure difference since

$$\Delta p = \frac{\rho}{3} \Delta \langle v^2 \rangle \ . \tag{2.15}$$

2.4 Modified boundary conditions

In Molecular Dynamics, periodic boundary conditions (PBC) applied to velocities are techniques to reduce the study of a large system to a smaller one far from the edge. Considering a simulation domain as a cube, PBC requires that if a molecule passes through one face, it reappears on the opposite face with the same velocity. Obviously, there is no difference in pressure, density or temperature between any two opposite faces of the simulation domain. Consequently $\Delta p = 0$, as it will be shown in the next section.

In our problem, all the pressure components P_{xx}, P_{yy}, P_{zz}, do not vary along y, which can be satisfied by the traditional PBC applied on the faces $y = \pm B/2$. However to create a pressure difference along the x-axis, we must develop a strategy that produces a constant difference between the squared velocity of the molecules crossing the face $x = 0$ and those crossing the face $x = L$.

Usually, to keep unchanged the total number of molecules in the domain whenever a molecule goes out of the domain, we must insert another molecule inside. In this chapter, we generalize the PBC to account for the pressure difference by maintaining the difference in squared velocity at the two opposite faces $x = 0$ and $x = L$.

From equations 2.13 and 2.14, we know that a constant pressure difference is related to a constant difference in squared velocity. A constant parameter δ is thus used to create a constant difference in squared velocity between the inlet and outlet faces (see Fig. 2.1). In order to apply a velocity square difference equal to a constant $3\delta L$ between the faces $x = 0$ and $x = L$, we modify the periodic boundary conditions so that if a molecule goes trough the face $x = L$ with a velocity $\mathbf{v}$, we insert a molecule at $x = 0$ with a velocity $\mathbf{v}'$ satisfying the following conditions

$$\mathbf{v}' = \alpha \mathbf{v}, \quad \alpha = \sqrt{1 + 3\delta L / v^2}. \tag{2.16}$$

Analogously, if a molecule crosses the face $x = 0$ with a velocity $\mathbf{v}$, it reappears at $x = L$ with a velocity $\mathbf{v}'$ so that

$$\mathbf{v}' = \alpha \mathbf{v}, \quad \alpha = \sqrt{1 - 3\delta L / v^2}. \tag{2.17}$$

Since $3\delta L$ is positive, it may happen that $v^2 - 3\delta L < 0$. It is then impossible to find v' satisfying Eq. 2.17. However, this effect can be assumed negligible for flows with relatively small speed (of the order 1% of the thermal speed), as seen in most MEMS/NEMS devices. In the present simulations, the number of molecules that do not satisfy Eq. 2.17 were found less than 1% of the outgoing molecules. In order to simulate low speed flows, small values of δ were used.

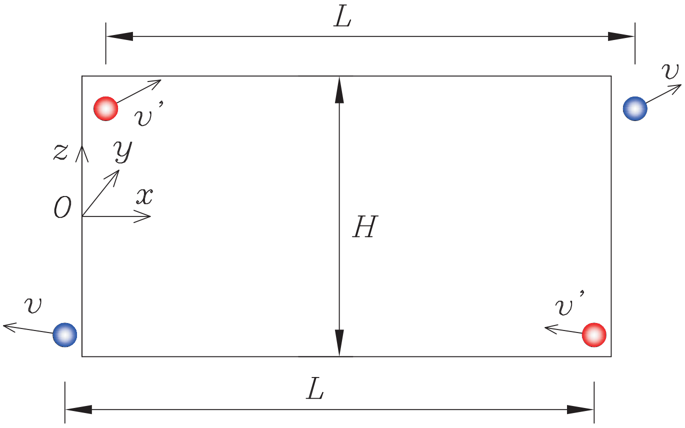

Figure 2.1: Modified periodic boundary conditions. The velocity v between the outgoing molecules are different from the ingoing molecules (Eq. 2.16 and 2.17)

Table 2.1: Summary of the boundary conditions applied on the simulation domain

	Boundary conditions
Faces x	Eqs. (2.16-2.17)
Faces y	PBC
Faces z	Thermal walls

2.5 Numerical results

2.5.1 Simulation of ideal gas flows

To model the interaction between the molecules, the 6-12 Lennard Jones potential is used:

$$V(r) = 4\epsilon \left[\left(\frac{\sigma}{r}\right)^{12} - \left(\frac{\sigma}{r}\right)^{6} \right], \tag{2.18}$$

where ϵ is the depth of the potential well, σ is the finite distance at which the inter-particle potential is zero, and r is the distance between the particles.

The potential well depth parameter is $\epsilon = 0.1\epsilon_0$ with ϵ_0 being the reference potential well depth. Two cutoff distances were used in this study : $r_c = 2^{1/6}\sigma$ [45] corresponds to repulsive interactions between molecules while $r_c = 2.5\sigma$ [47, 60, 61] corresponds to attractive-repulsive interactions. In general, the present method is valid for any pair potential. However, the simulation conditions of Table 2.2, i.e. $(\epsilon = 0.1\epsilon_0, 2^{1/6}\sigma)$, lead to a very small potential part of the pressure p_V (less than 1 % of the kinetic part p_K) making the behavior of the fluid close to an ideal gas.

Table 2.2: Input data for the first series of MD simulations.

N	L $[\sigma]$	B $[\sigma]$	H $[\sigma]$	Kn	δ $[\epsilon_0/m\sigma]$	γ $[\epsilon_0/m\sigma]$
2400	86.2	6.5	43.1	0.05	10^{-3}	4.3×10^{-4}
600	43.1	6.5	21.5	0.1	2×10^{-3}	8.6×10^{-4}

$(\epsilon, r_c) = (0.1\epsilon_0, 2^{1/6}\sigma)$, $\bar{n} = 0.1\sigma^{-3}$, $T = 2\epsilon_0/k_b$

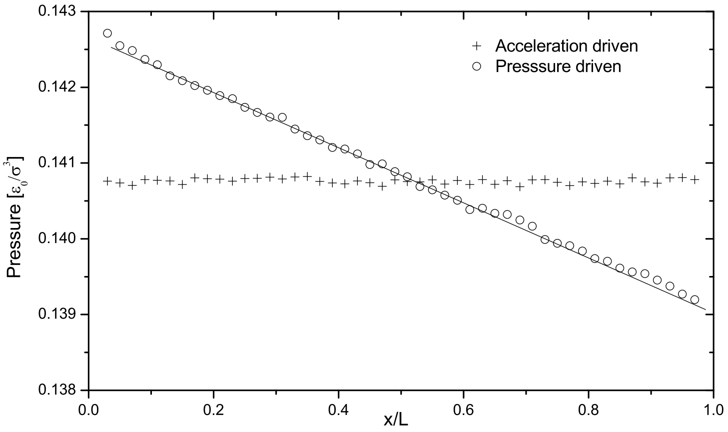

Figure 2.2: Pressure distribution $(\bar{p}(x))$ along the channel for pressure driven flow case and acceleration driven flow case (Kn = 0.05, $r_c = 2^{1/6}\sigma$, $\epsilon = 0.1\epsilon_0$, $\delta = 10^{-3}\epsilon_0/m\sigma$, $\gamma = 4.3\times10^{-4}\epsilon_0/m\sigma$). The full line represents the linear fit and is used to determine the pressure gradient $\Delta p/\Delta x$. The pressure unit is $[\epsilon_0/\sigma^3]$.

The two walls are modeled as thermally diffusive walls at the same and constant temperature. Whenever a molecule arrives at a wall, it is reflected with the velocity corresponding to the wall temperature $T_w = 2\epsilon_0/k_B$ and with a random direction. In this work, we do not use thermostats, the fluid can exchange energy with the wall due to the wall model described previously.

In our simulations, the global number density $\bar{n}$ is kept fixed, $\bar{n} = 0.1\sigma^{-3}$ in every configurations. Other geometric parameters like L, B, H and the number of the molecules N are changed as shown in Table 2.2. The values of δ are chosen such that the difference of the square of the molecular velocity between the inlet and outlet is small enough so that the stream velocity is much smaller than the thermal speed. From the microscopic viewpoint, the local stream velocity is the local average velocity of the molecules and from the macroscopic viewpoint, it is the flow speed $\mathbf{v}$ in the Navier Stokes equations and thus connected to the pressure gradient ∇p (or volume force $\rho\gamma$). On the other hand, the thermal speed is the root mean square of the molecular velocity and is directly connected to the local temperature T. The slope of the simulated total pressure distribution along of the channel (see Fig. 2.2 and 2.3) is used to determine the pressure gradient $-\Delta p/\Delta x$ and the equivalent external acceleration $\bar{\rho}\gamma$ used in the accelerationdriven flow simulations. The quantity $\bar{\rho}$ is the average mass density of the system, $\bar{\rho} = m\bar{n}$. The computation with Leap-Frog Verlet integration scheme is carried out for 10^8 time steps from equilibrium, each of which is equal to 0.005 unit time $\tau = \sqrt{m\sigma^2/\epsilon_0}$. The height and length of the channel are divided into 50 layers to determine accurately the distribution of local velocity $\mathbf{v}$, temperature T and pressure tensor $\mathbf{P}$. The local velocity $\mathbf{v}$ measured in one bin located at $\mathbf{r}$ is given by

$$\mathbf{v}(\mathbf{r}) = \frac{1}{n_{bin}} \sum_{\mathbf{r}_i \in bin} \mathbf{v}_i \ , \tag{2.19}$$

n_{bin} being the particle number in the bin. The local pressure $\mathbf{P}$ ($IK1$-model) is:

$$\mathbf{P}(\mathbf{r}) = \frac{1}{V_{bin}} \left[\sum_{\mathbf{r}_i \in bin} m(\mathbf{v}_i - \bar{\mathbf{v}}) \otimes (\mathbf{v}_i - \bar{\mathbf{v}}) - \frac{1}{2} \sum_{\mathbf{r}_i \in bin} \mathbf{r}^{(ij)} \otimes \mathbf{f}^{(ij)} \right] . \tag{2.20}$$

The pressure components were also computed by using the method of plane [45, 62]. With α, β being x, y or z, the pressure component $P_{\beta\alpha}$ along direction β and acting on the area element A_α normal to the axis α is defined by:

$$P_{\beta\alpha}(\mathbf{r}) = \frac{1}{\tau A_\alpha} \sum_{\mathbf{r}_i \in A_\alpha} m(v_{i\beta} - \bar{v}_{i\beta})(v_{i\alpha} - \bar{v}_{i\alpha})/v_{i\alpha} + \frac{1}{\tau A_\alpha} \int dt \sum_{r_{ij} \cap A_\alpha, i<j} f_\beta^{(ij)} \ . \tag{2.21}$$

In Eq. 2.21, the first sum is for all molecules crossing the area element A_α over the period τ, and the second sum is for all pairs whose distance vectors cut the area element A_α. The temperature T of one bin is then calculated by

$$T(\mathbf{r}) = \frac{m}{3k_B} \langle \| \mathbf{v} - \bar{\mathbf{v}} \|^2 \rangle_{bin} \ . \tag{2.22}$$

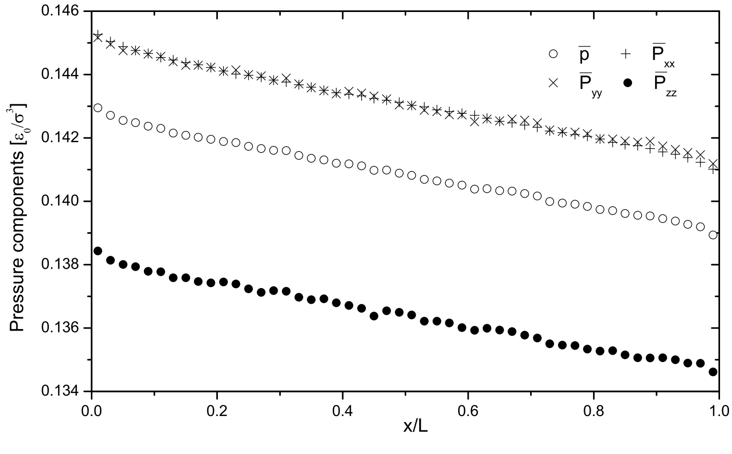

Figure 2.3: Distribution of pressure $\bar{p}(x)$ and pressure components $\bar{P}_{xx}(x), \bar{P}_{yy}(x), \bar{P}_{zz}(x)$ along the channel for pressure driven flow case (Kn = 0.05, $r_c = 2^{1/6}\sigma$, $\epsilon = 0.1\epsilon_0$, $\delta = 10^{-3}\epsilon_0/m\sigma$). The pressure unit is $[\epsilon_0/\sigma^3]$.

In what follows, the x-distributions of pressure, temperature and density correspond to an average on y and z of the local quantities $p(\mathbf{r})$ and $n(\mathbf{r})$. They are denoted as $\bar{p}(x) = \langle p(\mathbf{r})\rangle_{y,z}$ and $\bar{n}(x) = \langle n(\mathbf{r})\rangle_{y,z}$, respectively. Analogously, the profile along z of velocity, temperature and density correspond to an average on x and y of local quantities with the notations: $\bar{v}(z) = \langle v(\mathbf{r})\rangle_{x,y}$, $\bar{T}(z) = \langle T(\mathbf{r})\rangle_{x,y}$ and $\bar{n}(z) = \langle n(\mathbf{r})\rangle_{x,y}$, respectively.

From the simulations, the axial pressure distribution is plotted in Fig. 2.2 for the pressure driven and the acceleration driven flows with Kn $= 0.05$, $r_c = 2^{1/6}\sigma$. As expected, for the acceleration driven flow case, the pressure is constant. In contrast, the pressure distribution for pressure driven flow decreases linearly. We note here that the slope of the pressure curve, equal to $\Delta\bar{p}/\Delta x$, is used to compute the value γ in the acceleration flow simulation according to the formula $\gamma = -\Delta\bar{p}/(\bar{\rho}\Delta x)$. Under the simulation conditions $\bar{n} = 0.1\sigma^{-3}$, $T_w = 2\epsilon_0/k_B$ and $r_c = 2^{1/6}\sigma$, $\epsilon = 0.1\epsilon_0$, the kinetic part p_K of the pressure dominates.

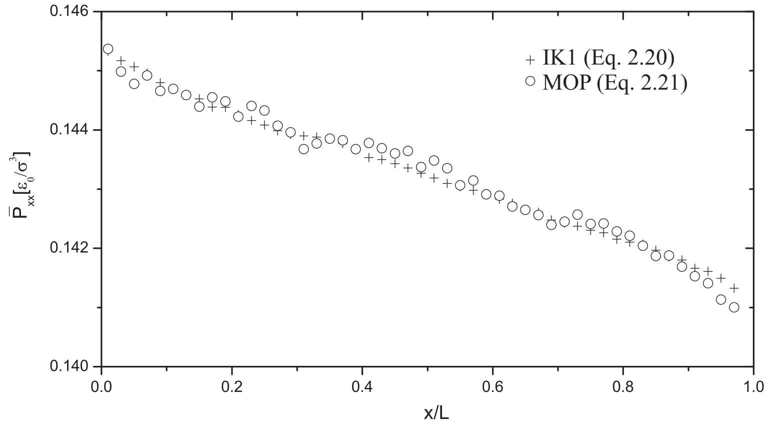

Figure 2.4: Distribution of pressure $\bar{P}_{xx}$ along the channel for pressure driven flow case (Kn $= 0.05$, $r_c = 2^{1/6}\sigma$, $\epsilon = 0.1\epsilon_0$, $\delta = 10^{-3}\epsilon_0/m\sigma$) computed by Eq. 2.20 and 2.21. The pressure unit is $[\epsilon_0/\sigma^3]$.

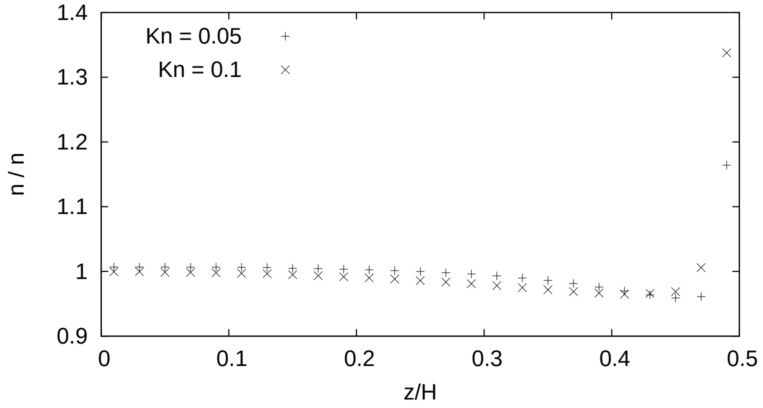

Figure 2.5: Dimensionless density profile ($\bar{n}(z)$) in half of the channel cross-section for pressure driven simulations (Kn=0.05, 0.1, $r_c = 2^{1/6}\sigma$, $\epsilon = 0.1\epsilon_0$, $\delta = 10^{-3}\epsilon_0/m\sigma$, $2 \times 10^{-3}\epsilon_0/m\sigma$).

In order to know how the pressure difference is distributed in the x, y, z-directions , the pressure components $\bar{P}_{xx}, \bar{P}_{yy}, \bar{P}_{zz}$ along x are plotted in Fig. 2.3. All the three pressure components decrease with x and the slopes are almost the same. The values of components $\bar{P}_{xx}, \bar{P}_{yy}$ are very close whereas the value of component $\bar{P}_{zz}$ is smaller because the fluid is confined in z-direction. Although the difference between the pressure components is small (less than 4%), it implies that the velocity distribution deviates from the equilibrium distribution. Because the pressure $\bar{p}$ is the average value of $\bar{P}_{xx}, \bar{P}_{yy}, \bar{P}_{zz}$, the $\bar{p}$-curve lies between the others and have the same slope. It should be noted that equations 2.20 and 2.21 leads to relatively close results when considering the average axial pressure component $\bar{P}_{xx}$ (see Fig. 2.4). Figure 2.5 shows that the fluid density distribution $\bar{n}(z)$ across the channel width varies slightly around the average density $\bar{n}$, except near the walls where it can be as high as $1.4\bar{n}$. However, the phase diagram for LJ fluid [61] shows that the fluid near the wall is still in gas state. In our simulations, $\bar{n}$ and ϵ are chosen to be very small ($\bar{n} = 0.1\sigma^{-3}, \epsilon = 0.1\epsilon_0$) and the fluid temperature near the wall is relatively large (the temperature of the wall is $T_w = 2\epsilon_0/k_B$). The fluctuation of the density profile shows that the incompressibility assumption is no longer valid, especially near the channel walls. However, the fluctuations being localized, it is interesting to check if the analytical solutions presented in Section 2 still agree with the MD solutions.

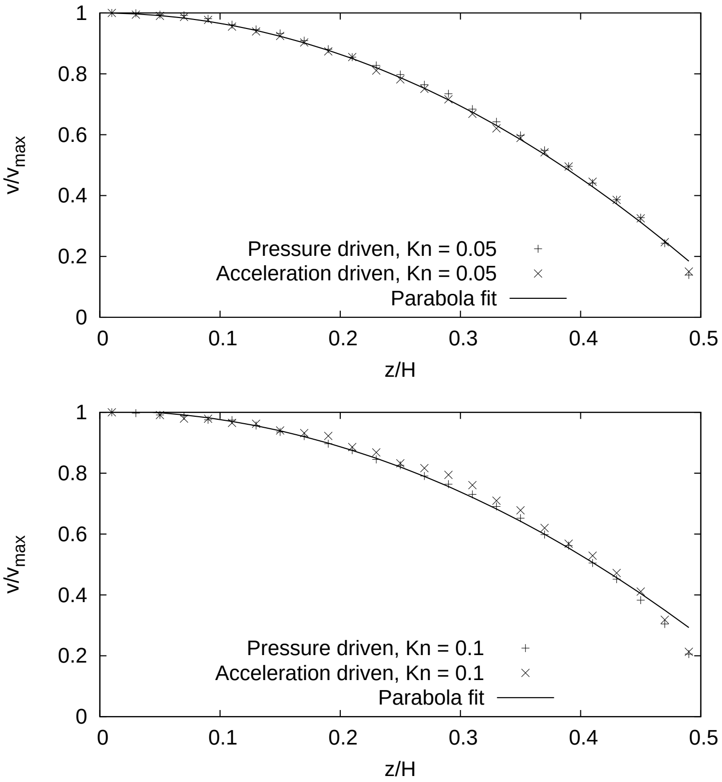

Figure 2.6: Dimensionless velocity profile in half of the channel cross-section for Kn=0.05 and $Kn = 0.1$, ($r_c = 2^{1/6}\sigma$, $\epsilon = 0.1\epsilon_0$). The full lines represent equation $v(\hat{z}) = v(0)(1 - a_2\hat{z}^2)$ that best fit the numerical results ($a_2 = 0.18$ for Kn=0.05 and $a_2 = 0.29$ for Kn=0.1).

Figure 2.6 shows that acceleration and pressure-driven flows exhibit parabola-like velocity profiles in the center region of the channel, in agreement with Eq. 2.1. Near the wall where the Knudsen layer dominates, the velocity distribution tends to deviate from the solution given by Eq. 2.1 and a velocity slip at the wall is predicted. Based on the kinetic theories, different models have been derived to explain the slippage [12] and generally, the slip effect becomes important when the Knudsen number increases. The little difference in velocity profile between the two types of flow show that, despite their different microscopic natures, volume forces can be seen as equivalent to pressure gradients at the macroscopic scale.

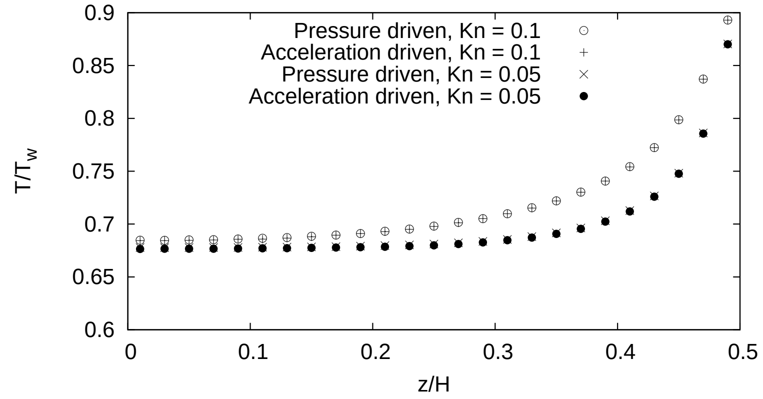

Figure 2.7: Dimensionless temperature profile ($\bar{T}(z)$) in half of the channel cross-section for two Kn-values according to the flow model ($r_c = 2^{1/6}\sigma$, $\epsilon = 0.1\epsilon_0$).

Regarding the temperature profile across the channel width, there is no visible difference between acceleration and pressure-driven formulations whatever Kn (Fig. 2.7). The temperature profile cannot be fitted by any of the three approximate analytical solutions (Eq. 2.2-2.4). The temperature is minimal at the center of the channel and increases rapidly near the wall, which does not agree with the approximate solutions obtained with the incompressible assumption (Eq. 2.2-2.3). With the simulation conditions reported in Table 2.2, this reverse trend cannot thus be explained by using the incompressible flow equations. This anomaly was also observed by using DSMC method [63] and Super-Burnett (SB) method [64]. Note that the flow speeds in our simulations are very small, as in [63, 64].

Next, we study the influence of γ and δ on the temperature profile. By increasing the acceleration parameter γ or the δ-parameter (squared velocity,) the stream velocity is increased. A change in the form of the temperature profile is observed in Fig. 2.8 and 2.9 as γ (or δ) increases. At high values of γ (or δ), the temperature profiles seem to be closer to the approximate solutions which predict a maximum at the center of the channel and a minimum at the walls. At small values of γ (or δ), the temperature profiles for the two flow types differ just a little. However, at high values of γ (or δ), the discrepancy becomes more important: the curvature at the center of channel for the pressure driven flow case is higher than that for the acceleration driven flow case. Using curve fitting procedure, we find that the temperature profile of the pressure driven flow case agrees quite well with the quartic expression (Eq. 2.3). The temperature for the acceleration driven flow case does not fit well with Eq. 2.2. To explain this discrepancy, Todd and Evans [48] argued that the transport coefficients are not constant and there exist an additional cross-coupling between strain rate and heat flux. They proposed a correction to (Eq. 2.3) with a z^6-extra term for the temperature profile (see Eq. 2.4). The dashed line drawn in Fig. 2.9 shows that the sextic polynomial fit very well the present numerical results.

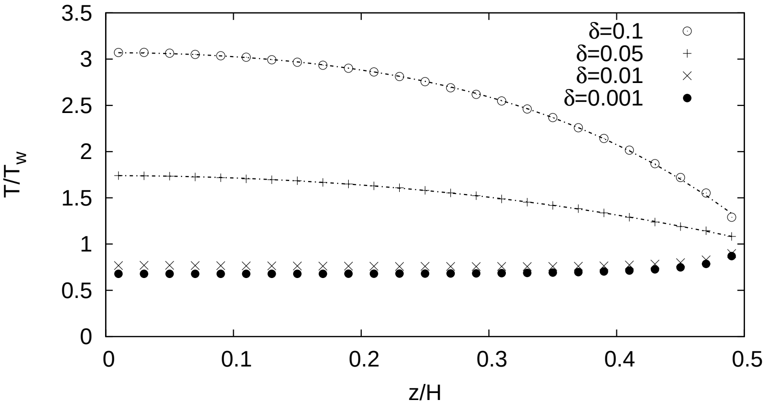

Figure 2.8: Variation of temperature profile when increasing the pressure gradient or parameter δ (Kn $= 0.05$, $r_c = 2^{1/6}\sigma$, $\epsilon = 0.1\epsilon_0$). The dashed lines are based on equation $c_0 - c_2\hat{z}^2 - c_4\hat{z}^4$ that best fits the numerical results. $c_0 = 3.07$, $c_2 = 4.16$, $c_4 = 12.8$ for $\gamma = 0.1\epsilon_0/m\sigma$, $c_0 = 1.74$, $c_2 = 2.5$, $c_4 = 1.0$ for $\gamma = 0.05\epsilon_0/m\sigma$.

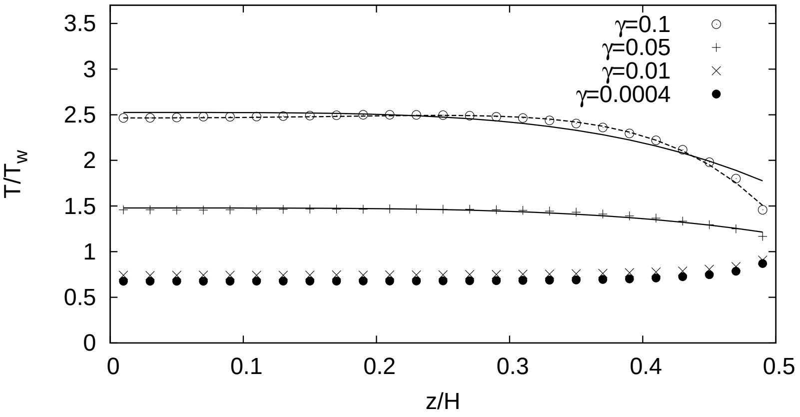

Figure 2.9: Changes in the temperature profile for various values of the acceleration parameter γ (Kn $= 0.05$,$r_c = 2^{1/6}\sigma$, $\epsilon = 0.1\epsilon_0$). The solid and the dashed lines correspond to equations $b_0 - b_4\hat{z}^4$ and $d_0 - d_2\hat{z}^2 - d_4\hat{z}^4 - d_6\hat{z}^6$ that best fit the numerical results. $b_0 = 2.53$, $b_4 = 13.0$, $d_0 = 2.46$, $d_2 = 0.54$, $d_4 = 4.58$, $d_6 = -97.8$ for $\gamma = 0.1\epsilon_0/m\sigma$ and, $b_0 = 1.48$, $b_4 = 4.57$ for $\gamma = 0.05\epsilon_0/m\sigma$.

2.5.2 Applications to general cases

The application of the method to cases for which the fluid particles interact strongly, i.e the potential pressure p_V is of the order of p_K, is considered in that section. The case of rib-roughened channels is also briefly discussed.

With the algorithm developed in the previous section, two cases were considered with the same parameters, except for the cutoff distance r_c and density number $\bar{n}$. In the first case, $\bar{n} = 0.1\sigma^{-3}$ and the cutoff distance is set to $r_c = 2.5\sigma$ (attractive-repulsive interaction). In the second case, the fluid density is increased up to $\bar{n} = 0.8\sigma^{-3}$ while seting $r_c = 2^{1/6}\sigma$ as in the previous section. The well depths ϵ are the same in both cases and equal to the reference value, i.e $\epsilon = \epsilon_0$. All the parameters for these two cases are summarized in Table 2.3.

Table 2.3: Input data for MD simulations in Section 2.5.2

$\bar{n}$ $[\sigma^{-3}]$	N	L $[\sigma]$	B $[\sigma]$	H $[\sigma]$	δ $[\epsilon_0/m\sigma]$	T_w $[\epsilon_0/k_b]$
0.1	2400	86.2	6.5	43.1	1×10^{-3}	2
0.8	2400	86.2	3.2	43.1	1×10^{-3}	2

$(\bar{n}, \epsilon, r_c) = (0.1\sigma^{-3}, \epsilon_0, 2.5\sigma), (0.8\sigma^{-3}, \epsilon_0, 2^{1/6}\sigma)$

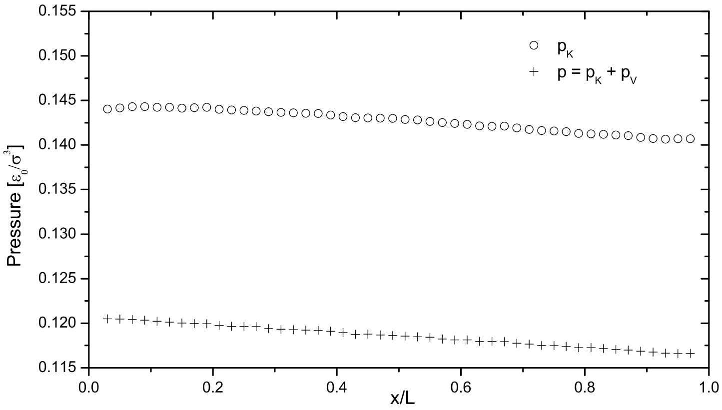

Figure 2.10: Axial variations of pressures $\bar{p}(x) = p_K + p_V$ and p_K for pressure driven flow ($\bar{n} = 0.1\sigma^{-3}$, $r_c = 2.5\sigma$, $\epsilon = \epsilon_0$). The pressure unit is $[\epsilon_0/\sigma^3]$.

In the first case ($\bar{n} = 0.1\sigma^{-3}$), figure 2.10 displays the kinetic part $\bar{p}_K$ and the virial pressure $\bar{p}$ according to Eq. 2.9 along the channel. Except a slight curvature in the $\bar{p}_K$ curve, both pressure curves decrease continuously and linearly. The relative difference between the slopes of both curves is less than 1%, which means that the gradient of the potential part $\Delta\bar{p}_V/\Delta x$ is also small in comparison with the kinetic part $\Delta\bar{p}_K/\Delta x$ even if $\bar{p}_V$ is not negligible ($|\bar{p}_V/\bar{p}_K| \simeq 0.2$). In the second case ($\bar{n} = 0.8\sigma^{-3}$), Figure 2.11 shows a totally reverse trend: both the virial pressure profile and its potential part decrease with x. The variation of the potential part contributes to 80% of the virial pressure variation with $\Delta\bar{p}/\Delta x = -0.0177$ and $\Delta\bar{p}_V/\Delta x = -0.0159$. We conclude that the method is convenient

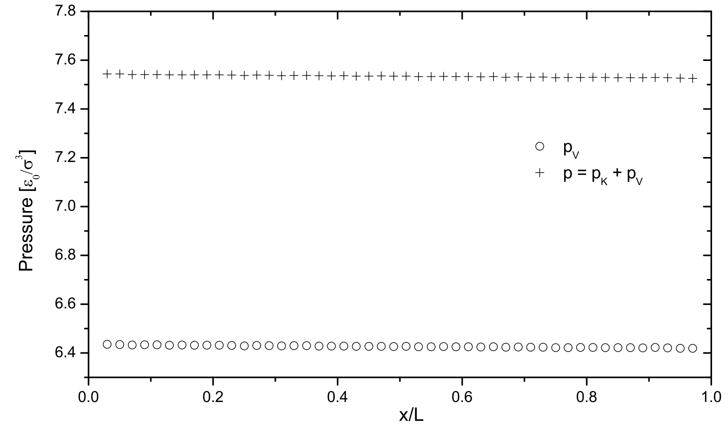

Figure 2.11: Axial variations of pressures $\bar{p}(x) = p_K + p_V$ and p_V for pressure driven flow ($\bar{n} = 0.8\sigma^{-3}$, $r_c = 2^{1/6}\sigma$, $\epsilon = \epsilon_0$). The pressure unit is $[\epsilon_0/\sigma^3]$.

for generating virial pressure profiles which decrease in the axial direction.

Next, we consider the velocity profiles across the channel section for these two cases. The velocity profiles (Fig. 2.12) agree then with Eq. 2.1. The slip length for the case $\bar{n} = 0.8\sigma^{-3}$ is smaller than for the case $\bar{n} = 0.1\sigma^{-3}$ because the mean free path is decreased when the density number is increased. When computing the average pressure component $\bar{P}_{xx}$ along the channel, figure 2.13 shows that there is no visible difference between equations 2.20 and 2.21

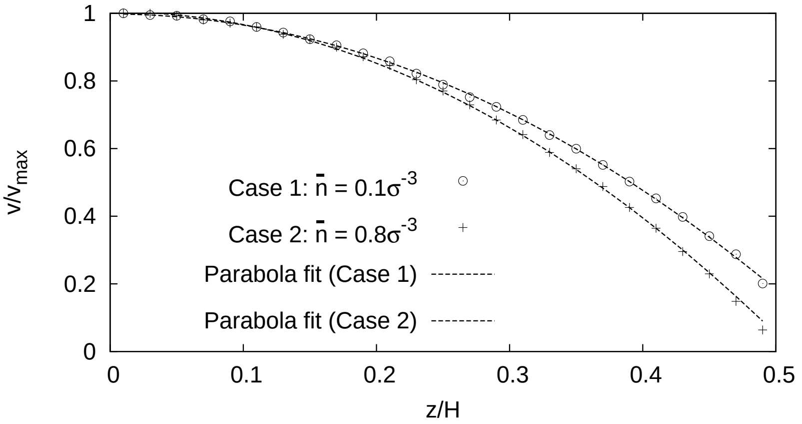

Figure 2.12: Dimensionless velocity profile in half of the channel cross-section for $\bar{n} = 0.1\sigma^{-3}$ and $\bar{n} = 0.8\sigma^{-3}$. The dashed lines represent the equations $a_0 - a_2 z^2$ that best fit the numerical results.

It should thus be emphasized that the present method is relevant to generate various fluid flows even if we control only the difference in squared molecular velocity. It does not imply that the potential part p_V, which depends on the interatomic interaction, does not vary along the flow direction. As shown numerically, the variation of p_V contributes considerably to the pressure gradient.

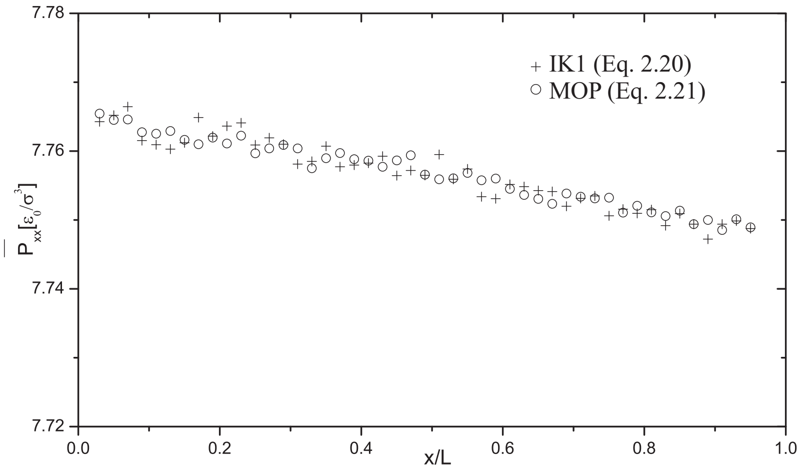

Figure 2.13: Axial variations of pressure component $\bar{P}_{xx}$ computed by Eq. 2.20 and 2.21. The pressure unit is $[\epsilon_0/\sigma^3]$.

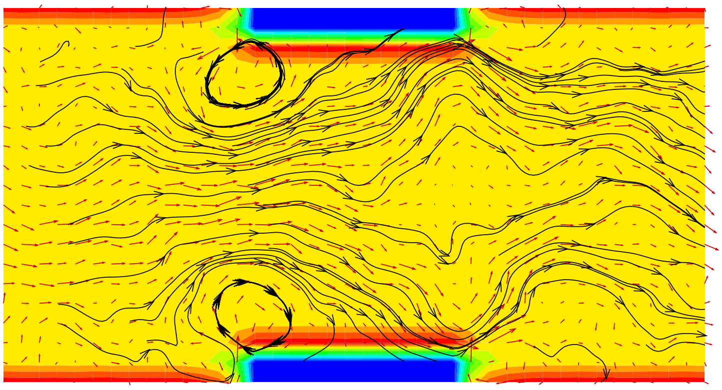

Figure 2.14: Streamlines in a rib-roughened channel. The color represents the fluid density field.

The third case aimed at modeling the flow within a rib-roughened channel. The parameters are the same as in the second case ($\bar{n} = 0.8\sigma^{-3}$, $r_c = 2^{1/6}\sigma$) but the channel height is suddenly reduced in its middle part by inserting on both walls ribs of height h and length l. The rib-to-channel width ratio is equal to $h/H = 0.8$ and $l/L = 0.3$ (Fig.2.14). Figure 2.14 exhibits the onset of two vortices close to the rib corners at the upstream section. It is also shown that the fluid flow is highly non uniform and characterized by wavy streamline patterns within the downstream region. From Fig. 2.15, the axial pressure variations are rather different from those predicted for smooth channels. Although the variations of the axial pressure predicted by the two expressions are quite similar, there are considerable differences between them. The MOP pressure is 8% smaller than the IK1 pressure. The changes in pressure at the downstream and upstream sections display also smoother pressure variations. This considerable difference is due to the strong inhomogeneity of the fluid within the channel. Generally, the MOP, based on the hydrodynamics equation, must be used in such situation.

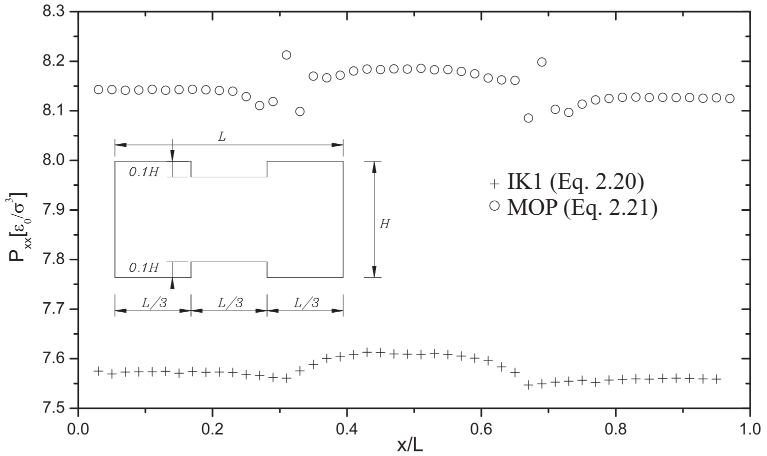

Figure 2.15: Distribution of pressure component $\bar{P}_{xx}$ in a rib-roughened channel computed by Eq. 2.20 and 2.21. The pressure unit is $[\epsilon_0/\sigma^3]$.

Chapter 3

Gas-wall potential and effects on the accommodation coefficient

3.1 Introduction

As mentionned in Chapter 1, Maxwell introduced a gas-wall momentum accommodation parameter σ_t (TMAC) to quantify the slip effects [16]. He postulated that after collision with the wall, a gas atom rebounds either diffusively or specularly, with the associated portions of σ_t and $1 - \sigma_t$, respectively. Although Molecular Dynamics simulations showed that the reflection mechanism is more complicated than Maxwell's postulate, the coefficient σ_t is still widely used due to its simplicity. For example, in the case of isothermal flows, Eq. (1.28) is reduced to

$$U_{slip} = \frac{2 - \sigma_t}{\sigma_t} \mathrm{Kn} \left(\frac{\partial U}{\partial n} \right)_s . \tag{3.1}$$

With MD method, the accommodation parameter can be computed either indirectly or directly. The former concerns the simulation of confined flows [51, 65], finding the slip velocity and using slip equation (3.1) to calculate σ_t . The latter method consists in projecting a gas atom with velocity $\mathbf{v}_i$ into a surface, measuring the reflected velocity $\mathbf{v}_r$, and computing σ_t [66]. However, the success of the MD method relies on the accuracy of the interaction potential of the gas-wall couple into consideration. The choice of such potential for a MD simulation is crucial. This interaction potential can be either determined by quantum electronic structure calculations or elaborated to reproduce experimental data with some empirical parameters.

Based on periodic density functional theory computations, a Pt-Ar potential is developed for MD simulations. Other pairwise potentials from the literature will be also considered to discuss what kind of interaction potentials should be used for correct MD simulations and what are the consequences of the choice of a given potential.

We have chosen the Pt-Ar couple because a number of references exist about the interaction potential between the Pt(111) surface and an Ar atom. In particular, the Pt(111)-Ar couple has been widely involved in MD simulations of atomic beam experiments [67–74] or of slip flows [65, 75–78], as examples. A section of the present chapiter is devoted to a brief review of the existing Pt-Ar pairwise potentials.

3.2 Interaction potentials

3.2.1 Previous works

Experimentally, only few data exist about the interaction of an Ar atom with a Pt(111) surface. Zeppenfeld *et al.* [79] measured the vertical vibrational frequency of the adsorbed atom at about 5 meV from inelastic He scattering on Ar monolayer physisorbed on Pt(111). To the best of our knowledge, the first reference to the total adsorption energy appeared in the work of Head-Gordon *et al.* [68] who reported a Ar on Pt(111) binding energy of about 80 meV (7.5 kJ.mol^{-1} or 900 K). Zeppenfeld *et al.* [80] mentioned a value of 96 meV from unpublished results of Zeppenfeld, Kern and Becher. Most of the empirical potentials have been optimized in order to reproduce the 80 meV binding energy and experimental results on trapping, desorption and scattering of Ar on Pt(111).

In the following, we give a brief description of the previous interaction potentials between Ar and Pt(111). $\mathbf{r}$ represents the position of the Ar atom, $\mathbf{r}_i$ the position of the ith Pt atom and z is the normal distance of Ar above the surface. Most of the potentials given below are empirical and Table 3.1 contains the associated parameters.

Head-Gordon *et al.* [68] have employed Morse type functions to reproduce the experimental measurements about the trapping and desorption of the Ar atom on the Pt surface, as well as the binding energy of 80 meV. They assumed that the incorrect form of the attractive part of this potential does not play a crucial role for trapping or scattering:

$$V_{Head-Gordon} = D_e \sum_i \left(\exp[-2\sigma(|\mathbf{r}-\mathbf{r}_i| - R_0)] - 1\right)^2 \ , \tag{3.2}$$

where D_e is the dissociation energy parameter which controls the strength of binding and σ is the strength parameter which is linked to the efficiency of energy transfer between gas and surface. It must be noticed that Yamamoto [75] used this Morse potential for the study of the slip flow of Ar on Pt(111), but with a twice too large value for σ.

The most common empirical potentials used for MD are Lennard-Jones 6-12 potentials, in order to obtained a better representation of the long-range attractive part that can be important in the simulation of the fragmentation of clusters or droplets:

$$V_{LJ} = 4\epsilon \sum_i \left[\left(\frac{\sigma}{|\mathbf{r}-\mathbf{r}_i|} \right)^{12} - \left(\frac{\sigma}{|\mathbf{r}-\mathbf{r}_i|} \right)^{6} \right] \ , \tag{3.3}$$

ϵ is the depth of the potential well and σ is the finite distance at which the pair potential is zero. As examples, Svanberg and Pettersson [81] have optimized parameters such that the interaction potential reproduces the one of Head-Gordon *et al.* [68] in order to model the scattering of Ar clusters from the Pt(111) surface. Maruyama and Kimura [73, 74], and Spijker *et al.* [76] have suggested values for σ and ϵ for the simulation of nucleation of Ar liquid droplets on Pt surface. Ramseyer *et al.* [82] have also derived a Lennard-Jones type potential from the experimental data derived by Zeppenfeld *et al.* [79, 80].

More elaborated interaction potentials have also been derived. For a MD study of the trapping and scattering of Ar on Pt(111), Smith *et al.* [69] used an interaction potential between the Ar atom and the Pt surface defined as a sum of pairwise repulsive terms and a non-corrugated van der Waals attractive part:

$$V_{Smith} = \sum_i V_0 e^{-\alpha(|\mathbf{r}-\mathbf{r}_i|)} - \frac{-C_{vdW}}{\sqrt{(z-z_0)^6 + (C_{vdW}/V_{min})^2}} \ . \tag{3.4}$$

The parameters were chosen such that $C_{vdW} = 2.3697$ eV.Å^2, evaluated from the Ar polarizability and the Pt dielectric function. Kulginov *et al.* [71] determined an empirical potential energy function for the Pt(111)-Ar system based on atomic beam scattering data, the measured well depth, and the vibrational frequency of the absorbed atom by Comsa *et al.* [68, 79]. This function is composed of a pairwise sum of non-central potentials. The repulsive pair potential has the Buckingham form [36]:

$$V_{Kulginov} = \sum_i \left(V_0 e^{-\alpha(|\mathbf{r}-\mathbf{r}_i|-r_0)} - D(r)\frac{C_6}{|\mathbf{r}-\mathbf{r}_i|^6} \right) \ , \tag{3.5}$$

and the attractive part corresponds to the van der Waals attraction multiplied by a damping function $D(r)$. C_6 is chosen such that the total potential reproduces the van der Waals attraction calculated by Smith *et al* [69]. They suggested also that their and the Head-Gordon functions [68] should by shifted by ≈ -0.7 Å to better agree with the sum of the van der Waals radii of the Ar and Pt atoms. They confirmed that the position of the potential well can not be determined by the scattering data alone and that electronic structure calculations should be made. From the *ab initio* point of view, only Lahaye [70] have used Hartree-Fock calculations on Ar approaching a Pt_4 cluster to derive a Pt(111)-Ar interaction potential with a similar form to the one of Smith *et al.* [69] (see equation (3.4)).

3.2.2 Computational approach

As explained in the previous section, several potentials exist for the Pt(111)-Ar interaction, most of them being obtained empirically since the computation of such interaction potential still remains a challenging task. In order to fill this lack, large periodic computations using the density functional theory approach have been performed. All these electronic structure computations were done with the CRYSTAL09 code [83] using the PBE functional revised for the study of solids (PBEsol) [84]. For the description of the Pt atoms, the pseudo-potential and basis set introduced by Doll [85] to investigate the absorption of CO on a Pt(111) surface was used. For the Ar atom, the all electron basis set developed by Nada *et al.* [86] was chosen. As a starting point of these computations, the lattice parameter of a platinum bulk was investigated to check the accuracy of the methodology used. At this level of calculation, the equilibrium lattice parameter is obtained at $a = 3.96$ Å. That is in relatively good agreement with the experimental value of 3.92 Å [87], and consistent with those computed by Doll [85] at 4.01 Å and 4.05 Å using the PW91 and B3LYP functionals, respectively.

The pairwise potential cannot be obtained directly from quantum chemistry calculations since the interaction of an Ar atom with an isolated Pt atom is strongly different of an interaction of an Ar atom with an Pt atom embedded in a surface slab. A way to obtain the pairwise interaction potential between a gas atom and a surface atom is to decompose of the Pt(111)-Ar potential in two bodies term. To this end, the Pt(111)-Ar interaction was modeled by using a super-cell representing a three-layer Pt slab, the Pt atoms being arranged as in the face-centered cubic lattice, with the PBEsol optimized platinum bulk lattice parameter of 3.96 Å. The Ar atom was adsorbed on one side of the slab, vertical to the (111) surface in front of a fcc-hollow site. On this site, the Ar atom is placed vertically above a Pt atom of the third Pt layer. We have checked that the adsorption energy is little sensitive to the adsorption site, the variation in the adsorption energy being of 7 meV between the top and fcc-hollow sites. Several slab sizes have been tested. The (4x4x3) slab

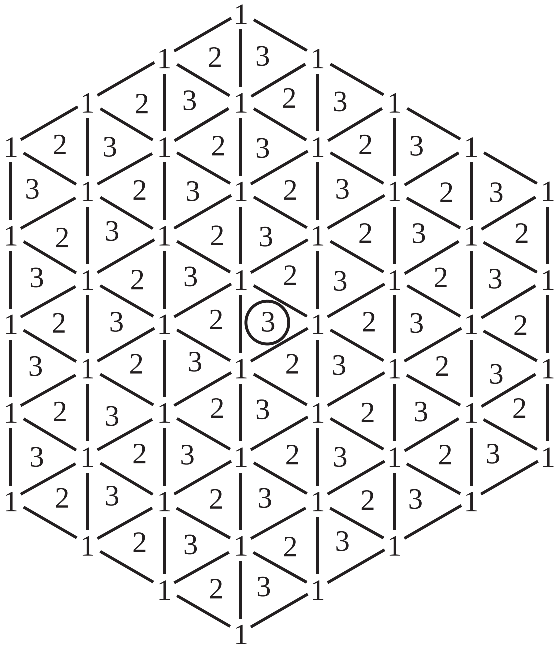

Figure 3.1: Scheme of the Pt cluster used to decompose the global Pt(111)-Ar interaction potential on a sum of two bodies Pt-Ar terms used for the molecular dynamics. The circle represents the argon atom adsorbed on the fcc-hollow site, numbers 1 represent platinum atoms of the first layer, numbers 2 Pt atoms of the second layer, and numbers 3 Pt atoms of the third layer, respectively.

appears to be a good compromise between accuracy of the interaction energy and computational effort. Using this (4x4x3) slab, the distance between two Ar atoms is about 11.2 Å, about three times larger than the equilibrium distance of the diatomic Ar_2 molecule (R_e(Ar-Ar) = 3.76 Å [88]). The relaxation of the first layer was not considered according to the work of Doll [85] showing the very small change in the binding energy due to such a relaxation. Finally, a k-point sampling net of size 16 x 32 was used, and the Fermi function was smeared with a temperature of 0.01 E_h to improve the convergence of the total energy with respect to k-point sampling and the convergence of the Pt(111) surface energy with respect to the number of layers [83].

The resulting computed energies have been fitted by a sum of pairwise functions in order to reproduce the Pt(111)-Ar interaction potential.

$$V^{Pt(111)-Ar}(z) = \sum_i V^{Pt-Ar}(|\mathbf{r} - \mathbf{r}_i|) \ , \tag{3.6}$$

z is the distance between the Ar atom at the vertical of the fcc-hollow site and the first layer of the Pt(111) surface. $z = 0$ is defined as the position of the Pt nuclei of this first layer for $T = 0K$. The sum is made over all of the 121 Pt atoms of the cluster depicted in Figure 3.2.2 which is supposed to reproduce the Pt(111) surface. According to the previous empirical pairwise potentials, a similar function (see equation (3.7)) as the one used by Kulginov et al. [71] has been employed to fit the computed energies.

$$V^{Pt-Ar}(r) = V_0 e^{-\alpha(r-r_0)} - \frac{C_6}{r^6} \ , \tag{3.7}$$

Table 3.1: Pt(111)-Ar interaction potential parameters.

$\sum$Rep + vdW	V_0 (eV)	α (Å^{-1})	C_{vdW} (eV.Å^3)	z_0 (Å)	V_{min} (eV)
Smith [69]	900	3.2	2.3697	0.65	0.3
Lahaye [70]	975.455	2.8	0.81	1.72	0.63
$\sum$ (Rep+vdW)	V_0 (eV)	α (Å^{-1})	r_0 (Å)	C_6 (eV.Å^6)	
Present work	0.00818	3.3	3.928	64.92	
Kulginov [71]	2000	3.3	-0.75	68.15	
Morse	D_e (meV)	2σ (Å^{-2})	r_0 (Å)		
Head-Gordon [68]	11.6	1.6	4.6		
Yamamoto [75]	11.6	3.2	4.6		
Lennard-Jones 6-12	ϵ (meV)	σ (Å)			
Ramseyer [82]	6.6	3.37			
Svanberg [81]	6.80	4.00			
Maruyama [73, 74]	5.58	3.085			
Spijker [76]	6.82	2.94			

with $r = |\mathbf{r}_{Ar} - \mathbf{r}_{Pt}|$. The fitted parameters are given in Table 3.1.

In Figure 3.2.2, the circle represents the Ar atom adsorbed on the fcc-hollow site, numbers 1 represent the Pt atoms of the first layer, numbers 2 the Pt atoms of the second layer, and numbers 3 the Pt atoms of the third layer. By considering the Ar atom at the vertical position above a fcc-hollow site of the Pt(111) surface, the system presents a third order rotation axis. This rotational symmetry is conserved for the construction of the Pt cluster used for the decomposition. The height of this cluster is 4.57 Å and its width is larger than 8.0 Å. When the Ar atom is close to its equilibrium position, the distance between the Ar atom and the more external Pt atoms of the cluster is more than 8.0 Å. For most of the pairwise potentials studied in this work, including the present potential, the pairwise interaction can be neglected for $r_{Pt-Ar} > 8.0$ Å. The convergence of the recomposed potential $V^{Pt(111)-Ar}(z)$ relative to the number of Pt atoms has been checked, in particular the addition of a fourth layer has a negligible contribution in the sum of equation (3.6). Moreover, $V^{Pt-Ar}(r)$ is expected to be adequate to reproduce the attractive part of the potential: the C_6 value of 64.92 eV.Å^6 obtained is consistent with the value of 68.15 eV.Å^6 chosen by Kulginov *et al.* [71] to reproduce the C_{vdW} value of Smith *et al.* [69] calculated from the polarizability of the Ar atom and the dielectric function of Pt.

3.3 Computation of TMAC by Molecular dynamics

In this section, we describe the MD method to simulate the gas-wall interaction and directly calculate the accommodation coefficient. Each gas-wall collision is treated separately as in most direct scattering experiments (see [67, 89]). This method is suitable for dilute gas for which it can be assumed that only one atom interacts with the wall in one collision event. In the three-dimensional MD simulation, the Ar atoms beams are projected with different incident angles on a clean Pt(111) surface lying on the *Oxy* plane. The $\hat{x}$ direction corresponds to the $< 110 >$ direction associated with the maximum Pt atom density direction, such that the distance between two atoms equals 2.772 Å.

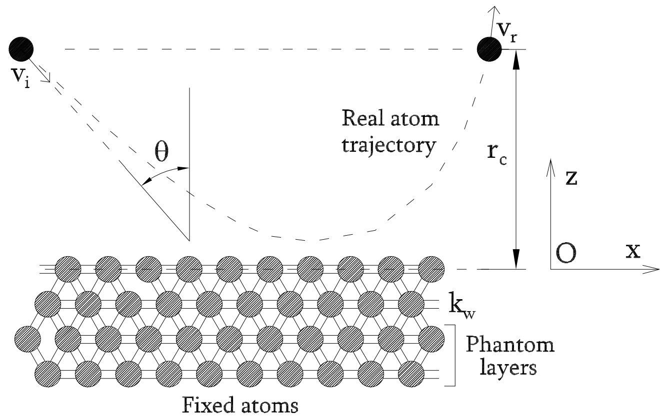

Figure 3.2: Molecular dynamics scheme. The incident argon atoms are with $\mathbf{v}_i$ velocities with no contribution along y. θ is the incident angle. The Pt wall has a fcc structure with a (111) surface. Each Pt atom is connected to the nearby ones by harmonic springs of rigidity k_w (see the text).

The *directional* σ_t^{dir} coefficient associated with each θ and φ is defined by the following formula [12]:

$$\sigma_t^{dir}(\theta, \varphi) = \frac{\langle v_{in} \rangle - \langle v_{rn} \rangle}{\langle v_{in} \rangle} \ , \tag{3.8}$$

where θ and ϕ are the zenithal and azimuthal angles, respectively. θ is the incident angle of the gas atom with the z axis, $\hat{n}$ is direction of the projection of the incident and reflected velocities on the Oxy plane, making an angle ϕ with the $\hat{x}$ direction. v_{in} and v_{rn} are the projections of the incident and the reflected velocities on $\hat{n}$, respectively.

$$v_{in} = v_i \sin(\theta), \quad v_{rn} = v_r \sin(\theta). \tag{3.9}$$

In order to model the Pt-wall and to maintain its temperature, a phantom wall technique [73, 74, 90] is used in this work. Each Pt atom is connected to the nearby ones by harmonic springs with rigidity k_w, allowing it to vibrate around its site. The wall structure is made of 924 atoms, arranged in (111) fcc four layers slab of size $40 \times 40 \times 6.77$ Å^3 (see Figure 3.3). The last two layers are the phantom layers, the lowest is fixed. The temperature of the bulk part of the wall, T_w, is controlled by a Langevin thermostat applied to the second phantom layer [91]. The motion of an upper phantom atom i is governed by the equation:

$$m_i \frac{d\mathbf{v}_i(t)}{dt} = -\xi \mathbf{v}_i(t) + \mathbf{f}_i(t) + \mathbf{R}_i(t) \ . \tag{3.10}$$

In equation (4.6), $\mathbf{v}_i$ is the velocity of the atom i, $\mathbf{f}_i$ is the resulting force acting on it by the surrounding ones, m_i is the atomic mass and ξ is the damping coefficient. The third term in the right hand side of equation (4.6) is then the random force applied on the atom. In the simulation, it is sampled after every time step δt from a Gaussian distribution with zero average and mean deviation of $\sqrt{6\xi k_B T_w / \delta t}$. The simulations were carried out by setting rigidity, time step and damping factor at the following values [90]:

$$k_w = 46.8 \text{ N/m}, \quad \delta t = 2 \text{ fs}, \quad \xi = 5.184 \times 10^{-12} \text{kg/s}. \tag{3.11}$$

The spring constant k_w has been optimized by Maruyama and Kimura to reproduce the physical properties of solid platinum [73, 74]. The phantom atoms technique allows to model the semi-infinitely large bulk solid kept at a constant temperature T_w with the proper heat conduction characteristics. We also checked that to add on two layers does not change the σ_t values. The gas velocity at each time step is calculated by the usual Leap-Frog Verlet integration scheme. For a given pair potential $V(R_{ij})$, we can compute the force vector $\mathbf{f}_{ij}$ that atom j at position $\mathbf{R}_j$ exerts on atom i at position $\mathbf{R}_i$ by:

$$\mathbf{f}_{ij} = -\frac{dV^{Pt-Ar}}{dr}\frac{\mathbf{r}_{ij}}{\|\mathbf{r}_{ij}\|} \ , \quad \mathbf{r}_{ij} = \ \mathbf{r}_i - \mathbf{r}_j \ . \tag{3.12}$$

The computational costs may be reduced by assuming that an Ar atom only interacts with the Pt wall within a cutoff distance r_c =12 Å, corresponding to a negligible attraction of about 0.02 meV. On the other hand, r_c is very small with respect to the mean free path. Initially, Ar atoms are given with a fixed incident velocity $\mathbf{v}_i$ defined in the Oxz plane and with a norm associated to the gas beam temperature T_g, such that

$$v_{i\tau} = \sqrt{\langle v_{i\tau}^2 \rangle} = \sqrt{\frac{k_B T_g}{m_{Ar}}} \ . \tag{3.13}$$

This value corresponds to the average value of the positive part of the incident velocity along the $\hat{\tau}$ direction. The wall temperature T_w is kept at 200 K, 300 K and 400 K and the gas beam temperature T_g is kept at a slightly higher value than T_w, here $T_g = 1.1 \times T_w$.

The Ar atoms are inserted randomly at the distance r_c with respect to the wall surface and their reflected velocity $\mathbf{v}_r$ is recorded when they bounce back beyond this cutoff distance. Whenever an Ar atom crosses this boundary, another one will be inserted with velocity $\mathbf{v}_i$. The process continues until we obtain a converged value of $\langle v_{rn} \rangle$, i.e. after approximatively 12000 collisions. A typical run requires 4×10^7 time steps of 2 fs. The periodic boundary conditions are applied along the x, y directions throughout the simulation.

3.4 Results and discussions

3.4.1 Interaction potentials

The Pt(111)-Ar interaction potential and the corresponding Pt-Ar pairwise potential calculated in the present work are plotted in Figures 3.3 and 3.4, respectively. The potentials described in the above referenced works (see Section 2.1) are also shown. Table 3.1 contains the fitted parameters and Table 3.2 presents the equilibrium interaction energies, V_e, the equilibrium value, z_e, of the Pt(111)-Ar distance and the vertical Pt(111)-Ar harmonic vibrational frequency, ω_e. These data are compared with those deduced from other potentials and with available experimental values ($V_e = -80$ meV and $\omega_e = 5$ meV [68, 79]). ω_e has been estimated from the second derivative of the interaction potentials at their respective minimum geometries, using the Ar mass as the reduced mass considering that the Pt surface has an infinite mass.

Figure 3.3 presents the Pt(111)-Ar potential computed together with those discussed in Section 2.1. Four types of potentials can be distinguished. The first ones are the Lennard-Jones potentials established by Maruyama and Kimura [73, 74] and by Spijker *et al.* [76]. They depict a relatively weak value of V_e, of ≈ -40 meV, and a short equilibrium $z_e < 3$ Å. The second group of potentials includes those of Head-Gordon *et al.* [68] and Svanberg

Table 3.2: Equilibrium interaction energy (V_e in meV), equilibrium distance (z_e in Å), and estimated vertical harmonic vibrational frequency (ω_e in meV) of the Pt(111)-Ar interaction potentials.

Potential	V_e / meV	z_e / Å	ω_e / meV
Present	-81.3	3.35	4.8
Kulginov [71]	-89.7	3.24	4.8
Ramseyer [82]	-72.8	3.22	5.0
Maruyama [73, 74]	-38.4	2.93	3.9
Spijker [76]	-43.2	2.76	8.1
Head-Gordon [68]	-76.0	4.11	5.7
Svanberg [81]	-77.2	3.89	4.4
Yamamoto [75]	-41.8	4.28	8.8
Smith [69]	-104.0	3.00	5.6
Lahaye [70]	-103.4	2.98	8.7
Exp. [68, 79]	-80.0 [a]		5.0 [b]

[a] Estimated V_0 value.

[b] Anharmonic vibrational frequency.

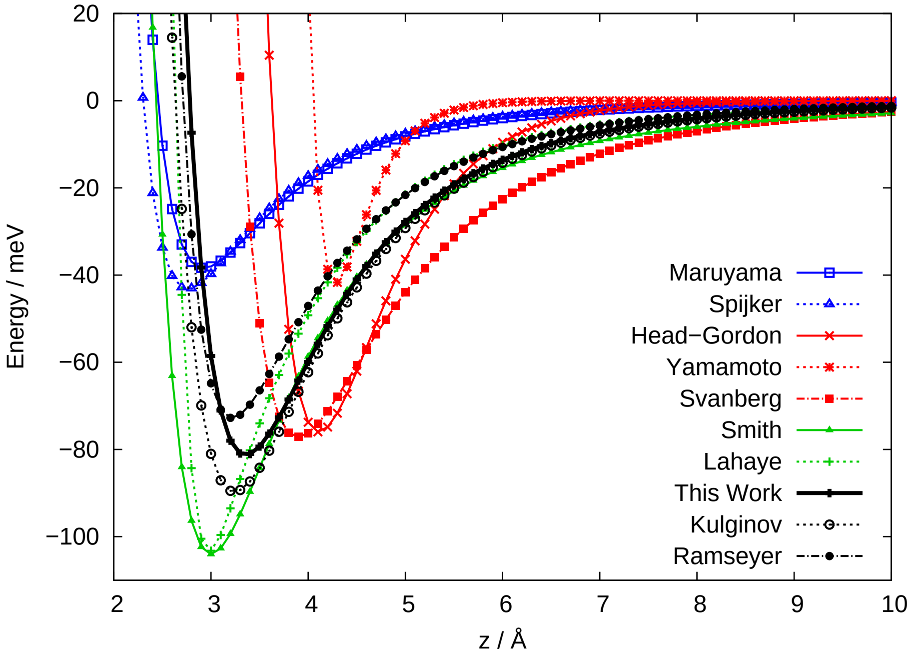

Figure 3.3: Pt(111)-Ar interaction potentials. z is the distance between the Ar atom at the vertical of the fcc-hollow site and the first layer of the Pt(111) surface. $z = 0$ is defined as the position of the Pt nuclei of this first layer for T = 0 K.

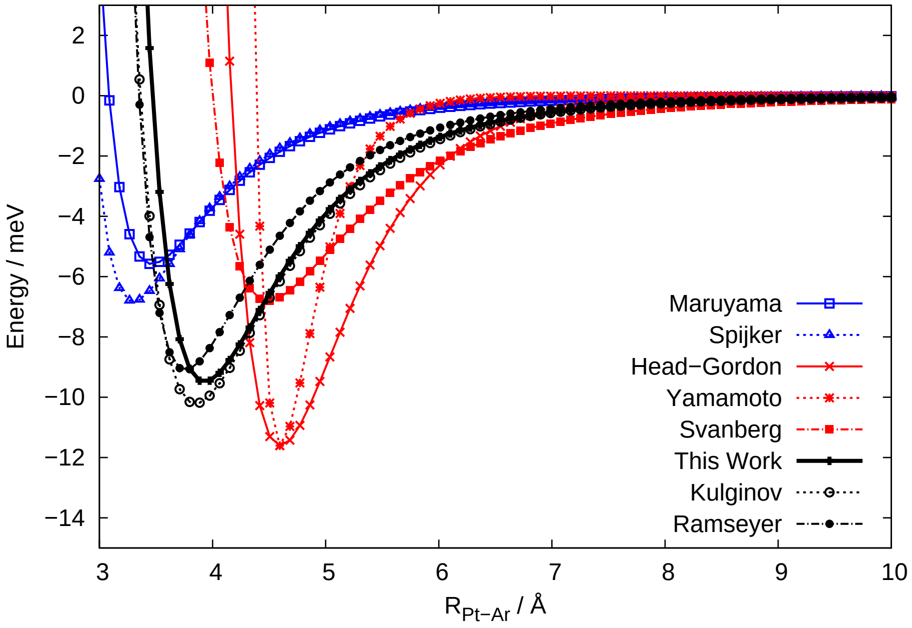

Figure 3.4: Pt-Ar pairwise potentials.

and Pettersson [81]. They reproduce correctly the experimental value of V_e, but with relatively large values of z_e compared with the other potentials. Additionally, we can mention the potential of Yamamoto [75], based on the parameters derived by Head-Gordon *et al.* [68], but with $2\sigma = 3.2$ Å^{-2} instead of $2\sigma = 1.6$ Å^{-2}. The resulting potential depicts a weak value for V_e and a relatively large equilibrium distance. The third group concerns the potentials deduced by Smith *et al.* [69] and Lahaye *et al.* [70]. Both use global van der Waals attractive part of the potential between Ar and the Pt surface. They cannot be decomposed into a pairwise sum. The corresponding V_e are lower than -100 meV and the z_e are ≈ 3 Å.

The last group includes the present potential, and those of Kulginov *et al.* [71] and Ramseyer *et al.* [82]. Our V_e value well reproduces the experimental value of approximately -80 meV and is ranged between the Kulginov and Ramseyer ones. The $z_e = 3.35$ Å deduced from our potential is also consistent with those of about 3.25 Å from the Kulginov or Ramseyer potentials. Experimentally, no information exists about the equilibrium distance between the Ar atom and the Pt surface but, such values around 3.2 and 3.4 Å should be correct since the last group of potentials reproduce properly as well the experimental equilibrium interaction energy as the experimental vertical Pt(111)-Ar harmonic vibrational frequency. The values of ω_e of this group of potentials are indeed very close to the experimental value of 5 meV.

Finally, the forces corresponding to all considered pairwise potentials are plotted in Figure 3.5. One can notice that the $|\mathbf{f}(R_{Pt-Ar})|$ functions (equation (3.12)) decay rapidly as R_{Pt-Ar} increases and can be negligible when $R_{Pt-Ar} \geq 3R_e$.

It must be noticed that, although the present and the Kulginov interaction potentials use the same mathematical expression, the repulsive part parameters are strongly different. In the Kulginov potential, the V_0 and α parameters have been determined from measured scattering data. This is not possible for R_0 which accounts for the position of the repul-

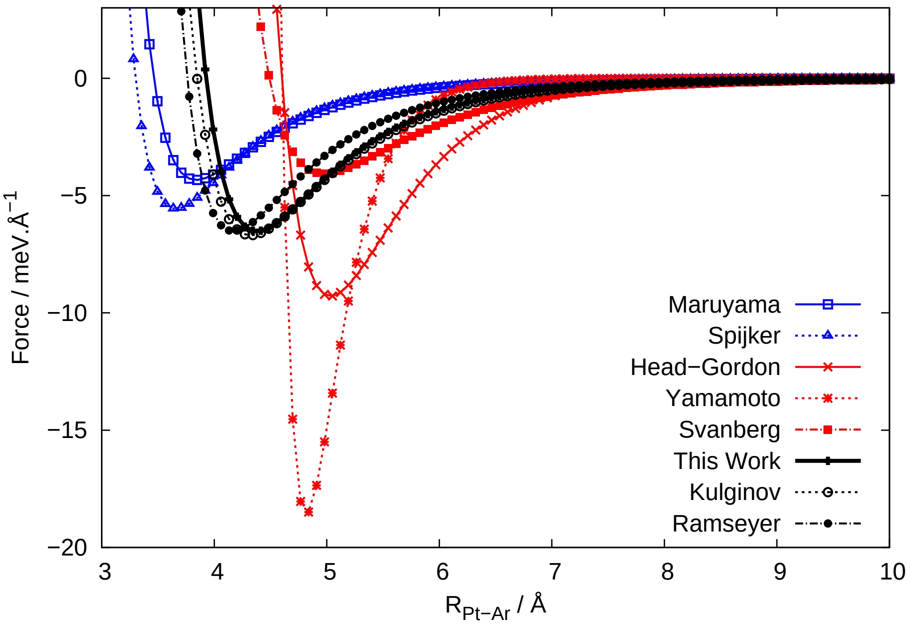

Figure 3.5: Pt-Ar pairwise forces.

Table 3.3: Comparison of the $\sigma_t^{dir}(\theta = 45°, 0°)$ given by two models for T = 300 K and an incident angle of 45°.

Potential	D_e / meV	R_e / Å	Model 1	Model 2
Present work	9.5	3.93	0.40	0.14
Yamamoto [75]	11.6	4.60	0.28	0.14

sive potential with respect to the attractive one. R_0 has been derived from local-density approximation DFT calculations. In our model, the potential can be seen as a Morse potential for which the attractive part is replaced by a van der Waals function. R_0 is seen as the minimum position of the potential where the repulsive part equilibrates the repulsive one. The differences between the present and the Kulginov parameters could come from the fact that the Kulginov parameters, V_0 and α, have been determined before R_0, whereas in our case, R_0 is almost fixed before optimizing V_0 and α. Both potentials are very similar for energies within the minimum and the dissociative region, as shown in Figures 3.3 and 3.4. However, strong divergences appear for very high energies, which are out of the scope of this study.

3.4.2 TMAC results

In order to consider the effect of the wall model, two models have been considered in a preliminary step. The first model simulates the mutual interaction between a gas atom and the wall (Model 1), whereas in the second model (Model 2), the gas atom exerts no force on the wall atoms. The former is more realistic but very expensive and for a given set of wall atoms, only one gas-wall collision is considered in one simulation. In Table 3.3, the $\sigma_t^{dir}(45°, 0°)$ values have been computed from Models 1 and 2 using our new pairwise potential and the one used by Yamamoto [75]. For both potentials, $\sigma_t^{dir}(45°, 0°) = 0.14$ if the simplified Model 2 is considered.

Table 3.4: Dissociation energy (D_e in meV), equilibrium distance (R_e in Å), and $\sigma_t^{dir}(\theta = 45°, 0°)$ computed at T_w = 300 K with an incident angle of 45° from different Pt-Ar pairwise potentials.

Potential	D_e / meV	R_e / Å	$\sigma_t^{dir}(\theta = 45°)$
Present work	9.5	3.93	0.40
Kulginov [71]	10.2	3.85	0.46
Ramseyer [82]	9.1	3.76	0.49
Maruyama [73, 74]	5.6	3.46	0.34
Spijker [76]	6.8	3.30	0.28
Head-Gordon [68]	11.6	4.60	0.24
Svanberg [81]	6.8	4.49	0.23
Yamamoto [75]	11.6	4.60	0.28

This value is comparable to the σ_t value of 0.19 found by Yamamoto [75] using a Couette flow simulation approach and a simplified wall description. In his simulation, the Pt atoms are connected through Lennard-Jones pairwise potentials with no possible relaxation. We find that Model 1 gives a much higher $\sigma_t^{dir}(45°, 0°)$ values. Model 2 corresponds indeed to a much harder surface and, the reflection tends to be more specular than with Model 1. Numerical results based on Model 1 show clearly that the wall can be locally deformed due to the collision. The gas atoms stay longer near the surface and interact deeply with it, resulting in a more diffusive reflection. This preliminary study conducted us to use Model 1 for all of the results discussed in what follows.

The values of $\sigma_t^{dir}(45°, 0°)$ computed at 300 K with an incident angle of 45° are tabulated in Table 3.4. The main characteristics of the pairwise potentials (i.e. the dissociation energies, D_e and the equilibrium positions, R_e) are also given. The $\sigma_t^{dir}(45°, 0°)$ values reported in Table 3.4 vary between 0.23 and 0.49. Such differences are closely related to the type of potential used. A first group of pairwise potentials, that includes the Maruyama and Kimura [73, 74] and Spijker *et al.* [76] potentials, present low dissociation energies D_e ($\approx 6 - 7$ meV) and short equilibrium positions ($<$ 3.5 Å). For both of these potentials, the $\sigma_t^{dir}(45°, 0°)$ is about 0.3. It should be noticed that these Lennard-Jones type potentials are commonly used in MD simulations [65] even if they do not reproduce properly the Pt(111)-Ar interaction (see Section 2.2). The second group results from interaction potentials associated with V_e close to the experimental value and large z_e, i.e. Head-Gordon and Svanberg potentials [68, 81]. These pairwise terms are characterized by relatively large values of R_e ($>$ 4.5 Å) resulting in small $\sigma_t^{dir}(45°, 0°)$ values, close to 0.25. The third group deals with the pairwise potential of the present work together with the Kulginov and Ramseyer ones [71, 82]. All these two bodies terms lead to $\sigma_t^{dir}(45°, 0°)$ values in the $0.4 - 0.5$ range. They present equilibrium geometries around $3.8 - 3.9$ Å and D_e ranging from 9.1 meV to 10.2 meV.

If $\sigma_t \approx 1$, the wall is almost diffusive whereas if $\sigma_t \approx 0$, the wall is almost specular. The wall tends to become diffusive if the Ar atoms can approach closer to the wall and interact more with it. This situation is obtain for the third class of pairwise potentials whereas the pairwise potentials of the first and second classes lead to more specular interaction of Ar with the wall. In the first class, the pairwise terms present shorter equilibrium

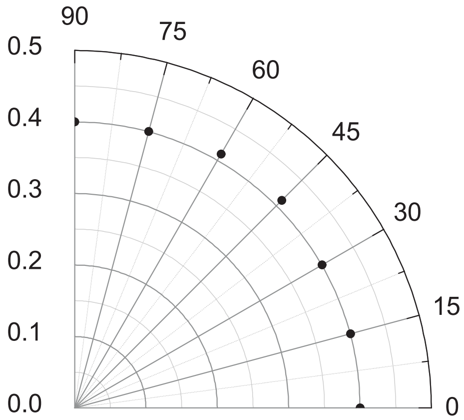

Figure 3.6: $\sigma_t^{dir}(\theta, \phi)$ values computed for $T_w = 300$ K, $\theta = 45°$ using the present potential, for ϕ varying between 0 and 90°.

Table 3.5: $\sigma_t^{dir}(\theta, 0°)$ and corresponding standard deviation σ_{TMAC} computed at $T_w = 300$ K with the Pt-Ar pairwise potential of the current work for different incident angles.

Incident angle	$\sigma_t^{dir}(\theta, 0°)$	σ_{TMAC}
10°	0.43	2.30
30°	0.41	0.85
45°	0.40	0.63
60°	0.41	0.55
80°	0.45	0.51

distances and lower D_e compared to the third class potentials. In the second class, the situation is reversed: the equilibrium distances are longer than those predicted from the third class. The force function (see Figure 3.5) resulting from our pairwise term can almost be superimposed with the curves associated with the Kulginov and Ramseyer forces. Consequently, almost identical values of σ_t are obtained. Moreover, it can be mentioned that the analytical expression of the potential has a low influence: indeed, our and Kulginov potentials have the Buckingham behavior, whereas the Ramseyer one is a Lennard-Jones potential.

$\sigma_t^{dir}(45°, \phi)$ has been evaluated for different values of ϕ and the resulting values are depicted in Figure 3.6. The orientation of the Oxz plane with respect to the surface has a negligible impact on the σ_t value and the surface (111) can be seen as isotropic.

Table 3.5 shows that the $\sigma_t^{dir}(\theta, 0°)$ variations with the incident angle are within 0.40 to 0.45 for the new potential suggested in present work. When averaging over θ, i.e. summing the different $\sigma_t^{dir}(\theta, 0°)$ values determined for the values of θ displayed in Table 3.5 and dividing by the number of the θ values, the resulting σ_t is 0.42. This averaged value could be associated to the σ_t parameter in the Maxwell's model.

Figure 3.4.2 gives the full distribution of the x component of the reflected velocity for 12000 collisions using the present pair potential for $T_w = 300$ K, $\theta = 45°$ and $\phi = 0°$. The standard deviation of the fitted curve equals 155.4 m.s^{-1} and is related to the TMAC standard deviation:

$$\sigma_{TMAC} = \frac{\sigma_{\langle v_{rx} \rangle}}{\langle v_{ix} \rangle} \ . \tag{3.14}$$

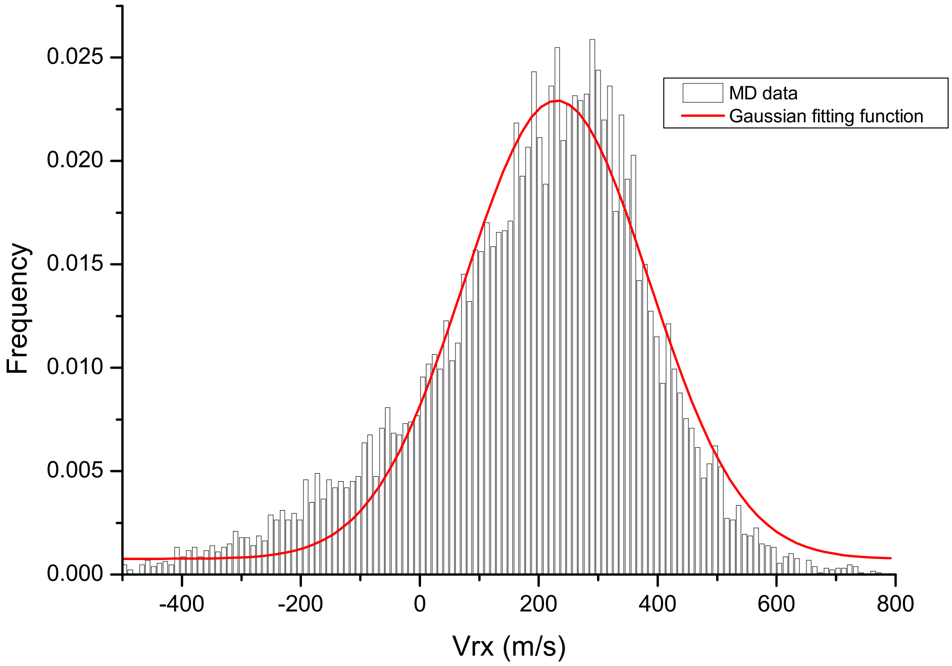

Figure 3.7: Distribution of the v_{rx} velocity with $v_{ix} = 262\,\mathrm{m.s}^{-1}$ after 12000 collisions using the present pair potential for $T_w = 300$ K, $\theta = 45^\circ$ and $\phi = 0^\circ$. The red curve corresponds to the fit of the results by a gaussian function $f(v_{rx}) = 7.6 \times 10^{-4} + \left(\frac{8.6}{310.7 \times \sqrt{\pi/2}}\right) \times \exp\left(-2 \times (\frac{v_{rx} - 230.3}{310.7})^2\right)$.

We notice that the deviations reported in Table 3.5 are very high, especially for small incident angles. These high deviations can be explained through analyzes of the post-collision path of the Ar atoms. After the collision with the wall, an Ar atom can bounce backward or forward with a large reflection angle. Therefore, the accommodation coefficient for a single Ar atom can be very high and, even negative. Theoretically, the σ_t corresponding to a single collision can take any negative or positive value according to the Maxwell model. This phenomenon is in agreement with the work of Finger *et al.* [66]. The deviation is higher with small θ since the initial tangential velocity in the denominator of equation (3.14) decreases.

Although most of the results of this work are obtained using a constant incident velocity corresponding to the gas temperature, we have done separate simulations using the Maxwell-Boltzmann distribution for the normal incident velocity:

$$f'(v_{i\tau}) = \left(\frac{m_g}{2\pi k_B T_g}\right)^{\frac{1}{2}} \times e^{-\frac{m_g v_{i\tau}^2}{2k_B T_g}} \ . \tag{3.15}$$

The resulting value of $\sigma_t^{dir}(45°, 0°)$ value is 0.39 using the present potential for $T_w = 300$ K. This result is almost identical to the σ_t^{dir} value of 0.40 in Table 3.4 obtained by the use of the constant $v_{i\tau}$ defined by equation (3.13).

We now compare some previous MD studies on the σ_t determination for the Pt-Ar couple with the present model. In their work, Sun and Li [77] have simulated Couette flows in smooth and rough nanochannels and have varied the temperature and the types of the surface crystal.

In their model, they have used Pt-Ar pairwise potential derived by Maruyama and Kimura [73, 74] and the Einstein model for the Pt slab vibration. For an isothermal flow at 200 K, they have obtained a σ_t value of 0.348 which can be compared with $\sigma_t^{dir}(45°, 0°) = 0.34$ for 300 K of Table 3.4. At 200 K, the present model would leads to $\sigma_t^{dir}(45°, 0°) = 0.47$, larger than the Sun and Li one. The low value derived by Sun and Li is probably due to their choice for the wall model since they have chosen a simple spring description based on the Einstein model leading to $k = 179.5$ N.m^{-1}, higher than the present k_{wall} value. This implies a more specular behavior of the collision.

Spijker *et al.* [76] have explored the computation of accommodation coefficients by the use of velocity correlation profiles determined from MD simulations. Contrary to the above studies, the Argon gas confined between two Pt walls was not subject to a flow but was at equilibrium. The Pt-Pt interactions in the walls were described by a Lennard-Jones potential. They have reoptimized the parameters of the Lennard-Jones Pt-Ar derived by Maruyama *et al.* [73, 74] to correctly describe the wettability character of Ar on a Pt surface, and at 300 K they derived a σ_t value of 0.53 whereas using their potential we obtained $\sigma_t^{dir}(45°) = 0.28$. The difference of the values can be due to either the wall model or the way of computing σ_t. Their model is based on velocities correlations between incoming and outcoming particles colliding with the walls to compute σ_t from in equilibrium gas atoms.

Very recently, using the Pt-Ar potential reoptimized by Spijker *et al.* [76], Prabha and Sathian [78] have simulated a Poiseuille flow in a nanochannel by MD. The Ar gas nonequilibrium flow was maintained due to a gravity field. For a wall temperature of 300 K, a Knudsen number of 0.74 and a gravity field of 5.10^{-7} nm/ps^2, they obtained a σ_t value of

0.290.This result agrees within 0.01 with the present $\sigma_t^{dir}(45°, 0°)$ value of 0.28 computed at the same temperature and using the Spijker potential. This agreement allows to validate the present MD model.

Agrawal and Prabhu compiled theoretical and experimental σ_t values in a survey. The averaged value is of 0.983 [92] for Ar atoms independently of the surface material. Experimentally, Cooper *et al.* [93] deduced a value of 0.52 ± 0.1 from the first experimental determination of the slip coefficient for Ar through tubular carbon structures, and Arkilic *et al.* [94] obtained σ_t between 0.75 and 0.85 for measurement of Ar mass flows through silicon micromachined channels due to an imposed pressure gradient. The σ_t difference between these experimental works gives an idea of the importance of the material surface. To the best of our knowledge, no experiment exists on the σ_t determination for the Pt-Ar couple making a good comparison difficult.

In order to conclude this study about the effect of the pair potential on the σ_t determination, the results of a scattering simulation are presented. Head-Gordon *et al.* also reported molecular beam experiments for the Pt(111)-Ar system. Figure 2 of Ref. [68] shows the velocity distribution of the scattered flux of Ar atoms with an incident energy of 2.5 kJ.mol^{-1} and an incident angle of 45° on a Pt(111) surface at 500 K. We have simulated this experiment using the same parameters for the atomic beam with $T_g = 600$ K, corresponding to an energy of 2.5 kJ.mol^{-1}, and the present potential. The reflected velocity has been plotted as a function of the reflected angle and the corresponding curve is compared with the experimental and simulated data of Head-Gordon *et al.* in Figure 3.8.

The simulated curve of Head-Gordon *et al.* was based on the use of the corresponding potential of Table 3.1, which has been optimized on the measured data of Figure 3.8.
The present curve presents the same main trends as the experimental points. The reflected velocity is maximum for θ_r around 20° and for θ_r larger than 40-50°, the norm of $\mathbf{v}_r$ is almost constant. However, the present calculated velocities are higher by approximately 100 m.s^{-1} in comparison with the measured data.

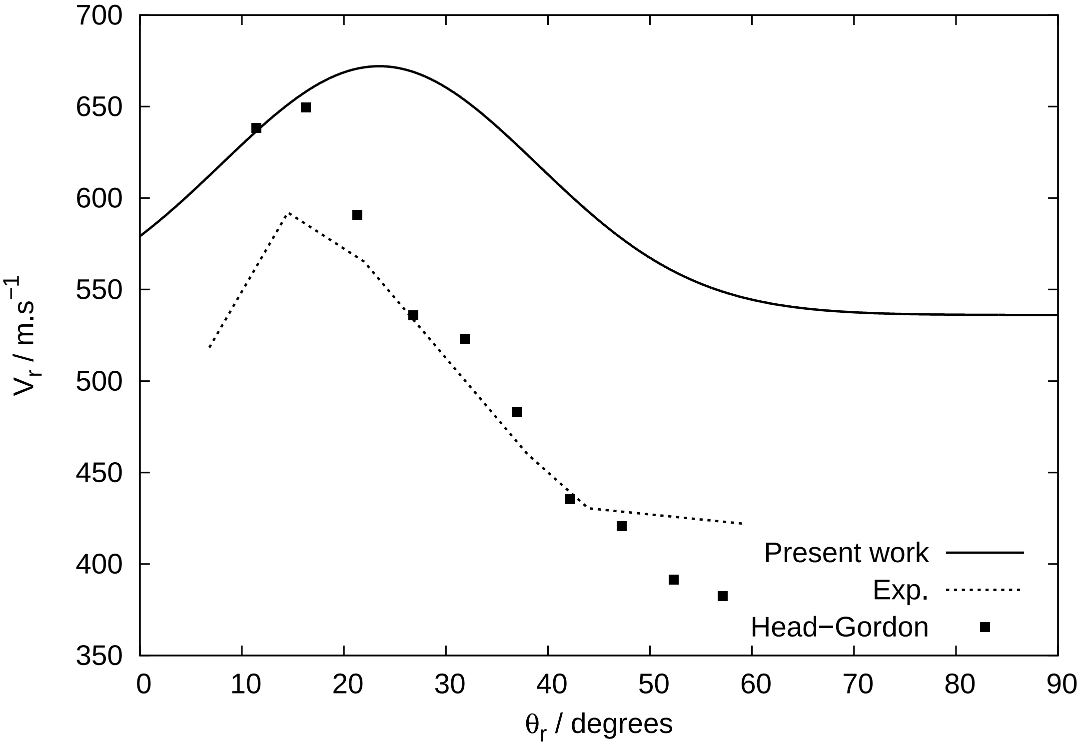

Figure 3.8: Norm of the reflected velocity (in m.s^{-1}) recorded for different values of the reflected angle θ_r (in degrees) with respect to the normal direction of the surface. The present pair potential has been used as well as $T_g = 600$ K, $T_w = 500$ K, $\theta = 45°$ and $\phi = 0°$. The dotted curve corresponds to the experimental values recorded by Head-Gordon *et al.* [68] and the markers to the simulated data from the same work.

Chapter 4

Effects of wall surface

4.1 Introduction

As mentioned earlier, based on Eq. (5.45) of Maxwell's model, the σ_t parameter for a gas-wall couple can be determined by either experiments [94] or Molecular Dynamics [51, 65] in the Navier Stokes slip regime. However, most MD simulations of flows were done at nanoscale [95] and did not have the same conditions as in experiments. In order to compare σ_t calculations with measurements for dilute gases, a more relevant MD approach [47, 60] consists in studying every single gas-wall collision event. Consequently, σ_t can be computed directly by projecting gas atoms into the surfaces and finding momentum changes [66]. This approach, which is quite similar to beam experiments [96], provides insights into the reflection mechanism and can be used to improve Maxwell's model. As far as multi-scale simulations are concerned, the obtained fluid-wall interaction results can be coupled with other numerical methods [3, 4, 8, 97–99].

In Eq. (3.1), the use of one parameter σ_t as in Maxwell's model means that the slip behavior is isotropic. For anisotropic textured surfaces, more sophisticate models are needed to reproduce the direction dependent slip or gas-wall interaction behavior. Bazant and Vinogradova [100] suggested using a slip length tensor to quantify this behavior. The tensorial nature of the slip effect was shown to be related to the interfacial diffusion [100**?** –102]. Effective slip tensors with bounds for flows over superhydrophobic surfaces were also obtained [103, 104]. As the slip models describe macroscopic behaviors, it is thus relevant to investigate the problem at the scale of fluid wall interaction. For gases, Dadzie and Meolans [105] generalized Maxwell's scattering kernel by using anisotropic accommodation coefficients. The consequences of the model on the slippage have not been studied. Since the anisotropic scattering kernel model does not provide full information about the gas-wall collisions, we shall use MD method to study these interactions in detail with the focus on the surface morphology. The MD code used in this chapter is the parallel version described in Ref. [47]. The original code has been enriched (e.g multi-body potentials, statistical tools, etc..) to adapt to the aim of the present work.

Generally, results obtained from MD simulations depend on the following factors:
- The interaction potential between the gas/wall atoms as mentioned in Chapter 3.
- The dimension of the simulation models. In general, 3D models are better than 2D since it accounts for interactions of the gas atom with all its neighbors.
- The potential between the solid atoms must be good enough to reproduce the free surface effect. It is well known that the distance between the atomic layers near the free surface are much smaller than in the bulk.

- The temperature effect must be considered as gas molecules are adsorbed easier at cold walls than at hot walls, which can results in a higher σ_t.
- The surfaces are not always ideally smooth and can have different morphology (e.g randomly rough or textured surfaces).

This chapter aims at including these features in simulations of molecular beam experiments. The gas/wall couple under consideration is Argon and Platinum but the methodology of the present work can be used to obtain σ_t for any gas/wall couple provided that an appropriate potential is used. The chapter is organized as follows. After the Introduction, Section 2 is devoted to the description of the computational method. It discusses briefly the choice of potentials, the method to prepare surface samples and MD simulation of gas/wall interaction. We remark that a part of surface sample preparation requires a separate molecular dynamics simulation of film deposition processes in order to create a realistic random roughness surface. The σ_t results issued from the calculations are then shown in Section 4. Finally, conclusions and perspectives are discussed.

4.2 Computation model

4.2.1 Interatomic potential

The interatomic potentials play an important part in the molecular dynamics simulations since they govern the dynamics of the system and, thus the accuracy of the results. In this work, the following van der Waals type pair potential between At and Pt derived by Kulginov *et al.* [71] is used

$$\phi_{Ar-Pt}(r_{Ar-Pt}) = V_0 e^{-\alpha(r_{Ar-Pt}-r_0)} - \frac{C_6}{r^6_{Ar-Pt}} , \qquad r_{Ar-Pt} = |\mathbf{r}_{Ar} - \mathbf{r}_{Pt}| , \tag{4.1}$$

where r_{Ar-Pt} is the distance between an Ar atom at location $\mathbf{r}_{Ar}$ and a Pt atom at location $\mathbf{r}_{Pt}$, or *vice versa.* As mentioned in Chapter 1, contrary to usual Lennard-Jones potentials, the repulsive part of this pair potential has a Born-Mayer form and provides a better description of the strong repulsion of the electrons. The pairwise potential parameters have been empirically adjusted such that the laterally average potential reproduces the measured properties of an Ar atom adsorbed on a slab of Pt atoms, i.e. a well depth of about 80 meV [68] and, a vibrational frequency of the adsorbed atom of about 5 meV [79]. The van der Waals interaction of an Ar atom with a platinum surface can be evaluated from the Ar-polarizability and the Pt-dielectric function. The values of the potential parameters are given in Table 4.1 and were shown to be in good agreement with an *ab-initio* based calculation [106].

Table 4.1: Parameters of the Pt-Ar pairwise potential [71].

V_0 (eV)	α (Å^{-1})	R_0 (Å)	C_6 (eV.Å^6)
20000	3.3	-0.75	68.15

In terms of the potential between the Pt atoms, the multi-body Quantum-Sutton Chen (QSC) potential is used [107]. As a particular Finnis-Sinclair potential type, the QSC potential includes quantum corrections and predict better temperature dependent properties.

Table 4.2: Quantum Sutton-Chen parameters for Pt [108].

n	m	ϵ (eV)	c	a (Å)
11	7	9.7894e-3	71.336	3.9163

For a system of N Pt-atoms, the potential is given by the following expression

$$V_{pot,Pt} = \epsilon \left[\frac{1}{2} \sum_{i=1}^{N} \sum_{\substack{j=1 \\ j \neq i}}^{N} \left(\frac{a}{R_{ij}} \right)^{n} - c \sum_{i=1}^{N} \rho_i^{1/2} \right] , \qquad \rho_i = \sum_{\substack{j=1 \\ j \neq i}}^{N} \left(\frac{a}{R_{ij}} \right)^{m} , \tag{4.2}$$

where a is the lattice constant, R_{ij} the distance between atom i and j and the local density ρ_i of atom i. The parameters ϵ and a determine the scales of energy and length, respectively and, n and m the range and shape of the potential. These potential parameters are given in Table 4.2. Combining the Ar-Pt and Pt potentials, we can compute the total potential of the system

$$V_{pot} = \sum_{i=1}^{N} \phi_{Ar-Pt}(R_{Ar-i}) + V_{pot,Pt} , \tag{4.3}$$

and the force $\mathbf{f}_i$ acting on atom i at position $\mathbf{r}_i$ by

$$\mathbf{f}_i = -\frac{\partial V_{pot}}{\partial \mathbf{r}_i} . \tag{4.4}$$

Since we only consider the interaction of one Ar atom with a Pt surface, there is no contribution of the Ar-Ar term in the total potential formula V_{pot}. The accuracy of the QSC potential for Pt has been justified in Ref. [108] as it reproduces accurately the melting temperature and the specific heat of the material. Although its implementation is more costly than the harmonic (spring) potential, it should better reproduce the surface effects, since atoms near the free surfaces are different from the bulk. Our tests on the QSC potential show that in fully relaxed equilibrium system, the interatomic distance near the free surfaces is much smaller than in the bulk (see Fig. 4.1). As shown by previous works [109–111], the lattice constant, wall mass and stiffness can have significant impacts on σ_t and the slip effects.

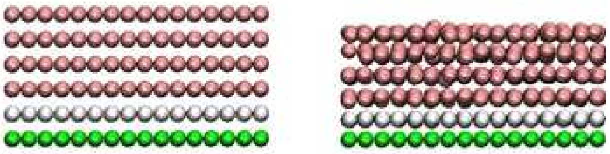

Figure 4.1: Surface effects: the fully relaxed configuration (right) is different from initial configuration (left).The solid film system is composed of fixed atoms (bottom layer), thermostat atom (upper bottom layer) and normal atoms (remaining layers).

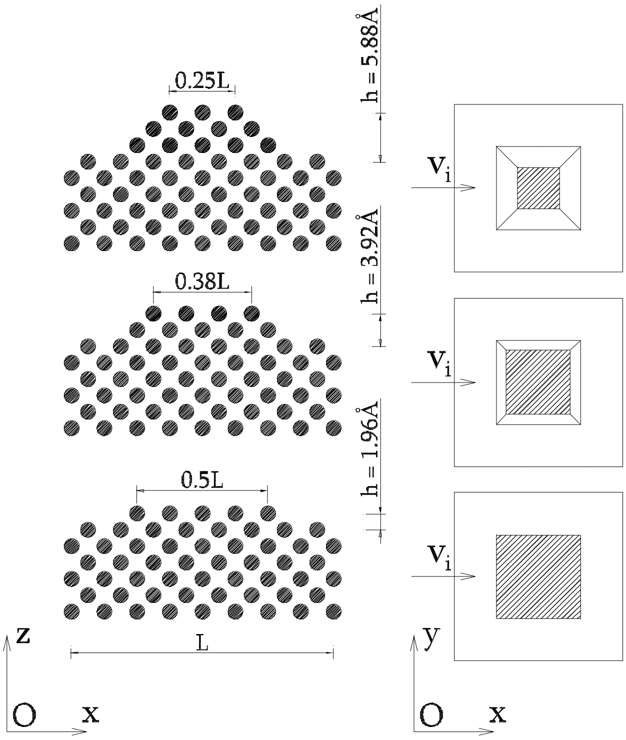

Figure 4.2: Nanotextured surface of type A (square)

4.2.2 Surface samples

In this work, three types of surfaces are considered: smooth surfaces, periodic nanotextured surfaces and randomly rough surfaces. The orientation of their free surfaces is (100) according to the Miller index. Initially, the Pt atoms are arranged in layers and the two lowest ones (phantom atoms) are used to fix the system and for the thermostat purpose. The remaining Pt atoms are free to interact with other solid atoms and gas atoms. The random arrangement of these atoms defines the "rough" state of the surface and will be detailed later on.

A smooth surface model is a system composed of 768 atoms arranged in 6 layers, all of which are in perfect crystal order. The nanotextured models are constructed from the smooth surface model by adding successively atom layers to create pyramids with the slope angle 45°. The slope is necessary to assure the stability of the system since perfectly vertical blocks (slope angle 90°) are less stable: in many cases atoms migrate to lower positions and the blocks evolve into step-like structures with smaller potential energy. The base of the pyramid can be a square (type A, Fig. 2) or an infinite strip (type B, Fig. 3), so that both isotropic/anisotropic effect can be considered. Although these pyramids are simplified models of a real rough surface, it can show the dependence of σ_t on the roughness. The latter in MEMS/NEMS is reported to be several Å [12]. In this work, the highest peak, varying with the number of atoms layers added on the surfaces, ranges from 2 to 6 Å.

Randomly rough surface models are also constructed by adding atoms on the smooth surfaces in a random way. In the available literature, there are several mathematical mod-

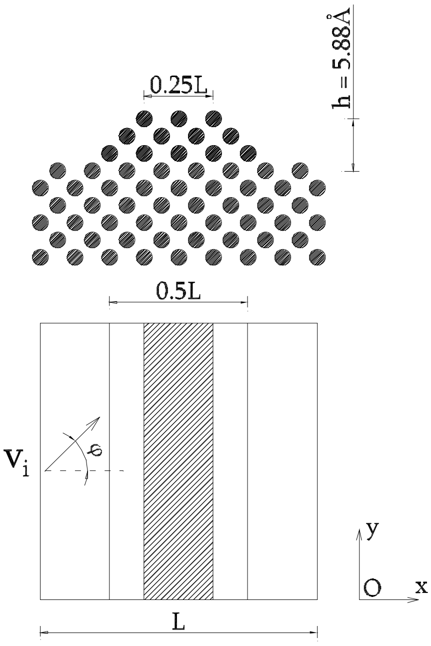

Figure 4.3: Nanotextured surface of type B (strip)

els [112–115] that describe random roughness. However, these models are not suitable at atomic scale: it is difficult to force atoms to be at given positions and, structure parameters such as orientation (100) and lattice constant must be respected. Furthermore such atomistic systems might not be appropriate in terms of potential energy. In our opinion, a randomly rough surface which is consistent with the internal atomistic structure, should be built from molecular dynamics simulations. Rapid cooling of thin films from the liquid state [116] can create rough surfaces but the final systems could contain many defects (e.g. pores, dislocations) and non crystalline structure (e.g. polycrystal, amorphous). As the present work focuses on Pt (100), the rough surfaces are constructed by deposing atoms randomly on the existing smooth Platinum surface. Since this procedure is quite similar to the film vapor-deposition processes, it is asssumed that the created surface is quite close to real MEMS/NEMS surfaces. The procedure of the material deposition is described as follows.

The initial system is a Pt plate made of four layers of 512 solid atoms, arranged in (100) fcc order. First, the system is relaxed towards the minimal potential energy configuration. Then, after 2000 time steps of 1 fs, a Pt atom is inserted randomly from a height of 10 Å with the initial thermal velocity corresponding to 1000 K. Under the attraction force (QSC potential) from the Pt plate, the deposed Pt atoms move downwards until they reach the plate which is maintained at 50 K. (see a snapshot of the deposition process in Fig. 4.4). Finally, when all inserted Pt atoms are attached firmly into the Pt plate, the whole system undergoes the anneal process at the ambient temperature $T_a = 300$ K with a time step equal to 2 fs. During the whole simulation, the Leap-Frog Verlet integration scheme is employed and the temperature is kept constant by simple velocity scaling method. Figure 4.4 shows a snapshot of the final system whose total number of Pt atoms have reached 733. To improve the statistical results, 5 samples obtained thanks to the above described procedure are collected, as shown in Fig. 4.5.

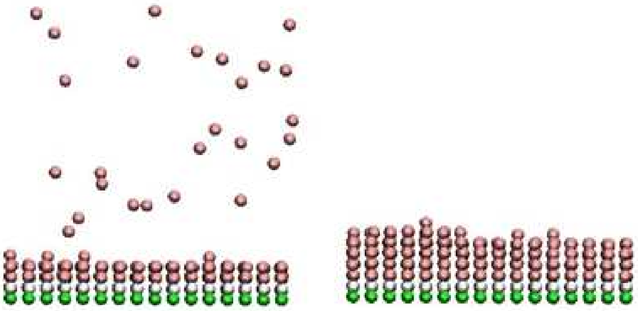

Figure 4.4: Snapshot of deposition process (left) and final thin film system (right)

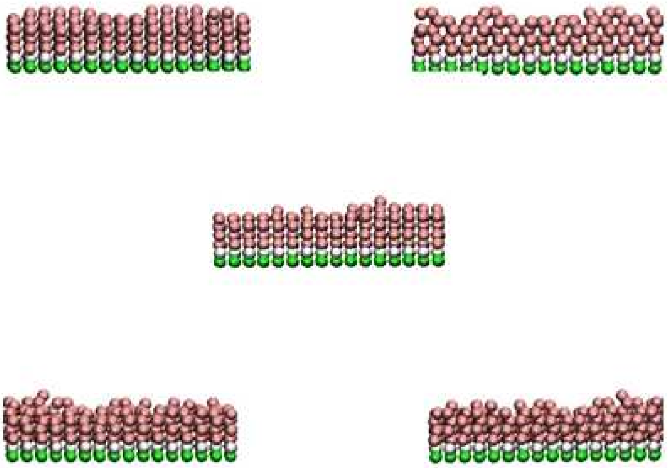

Figure 4.5: Five samples obtained from the deposition process

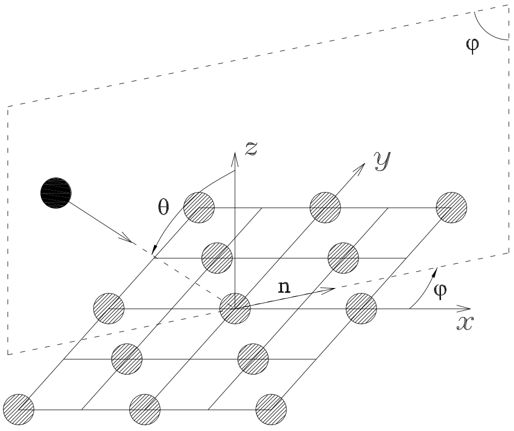

Figure 4.6: Representation of θ, φ in cartesian coordinate system

4.2.3 Dynamics of gas/wall collision

In what follows, we describe the MD method used to simulate the gas-wall collision and to calculate the σ_t coefficient. The simulations are three dimensional: an Ar atom is projected into a Pt(100) surface with different incident angles θ and with different approaching φ-planes. In spherical coordinate system, (θ, φ) are the polar and azimuthal angles, respectively (see Fig 4.6). As mentioned in Chapter 2, the coefficient $\sigma_t^{dir}(\theta, \varphi)$ is given by

$$\sigma_t^{dir}(\theta, \varphi) = \frac{\langle v_{in} \rangle - \langle v_{rn} \rangle}{\langle v_{in} \rangle} , \tag{4.5}$$

where v_{in} and v_{rn} are the projections of the incident and the reflected velocity on the vector $\mathbf{n}$, respectively. The latter is the intersection of the plane xOy and the φ-plane, i.e it lies on xOy and makes an angle φ with respect to Ox. Only one gas-wall collision is treated per simulation and the averages $\langle v_{in} \rangle, \langle v_{rn} \rangle$ in Eq. (4.5) are taken over a large number of simulations (or collisions). The definition (4.5) is the most accurate description of gas-wall interaction since it is associated to each direction. We also calculate the *effective anisotropic* $\sigma_t^{an}(\varphi)$ coefficients using the same equation (4.5) but with gas atoms arriving from all directions: the direction of $\mathbf{v}_i$ is randomly uniform with $v_{in} > 0$. In the special case where the surface is isotropic, σ_t^{an} varies little with φ and a single *effective isotropic* σ_t^{iso} constant is sufficient for modelling gas-wall interaction as in Maxwell's model. The latter *effective isotropic* coefficient is obtained by the similar method but $\langle v_{in} \rangle, \langle v_{rn} \rangle$ in Eq. (4.5) are further averaged over $\mathbf{n}$ (or φ).

We assume first that an Ar atom only interacts with the Pt wall within a cutoff distance $r_c = 10$ Å. Since this distance is much smaller than the typical mean free path at atmospheric pressure or in high vacuum ($\lambda > 69$ nm), it can justify the choice of such a small region to calculate the σ_t coefficients. At a distance of 10 Å, an Ar atom can be considered as non-interacting with the Pt- wall atoms since the potential value at that distance (-0.0580736meV) is negligibly small when compared with the potential well depth (10.21 meV). At the beginning of each simulation, an Ar atom is inserted randomly at the height r_c above the wall surface with initial incident velocity $\mathbf{v}_i$. The norm of $\mathbf{v}_i$ is equal to the thermal speed corresponding to the gas beam temperature T_g. Although the results of this work are obtained using a constant incident velocity corresponding to the gas temperature, we have done separate simulations using the Maxwell-Boltzmann velocity distribution and

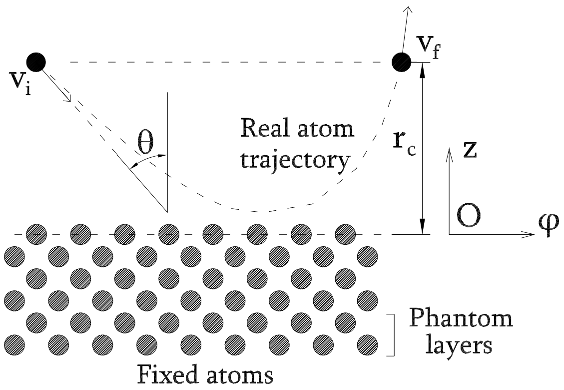

Figure 4.7: Molecular dynamics scheme. The incident argon atoms are with v_i velocities. θ is the incident angle. The Pt wall has a fcc structure with a (100) surface. The Pt atoms are controlled by Sutton-Chen potential.

find that σ_t is insensitive to this modification. A collision is considered as finished when the atom bounces back beyond the cutoff distance. Then the reflected velocity $\mathbf{v}_r$ is recorded for the statistical purpose and another Ar atom is reinserted randomly to continue the process. After approximatively 10000 collisions (simulations), converged values of σ_t values were obtained. Numerical tests show that the statistical error of a typical 10000-collision average is within 1.0%.

Throughout the simulations, periodic boundary conditions were applied along the x, y directions. The velocities and positions of gas atoms and the solid atoms at each time step are calculated by the usual Leap-Frog Verlet integration scheme. To control the temperature T_w of the system, the phantom technique is used: the Langevin thermostat [91] is applied to the atom layer above the fixed layers. The motion of an atom i belonging to this layer is governed by the equation

$$m_i \frac{d\mathbf{v}_i(t)}{dt} = -\xi \mathbf{v}_i(t) + \mathbf{f}_i(t) + \mathbf{R}_i(t) \ . \tag{4.6}$$

In Eq. (4.6), $\mathbf{v}_i$ is the velocity of the atom i, $\mathbf{f}_i$ is the resulting force acting on it by the surrounding ones, m_i is the atomic mass and ξ is the damping coefficient. The third term $\mathbf{R}_i$ in the right hand side of Eq. (4.6) is the random force applied on the atom. In the simulation, it is sampled after every time step δt from a Gaussian distribution with zero average and mean deviation of $\sqrt{6\xi k_B T_w/\delta t}$. The simulations were carried out by setting time step and damping factor at the following values:

$$\delta t = 2 \text{ fs} \ , \quad \xi = 5.184 \times 10^{-12} \text{kg/s} \ . \tag{4.7}$$

The wall temperature T_w was kept at 200 K, 300 K and 400 K and the gas beam temperature T_g was kept at a slightly higher value than T_w, here $T_g = 1.1 T_w$. Such choice of T_g was made arbitrarily and the procedure of the present work can be applied to any gas temperature. Generally, to obtain the best statistical results, a typical run requires 4×10^7 time steps of 2 fs. All simulations were run on 9 processors, using a domain decomposition and the Message Passing Interface. The longest simulation takes about 20 CPU hours. We have carried out computations with different time steps from 1fs to 3fs and we have found that the results are insensitive to this factor.

Table 4.3: $\sigma_t^{dir}(\theta,\varphi)$ computed at $T_w = 200\ K$, $300\ K$, $400\ K$ for three roughness heights h with $\theta = 10°$, $45°$, $80°$ and $\varphi = 0°$.

Surface type	θ	$T_w = 200\ K$	$T_w = 300\ K$	$T_w = 400\ K$
A (h =5.88 Å)	10°	0.96	0.87	0.79
	45°	0.92	0.85	0.77
	80°	0.90	0.83	0.74
A (h =3.92 Å)	10°	0.94	0.84	0.75
	45°	0.90	0.79	0.74
	80°	0.88	0.78	0.72
Smooth	10°	0.85	0.72	0.61
	45°	0.82	0.70	0.60
	80°	0.80	0.69	0.59

Table 4.4: σ_t^{iso} and $\sigma_t^{dir}(\theta,\varphi)$ computed at $T_w = 300\ K$.

Surface type	φ	θ	σ_t^{dir}	σ_t^{iso}
A (h =5.88 Å)	0°	10°	0.87	–
	0°	30°	0.86	–
	0°	45°	0.85	–
	0°	60°	0.85	–
	0°	80°	0.83	–
	–	–	–	0.85
Random (Fig. 4.5)	–	–	–	0.92
Smooth	–	–	–	0.70

4.3 MD simulation results

4.3.1 Effects of temperature and roughness height

From the description of the models in Section 2, the coefficient σ_t^{dir} can depend on the several input parameters: temperature, surface morphology, incident direction (θ, φ). The variation of σ_t^{dir} in terms of these parameters is investigated in the following subsections.

The σ_t^{dir} results at different temperatures are shown in Tables 4.3 and Fig. 4.8. A general trend can be noticed here: σ_t^{dir} increases as the temperature decreases, ranging from 0.78 to 0.92 in the case of the highest roughness considered (h = 5.88 Å). This trend in σ_t^{dir} variation can be explained by the fact that the adsorption is stronger with colder walls. Gas atoms stay longer near the wall, interact more with solid atoms and, as a result, the reflection is more diffusive. Similar remarks have been reported in Refs. [65, 76] for confined systems. For h = 5.88 Å and $T_w = 300\ K$, Table 4.4 shows that the σ_t^{dir} value varies very little with the incident angle θ and very close to the average isotropic value $\sigma_t^{iso} = 0.85$. This means that for this kind of surface, Maxwell's one parameter model is sufficiently accurate to model gas-wall interaction.

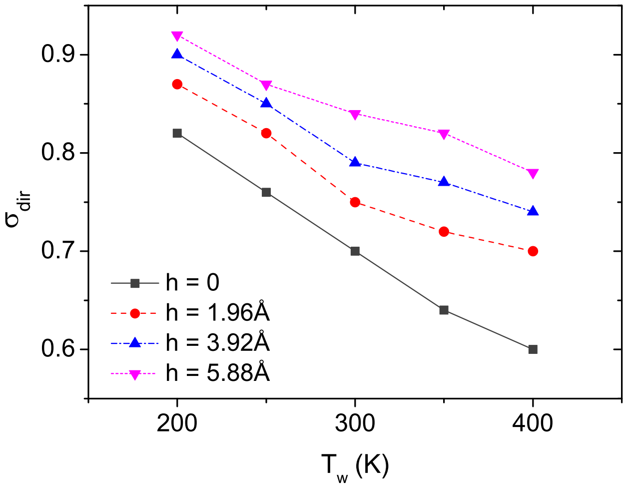

Figure 4.8: σ_t^{dir} computed for the wall of type A (square) at $T_w = 200\ K$, $250\ K$, $300\ K$, $350\ K$ and $400\ K$ for three roughness heights h with $\theta = 45°$ and $\varphi = 0°$.

The σ_t^{dir} coefficient increases with the roughness of the wall surface (see Table 4.3 and Fig. 4.8). Computations carried out for pyramidal structures at the temperature of 300 K show that the σ_t^{dir} coefficient can reach up to 0.87 for surfaces with the highest peak configuration. It is clear that the presence of peaks leads to non uniform surface potentials with local minima where gas molecules can easily be trapped: the gas atoms adhere stronger to the wall and lose their initial momentum. Moreover, the changes in local slopes produce more or less random variations in the local incident and reflection angles.

Visualization of collision trajectories shows a clear difference between a smooth surface and a rough surface. On a smooth surface, a gas molecule collides and bounces several times before finally escaping from the influence distance r_c of the wall (see Fig.4.9). On a rough surface, it stays near the wall and moves within the valley between the peaks, a mechanism similar to surface diffusion, until the wall provides enough energy to escape (see Fig.4.10). The real behaviors are mixed: we sometimes observe the colliding and bouncing mechanisms on rough surfaces (not shown in Fig.4.10), but they are not typical.

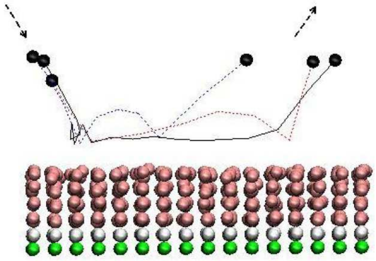

Figure 4.9: Typical collision trajectories (solid and dashed lines) on a smooth surface. Gas molecules collide and bounce several times before escaping.

Next we considered the case of random surfaces obtained from the atom deposition process. With the same parameters for the deposition process, the σ_t^{dir} obtained for the five

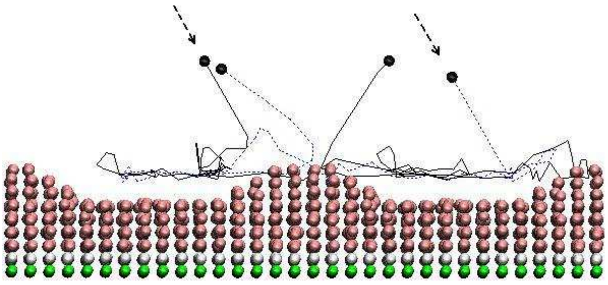

Figure 4.10: Typical collision trajectories (solid and dashed lines) on a rough surface. Gas molecules move within the valley between the peaks.

samples shown in Fig. 4.5 exhibit small differences, from 0.90 to 0.93. It is very close to σ_t^{iso} value for random surfaces 0.92 (see Table 4.4). Thus, in addition to the roughness height, the in-plane random arrangement of the atoms also plays a significant role on the accommodation coefficient.

4.3.2 Surface anisotropy effect

An anisotropic textured surface can obstruct or facilitate the flows differently along different directions. Bazant and Vinogradova [100] generalized Navier slip boundary conditions for anisotropic texture surface by using a tensorial slip length. In the framework of the kinetic theory, Dadzie and Meolans [105] proposed a new scattering kernel that accounts for surface anisotropy. Their formulation is based on three independent accommodation coefficients $\alpha_x, \alpha_y, \alpha_z$ along the three directions x, y, z. The coefficients α_x, α_y represent the tangential accommodation coefficients and α_z is the normal accommodation coefficient. The tangential accommodation coefficient α_n in direction n is then computed by the expression (see Appendix I)

$$\sigma_t^{an}(\varphi) = \alpha_n = \alpha_x \cos^2 \varphi + \alpha_y \sin^2 \varphi \ . \tag{4.8}$$

We remark that by substituting $\varphi = 0°$ and $\varphi = 90°$, the accommodation values α_x and α_y along x, y direction can be recovered. In this subsection, we study the anisotropy effect using MD and the directional σ_t definition in Eq. (4.5) and examine the relation (4.8). The anisotropy effect can be seen from Figs. 4.11 and 4.12: the σ_t^{dir} variation with φ is non uniform for rough surfaces. The accommodation process along the two directions x, y is highly different. The σ_t^{dir} is minimum when the atoms are projected along the longitudinal direction of the strip ($\varphi = 90°$), since the surface may be considered as almost smooth in that direction (see Fig. 4.3). This σ_t value corresponds to α_y in the model of [105]. The maximal σ_t values recorded for $\varphi = 0°$ and $h > 0$ can be attributed to the largest roughness effect in that direction and correspond to α_x in the model [105]. Moreover, Figs. 4.11 and 4.12 show an increase of anisotropy effect as the roughness increases: the difference between the highest and the smallest σ_t value increases with the roughness height whereas the σ_t results depend very little on the beaming direction for a smooth surface. This could be explained by the fact that the smooth surface can be considered isotropic. Although Figs. 4.11 and 4.12 show discrepancies of σ_t obtained in different ways, all curves can fit reasonably well the analytical relation (4.8) as plotted in solid, dashed and dash-dotted lines.

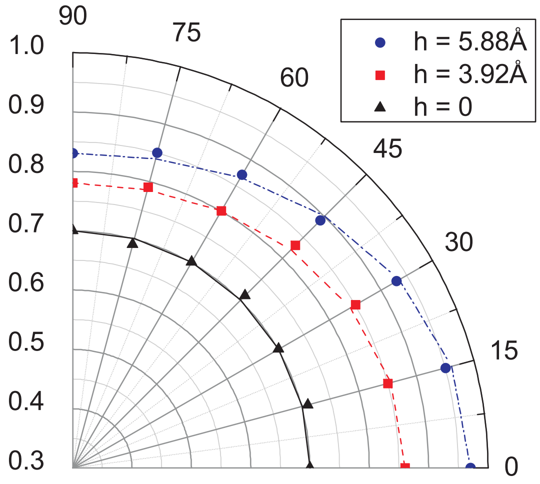

Figure 4.11: σ_t^{dir} computed for type-B walls (strip) versus azimuth angle φ for different roughnesses ($T_w = 300K$, $\theta = 45°$). The solid, dashed, dash-dotted lines are the analytical expressions (4.8) used to fit the present numerical results.

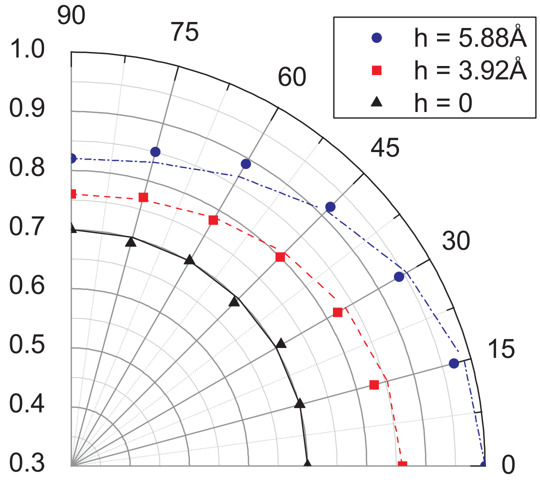

Figure 4.12: σ_t^{an} computed for type-B walls (strip) versus azimuth angle for different roughnesses ($T_w = 300K$). The solid, dashed, dash-dotted lines are the analytical expressions (4.8) used to fit the present numerical results.

Table 4.5: Ratio $\langle v_{rm}\rangle/\langle v_{rn}\rangle$ computed for type-B walls (strip) with different roughness heights h at $T_w = 300K$, $\theta = 45°$ and $\varphi = 45°$.

h	$\langle v_{rm}\rangle/\langle v_{rn}\rangle$
0	0
1.96 Å	0.15
3.92 Å	0.39
5.88 Å	0.67

For anisotropic surfaces, the reflected flux is not always lying in the same plane with the arriving one. Consequently, in addition to Eq. (4.5), we should account for the ratio of the reflected flux components along two orthogonal directions m, n: $\langle v_{rm}\rangle/\langle v_{rn}\rangle$. According to the anisotropic model (see Appendix I), this ratio can be computed by the expression

$$\langle v_{rm}\rangle/\langle v_{rn}\rangle = \frac{(\alpha_x - \alpha_y)\cos\varphi\sin\varphi}{1 - \alpha_x\cos^2\varphi - \alpha_y\sin^2\varphi} \ . \tag{4.9}$$

By observing the surface structure, we can deduce that $\langle v_{rm}\rangle/\langle v_{rn}\rangle$ must vanish for impinging fluxes parallel to the planes of symmetry of the anisotropic surface. That remark is in good agreement with Eq. (4.9) where $\langle v_{rm}\rangle/\langle v_{rn}\rangle = 0$ at $\varphi = 0°, 90°$. Our MD simulation confirms the remark and also shows that the ratio is nonzero at $\varphi \neq 0$. From Table 4.5, at $\varphi = 45°$, we find that the ratio is significant. It even increases with the roughness height increases, i.e the anisotropic effect is enhanced.

Chapter 5

Tensorial slip theory for gas flows

5.1 Introduction

Among the topics of micro-nanofluidics, slip flows at solid surfaces have been studied actively from different aspects including experiments, modelling and computational methods [3, 8, 12, 47, 60, 101, 102]. In most problems under consideration, Navier slip boundary conditions are used

$$u_s = L_s \frac{\partial u}{\partial n} \ , \quad \text{or} \quad u_s = M\tau \ . \tag{5.1}$$

In $(5.1)_1$, u_s is the slip velocity which is assumed to be proportional to the normal velocity gradient $\frac{\partial u}{\partial n}$ at the wall and to a slip length L_s. Equation $(5.1)_2$ is another formulation based on shear stress τ and surface mobility constant M. Considering a Newtonian fluid of viscosity η, these two formulations are equivalent as $L_s = M\eta$ and $\tau = \eta\frac{\partial u}{\partial n}$. For gases, the slip length L_s is shown to be related to σ_t and the mean free path λ according to Maxwell's model [12, 16]

$$L_s = \frac{2-\sigma_t}{\sigma_t}\lambda \ . \tag{5.2}$$

Micro-nano textured surfaces have drawn a lot of scientific interests recently. If suitably designed, these surfaces can become superhydrophobic and reduce significantly friction. However, due to the strong surface anisotropy, the application of isotropic equation (5.1) is quite limited. A natural generalization of (5.1) while keeping the relations linear is the following tensorial form [100]

$$\mathbf{u}_s = \mathbf{b}\frac{\partial \mathbf{u}}{\partial n} \ , \quad \text{or} \quad \mathbf{u}_s = \mathbf{M}\boldsymbol{\tau} \ . \tag{5.3}$$

In (5.3), $\mathbf{u}_s, \mathbf{u}, \boldsymbol{\tau}$ are vectors and $\mathbf{M}, \mathbf{b}$ are second rank tensors having the same meanings as u_s, u, τ, M, L_s. Specifically, the tensors $\mathbf{M}$ and $\mathbf{b}$ can capture the anisotropy effect when they are not proportional to the identity tensor $\mathbf{I}$. In the gas regime, it is revealed that the accommodation coefficient can be orientation dependent [117] and its variation with respect to the incident direction agrees reasonably well with the anisotropic gas-wall interaction model [105]. The latter is formulated using a scattering kernel based on three accommodation parameters. This information suggests that the tensors $\mathbf{M}$ and $\mathbf{b}$ can be obtained from the accommodation coefficients in the same manner as Maxwell's isotropic model.

The present chapter which aims at addressing the aforementioned problem, is organized as follows. After the introduction, we shall revisit the concept of anisotropic scattering kernel proposed in Ref [105] and the associated slip models in Section 5.2. Explicit expressions for **M** and **b** as functions of the accommodation parameters are presented. Section 5.3 is dedicated to Molecular Dynamics (MD) simulation of Poiseuille flows where the anisotropic gas-wall interaction model is implemented. The MD results will then be compared with the available analytical solutions. Finally, some concluding remarks are given at the end of the chapter.

5.2 Anisotropic slip theory for gas flows

5.2.1 Scattering kernel for anisotropic surfaces

In kinetic theory, the boundary conditions for the distribution function $f(\mathbf{v})$ are usually described using a scattering kernel, for example

$$v_z f(\mathbf{v}) = \int_{\Omega'} B(\mathbf{v}', \mathbf{v}) |v'_z| f(\mathbf{v}') d\mathbf{v}' \ . \tag{5.4}$$

The scattering kernel $B(\mathbf{v}', \mathbf{v})$ is the probability that a gas atom impinging the wall with velocity $\mathbf{v}'$ is reflected with velocity $\mathbf{v}$. In Eq. (5.4), the wall is assumed to be normal to the z direction of the Cartesian coordinate system $Oxyz$. The velocity components of the incoming and outgoing atoms and the velocity spaces Ω, Ω' are defined as follows

$$\begin{aligned} \mathbf{v} &= (v_x, v_y, v_z) \in \Omega = \{\mathbb{R} \times \mathbb{R} \times \mathbb{R}^+\} \ , \\ \mathbf{v}' &= (v'_x, v'_y, v'_z) \in \Omega' = \{\mathbb{R} \times \mathbb{R} \times \mathbb{R}^-\} \ . \end{aligned} \tag{5.5}$$

Different phenomenological models for gas-wall interaction were proposed based on accommodation parameters. The first popular scattering kernel was derived from Maxwell's postulate on the reflection mechanism of the gas atoms [16]: it can be either diffusive or specular with the respective portion of σ_t and $1 - \sigma_t$. Another wellknown model was developed by Cercignani and Lampis [118, 119] and later extended by Lord [120] using two parameters α and α_{Ez}. The former is the accommodation coefficient of the tangential momentum and the latter is the accommodation coefficient of the kinetic energy due to the normal velocity component v_z. Being invariant with respect to any change of basis in the plane xOy, these two models are suitable for describing the behavior of ideally or nearly isotropic surfaces, e.g smooth crystalline surfaces. For periodic nano-textured surfaces (see Fig. 5.1), MD simulations of beam scattering experiments in Chapter 4 showed that the coefficient σ_t depends on the surface orientation. Interestingly, the variation of σ_t with respect to the incident azimuthal angle φ agrees quite well with results issued from the anisotropic scattering kernel proposed by Dadzie and Meolans [105].

Let us call Φ_i^- and Φ_i^+ the incoming and outcoming flux at the wall of the momentum i component defined mathematically by the expression

$$\begin{aligned} \Phi_i^- &= m_g \int_{\Omega'} |v'_z| v'_i f^-(\mathbf{v}') d\mathbf{v}' \ , \\ \Phi_i^+ &= m_g \int_{\Omega} |v_z| v_i f^+(\mathbf{v}) d\mathbf{v} \ , \end{aligned} \tag{5.6}$$

where f^- and f^+ are respectively the velocity distribution associated with the incident molecules and reflected molecules. Dadzie and Meolans [105] proved the following relation

$$\frac{\Phi_i^- - \Phi_i^+}{\Phi_i^-} = \alpha_i \ , \quad i = x, y \ , \quad \frac{\Phi_z^- - \Phi_z^+}{\Phi_z^- - \Phi_z^e} = \alpha_z \ . \tag{5.7}$$

In (5.7), the three model parameters $\alpha_x, \alpha_y, \alpha_z$ are the momentum accommodation coefficients along x, y, z axes and Φ_z^e is the reflected flux associated to complete accommodation situation: $\alpha_x = \alpha_y = \alpha_z = 1$.

Since (Φ_x^+, Φ_y^+) and (Φ_x^-, Φ_y^-) are components of tangential momentum vector fluxes $\mathbf{\Phi}_t^+$ and $\mathbf{\Phi}_t^-$ expressed in the same basis, the first linear relation in (5.7) can be written in tensorial form

$$\mathbf{\Phi}_t^+ = (\mathbf{I} - \mathbf{A})\mathbf{\Phi}_t^-, \tag{5.8}$$

where $\mathbf{A}$ is the accommodation tensor admitting the diagonal form in the current basis

$$\mathbf{A} = \begin{bmatrix} \alpha_x & 0 \\ 0 & \alpha_y \end{bmatrix}. \tag{5.9}$$

Finally, we note the following relation which results from (5.8)

$$(\mathbf{\Phi}_t^+ + \mathbf{\Phi}_t^-) = \mathbf{N}(\mathbf{\Phi}_t^- - \mathbf{\Phi}_t^+) \ , \quad \mathbf{N} = 2\mathbf{A}^{-1} - \mathbf{I} \ . \tag{5.10}$$

In the current basis Oxy, tensor $\mathbf{N}$ is reduced to the matrix

$$\mathbf{N} = \begin{bmatrix} (2-\alpha_x)/\alpha_x & 0 \\ 0 & (2-\alpha_y)/\alpha_y \end{bmatrix}. \tag{5.11}$$

By applying the rotation transformation $\mathbf{Q}(\varphi)$

$$\mathbf{Q}(\varphi) = \begin{bmatrix} \cos\varphi & \sin\varphi \\ -\sin\varphi & \cos\varphi \end{bmatrix}, \tag{5.12}$$

to (5.8,5.9), we find the relations between the tangential fluxes $\Phi_n^\pm, \Phi_m^\pm$ in the new basis (n, m) (see Appendix I)

5.2.2 Simplified anisotropic slip model for gas flows based on tangential accommodation coefficients

From now, we consider gas flows over a periodic nano-textured surface (see Fig. 5.1) and assume that it is possible to replace the latter with a nominally flat surface and an equivalent gas-wall interaction model. It is noteworthy to say that given the boundary conditions for the distribution f, there is no unique derivation of boundary conditions for macroscopic quantities [3, 12, 16, 121]. Temperature jump and velocity slip equations are usually based on near-wall approximation of f and the assumption that the Navier-Stokes-Fourier (NSF) equations are valid up to the wall. In many cases, the obtained boundary conditions are strongly coupled (i.e stress, heat flux, temperature, velocity, etc.. are all present in the same non linear equation) and difficult to use in practice. In what follows, we adopt the isothermal flow hypothesis and present a simplified slip model for anisotropic surfaces. The derivation of the model relies essentially on the momentum equation and its associated properties (5.7-5.11) while relaxing the other conditions of the anisotropic kernel (A.1 - A.3, Appendix I). The advantage is that it can describe reasonably well the surface anisotropy effect for a broader class of problems and avoid unphysical issues due to the kernels. The shear stress vector $\boldsymbol{\tau}$ that the wall exerts on the gas atoms can be computed directly from the difference of tangential momentum fluxes due to collisions

$$\boldsymbol{\tau} = (\mathbf{\Phi}_t^- - \mathbf{\Phi}_t^+) \ , \tag{5.13}$$

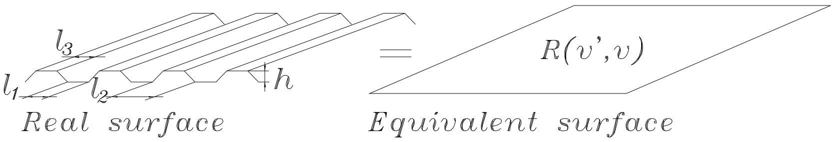

Figure 5.1: Equivalent gas-wall interaction model. In modelling and simulations, the structured surface is replaced by a smooth surface with a scattering kernel $R(\mathbf{v}', \mathbf{v})$. In Ref. [117], the authors considered a (100) crystalline Pt textured surface at 300 K with the following dimensions $l_1 = 11.76$Å, $l_2 = 19.6$Å, $l_3 = 7.84$Å, $h = 5.88$Å and used MD method to determine the accommodation parameters with Ar atoms associated to model (A.1 - A.3, Appendix I) $\alpha_x = 0.96$, $\alpha_y = 0.83$.

Assuming that the fluid near the wall is not too far from equilibrium, we can make the following approximation

$$\int_{\Omega'} f^-(\mathbf{v}')d\mathbf{v}' \simeq \int_{\Omega} f^+(\mathbf{v})d\mathbf{v} = \rho/2 \ , \tag{5.14}$$

where ρ is the total number density of the wall density function $\bar{f}$. The latter is defined from f^- and f^+ as follows

$$\bar{f} = f^- \text{ in } \Omega' \ , \quad \bar{f} = f^+ \text{ in } \Omega \ . \tag{5.15}$$

Next, we consider that, to some extent, the normal velocity component v_z in f^+ is independent of the tangential velocity $\mathbf{v}_t = (v_x, v_y)$ and v'_z in f^- is independent of $\mathbf{v}'_t = (v'_x, v'_y)$. Accounting for (5.14), the tangential momentum vector fluxes (5.6) can be estimated by

$$\begin{aligned} \mathbf{\Phi}_t^- \simeq m_g \bar{c}_z \int_{\Omega'} \mathbf{v}'_t f^-(\mathbf{v}')d\mathbf{v}' \ , \quad \mathbf{\Phi}_t^+ \simeq m \bar{c}_z \int_{\Omega'} \mathbf{v}_t f^+(\mathbf{v})d\mathbf{v} \ , \\ \frac{\rho}{2}\bar{c}_z = \int_{\Omega'} |v'_z| f^-(\mathbf{v}')d\mathbf{v}' = \int_{\Omega'} |v_z| f^+(\mathbf{v})d\mathbf{v} \ . \end{aligned} \tag{5.16}$$

The last equality of (5.16) implies that the wall does not accumulate. Using the definition of gas velocity at the wall

$$\rho \mathbf{u}_s = \int_{\Omega} f^+ \mathbf{v}_t d\mathbf{v} + \int_{\Omega'} f^- \mathbf{v}'_t d\mathbf{v}' \ , \tag{5.17}$$

we can deduce that

$$\mathbf{\Phi}_t^- + \mathbf{\Phi}_t^+ = m_g \rho \bar{c}_z \mathbf{u}_s \ . \tag{5.18}$$

Combining (5.10) and (5.18,5.13) leads to the following expression of the slip velocity

$$\mathbf{u}_s = \mathbf{M}\boldsymbol{\tau}, \quad \mathbf{M} = \frac{1}{\rho m_g \bar{c}_z}\mathbf{N} \ . \tag{5.19}$$

It is interesting to note that the second rank tensor $\mathbf{M}$, is similar to the interfacial mobility tensor in the tensorial slip theory [100]. In the case of Newtonian fluid of viscosity η, we obtain the generalized slip equation for anisotropic surface using the concept of slip length tensor $\mathbf{b}$

$$\mathbf{b} = \eta \mathbf{M} \ . \tag{5.20}$$

We note that the viscosity η is related to the mean thermal speed $\bar{c}$ and the mean free path λ [4]

$$\eta = \frac{1}{2}\rho m_g \bar{c}\lambda \ , \quad \bar{c} = \sqrt{\frac{8kT}{\pi m_g}} \ , \tag{5.21}$$

while $\bar{c}_z$ can be estimated from (5.16) by considering $\bar{f}$ (hence f^+, f^-) close to Maxwellian

$$\bar{c}_z = \sqrt{\frac{2kT}{\pi m_g}} \ . \tag{5.22}$$

As a result of (5.20), (5.19) and (5.11), tensor $\mathbf{b}$ becomes simplified into the simple form

$$\mathbf{b} = \lambda \mathbf{N} = \lambda \begin{bmatrix} (2-\alpha_x)/\alpha_x & 0 \\ 0 & (2-\alpha_y)/\alpha_y \end{bmatrix} . \tag{5.23}$$

It is interesting to remark that (5.23) is consistent with a rather heuristic and less rigorous approach presented in Appendix II. These results are the generalization of earlier works [12, 51] concerning isotropic surfaces. Another interesting feature of $\mathbf{b}$ is that it is independent of temperature [1] and the choice of the kernel form (A.1 - A.3, Appendix I). Finally, it is reduced to Maxwell's slip model when the behavior is isotropic, i.e $\alpha_x = \alpha_y$.

Tensor $\mathbf{b}$ can be made dimensionless with a characteristic length, for example the channel height H,

$$\bar{\mathbf{b}} = \frac{\mathbf{b}}{H} \ . \tag{5.24}$$

and using the Knudsen number Kn,

$$\frac{\bar{\mathbf{b}}}{\mathrm{Kn}} = \mathbf{N} \ , \quad \text{with} \quad \mathrm{Kn} = \frac{\lambda}{H} \ . \tag{5.25}$$

In Ref [121], a slip model associated directly to the kernel form (A.1 - A.3, Appendix I) was proposed. The obtained expression is still rather complex and still depend on the temperature T even if the variations along the tangential directions x, y are neglected. The gas temperature T must also be solved from the NSF equations combined with the separate temperature jump model. As shown by previous works [63, 64, 95], the gas temperature profile exhibits some anomalies that can not be described by available analytical solutions and even by compressible NSF equations. Furthermore, when the surface is isotropic $\alpha_x = \alpha_y$, Maxwell's model can not be recovered from the model proposed in Ref. [121].

We must also say that the slip models are based on the validity of NSF equations at the wall which is not true. However, as shown in previous works and our MD results in the later section, these models can describe reasonably well the slip effects near the wall. Furthermore, errors can be dealt with using empirical coefficients or higher order models, etc...

5.2.3 Poiseuille flow analytical solutions

We consider confined gas flows between two immobile parallel textured walls. The (dimensionless) slip tensors of each wall are denoted respectively $\bar{\mathbf{b}}^+$ (upper wall) and $\bar{\mathbf{b}}^-$ (lower

---

[1] The temperature dependence of the slip model can be expressed via the temperature dependence of α_x, α_y

wall). The flows can be driven by either pressure difference or external force field. As shown in previous works [49, 51, 95, 122] relevant to isotropic surfaces, Poiseuille parabolic solution can describe well the velocity profile even in nano-size channel and at high Knudsen number. These results suggest that we can adopt the following equation for the case under consideration [100]

$$\mathbf{u} = \frac{H^2}{4\eta}\left\{\frac{1}{2}\left[1-\left(\frac{2z}{H}\right)^2\right]\mathbf{I}+\mathbf{J}+\left(\frac{2z}{H}\right)\mathbf{K}\right\}\mathbf{g}\ . \tag{5.26}$$

with $\mathbf{g}$ being the driving force, equivalent to the pressure gradient or the external body force. For MD simulation cases studied in the later section, the fluid is subject to a gravity like field $\boldsymbol{\gamma}$ and the driving force $\mathbf{g}$ can be evaluated as average mass density $m_g\rho_0$ times $\boldsymbol{\gamma}$

$$\mathbf{g} = m_g\rho_0\boldsymbol{\gamma} \tag{5.27}$$

Tensors $\mathbf{J}, \mathbf{K}$ are defined by

$$\begin{aligned} &\mathbf{J} = \mathbf{C} - \mathbf{D}(\mathbf{I}+\mathbf{C})^{-1}\mathbf{D}\ , \quad \mathbf{K} = (\mathbf{I}+\mathbf{C})^{-1}\mathbf{D}\ ,\\ &\mathbf{C} = \bar{\mathbf{b}}^{+} + \bar{\mathbf{b}}^{-}\ , \quad \mathbf{D} = \bar{\mathbf{b}}^{+} - \bar{\mathbf{b}}^{-}\ . \end{aligned} \tag{5.28}$$

The first term of (5.26) is the usual no-slip Poiseuille profile, the second constant term corresponds to slip-driven plug flow and the third term corresponds to a linear shear stress flow [100].

The general formulation (5.26,5.28) does not require that the two wall surfaces are aligned and their slip tensors $\bar{\mathbf{b}}^{+}$ and $\bar{\mathbf{b}}^{-}$ are not necessarily diagonal in the current basis.

In the case where the slip tensors $\bar{\mathbf{b}}^{+}, \bar{\mathbf{b}}^{-}$ are diagonal in the basis Oxy, $\mathbf{J}, \mathbf{K}$ are also diagonal in the same base and their components admit the expressions

$$\begin{aligned} J_x &= \frac{\bar{b}_x^{+} + \bar{b}_x^{-} + 4\bar{b}_x^{+}\bar{b}_x^{-}}{1+\bar{b}_x^{+}+\bar{b}_x^{-}}\ , \quad J_y = \frac{\bar{b}_y^{+} + \bar{b}_y^{-} + 4\bar{b}_y^{+}\bar{b}_y^{-}}{1+\bar{b}_y^{+}+\bar{b}_y^{-}}\ ,\\ K_x &= \frac{\bar{b}_x^{+} - \bar{b}_x^{-}}{1+\bar{b}_x^{+}+\bar{b}_x^{-}}\ , \quad K_y = \frac{\bar{b}_y^{+} - \bar{b}_y^{-}}{1+\bar{b}_y^{+}+\bar{b}_y^{-}}\ . \end{aligned} \tag{5.29}$$

If the relation (5.23) holds, we can rewrite the previous expression as follows

$$\begin{aligned} J_x &= \frac{\mathrm{Kn}(N_x^{+}+N_x^{-}) + 4\mathrm{Kn}^2 N_x^{+}N_x^{-}}{1+\mathrm{Kn}(N_x^{+}+N_x^{-})}\ ,\\ J_y &= \frac{\mathrm{Kn}(N_y^{+}+N_y^{-}) + 4\mathrm{Kn}^2 N_y^{+}N_y^{-}}{1+\mathrm{Kn}(N_y^{+}+N_y^{-})}\ .\\ K_x &= \frac{\mathrm{Kn}(N_x^{+}-N_x^{-})}{1+\mathrm{Kn}(N_x^{+}+N_x^{-})}\ ,\\ K_y &= \frac{\mathrm{Kn}(N_y^{+}-N_y^{-})}{1+\mathrm{Kn}(N_y^{+}+N_y^{-})}\ . \end{aligned} \tag{5.30}$$

These analytical expressions will be examined in the later section with the Molecular Dynamics method.

5.3 Molecular dynamics models

In this section, we described the Molecular Dynamics method to simulate gas flows in a nanochannel. The gas atoms are placed in a rectangular box of dimension $L \times B \times H$ along x, y, z directions and subject to a uniform force field $\boldsymbol{\gamma}$ parallel to the plane xOy. We assume that the interaction between the gas atoms and the walls (normal to the z direction) can be described by the anisotropic kernel (A.1 - A.3, Appendix I). The following parameters associated to the kernel are used

$$\alpha_x = 0.96\ , \quad \alpha_y = 0.83\ , \quad \alpha_z = 0.9\ , \quad T_w = 300K\ . \tag{5.31}$$

It is noted that the values of α_x, α_y correspond to the tangential accommodations coefficients for Ar and a nanotextured Pt wall at $T_w = 300K$ with dimensions described in Fig. 5.1 and in Ref. [117]. In Ref. [117], these values are obtained from MD simulations of beam scattering experiment.

Although (A.1 - A.3) are the constraint equations for the phase density f at the wall, we shall implement an analogous boundary conditions for MD methods that can mimic the effects of the former. From the composition of the scattering kernel B, we can say that μ_i is the percentage of the molecules whose reflection mechanism is governed by the elementary kernel B_i. During MD simulations, when a gas atom crosses the wall boundary, we consider that it collides with the wall. Then, the same molecule is reinserted at the wall boundary with the same x, y coordinates and its velocity is reassigned on the basis of different elementary processes. At each collision event, a random number X with uniform distribution between $[0, 1]$ is generated. Depending on the value of X and the arriving velocity $\mathbf{v}'$, we shall decide the reflection mechanism B_i and generate the post collision velocity $\mathbf{v}$ accordingly, for example:
- If $0 < X < \mu_0$ then the reflection is specular (kernel B_0): $v_x = v'_x$, $v_y = v'_y$, $v_z = -v'_z$.
- If $\mu_0 < X < \mu_0 + \mu_{xy}$ then the reflection is specular along z, diffusive along x, y direction (kernel B_{xy}): $v_x, v_y \sim \mathcal{N}(0, \sqrt{kT_w/m_g})$, $v_z = -v'_z$.
- If $\mu_0 + \mu_{xy} < X < \mu_0 + \mu_{xy} + \mu_{xz}$ then the reflection is specular along y, diffusive along x, z direction (kernel B_{xz}) $v_x \sim \mathcal{N}(0, \sqrt{kT_w/m_g})$, $v_z \sim \mathcal{R}(\sqrt{kT_w/m_g})$ and $v_y = v'_y$.
- etc...

considering that the total sum of μ_i equals 1 (see A.2, Appendix I).

Here $\mathcal{N}(0, \sqrt{kT_w/m_g})$ is the normal distribution with zero mean and standard deviation $\sqrt{kT_w/m_g}$ and $\mathcal{R}(\sqrt{kT_w/m_g})$ is the Rayleigh distribution with parameter $\sqrt{kT_w/m_g}$. In addition to the previously described wall boundary conditions along the z direction, the simulation box is periodic along the x, y directions.

It is clear that the described anisotropic collision mechanism is a generalization of Maxwell's original mechanism. Here the specular and diffusion reflections are applied to three velocity components for different proportions of atom μ_i in order to reproduce the momentum relative changes (5.7). Furthermore, due to a considerable molecular portion reflecting diffusively at the wall temperature T_w, these boundary conditions correspond to a thermal wall allowing energy exchange. As the results, thermostats are no longer needed during MD simulation. A rather similar thermal wall approach can be found in Ref [49].

In our simulations, the interaction force between two gas molecules at distance r is governed by the Lennard-Jones potential :

$$V(r) = 4\epsilon\left[\left(\frac{\sigma}{r}\right)^{12} - \left(\frac{\sigma}{r}\right)^{6}\right], \tag{5.32}$$

with cutoff distance $r_c = 2.5\sigma$. For Argon, the reference energy ϵ and length σ are respectively $\epsilon = 1.67 \times 10^{-21}$ J and $\sigma = 0.341$ nm. The global number density is kept constant, $\rho_0 = 0.035\sigma^{-3}$ while the number of the molecules N, the acceleration γ and others geometric parameters like L, B, H are changed as shown in Table 5.1.

Table 5.1: Input data of MD simulations

N(atoms)	$L(\sigma)$	$B(\sigma)$	$H(\sigma)$	Kn	$\gamma(\epsilon/m\sigma)$
74088	128.4	128.4	128.4	0.05	0.001
27000	91.7	91.7	91.7	0.07	0.001
8000	61.1	61.1	61.1	0.104	0.001
4400	61.1	61.1	33.6	0.19	0.001

During the simulations, the Leapfrog-Verlet integration algorithm is employed and the averaging procedure starts only when the flow is stabilized, i.e. after about 10^6 time steps of 2 fs. The total computational time is 2×10^8 time steps. The height of the channel is divided into 100 layers to determine accurately the distribution of local stream velocity $\mathbf{u}$. The flow direction determined by the angle φ made between the flow direction n (also the direction of $\boldsymbol{\gamma}$) and the x axis is also varied from 0° to 90° to examine the anisotropy effect of the channel. The global mean free path λ used in the analysis is calculated by the formula

$$\lambda = \frac{1}{\sqrt{2}\pi\rho_0\sigma^2} \ . \tag{5.33}$$

5.4 Results

5.4.1 Walls with identical slip tensors

We consider first the case where the two walls are identical and aligned, $\overline{\mathbf{b}}^{+} = \overline{\mathbf{b}}^{-} = \overline{\mathbf{b}}$. This simplification leads to the following expression of $\mathbf{J}$ and $\mathbf{K}$,

$$\mathbf{J} = 2\overline{\mathbf{b}} \ , \quad \mathbf{K} = \mathbf{0} \ . \tag{5.34}$$

The MD simulation results confirm the parabolic velocity profile along the flow direction for most part of the channel, as predicted by (5.26). Another interesting aspect that agrees with (5.26) and some previous studies [123, 124] is that we observe the small transversal velocity profile. The latter seems to vanish at principal directions $\varphi = 0°, 90°$ and maximal at $\varphi = 45°$ (see Fig. 5.3). We will show that these properties cannot be recovered by the isotropic slip theory.

Next let us look further into the quantitative aspect of the results. The velocity profiles along the flow direction and the transversal direction are fitted respectively with parabolic and constant equation to determine the *fitted* slip velocities at the walls. These numerically computed values will be compared with analytical solution issued from (5.26) while accounting for (5.23,5.25,5.30). We remark that some deviations from the analytical

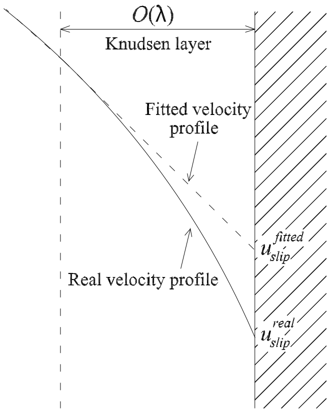

Figure 5.2: Schematic of the Knudsen layer and *real* and *fitted* slip velocities.

solution is observed in a small region near the wall (the Knudsen layer) and the *real* slip velocities can be different from the *fitted* velocities (see Fig. 5.2). The former are computed directly by averaging molecular velocity before and after collision with the walls, also considered in this work. However, for the sake of convenience, the terminology "slip velocities" without prefix (*fitted* or *real*) is used to refer to the *fitted* velocities when no comparison is made between these two quantities.

According to (5.26), the dependence of dimensionless slip lengths on the flow orientation can be expressed by the relation

$$\frac{L_s(\varphi)}{H} = \bar{b}_x \cos^2\varphi + \bar{b}_y \sin^2\varphi \tag{5.35}$$

or

$$\frac{L_s(\varphi)}{H} = \mathrm{Kn}\left(\frac{2-\alpha_x}{\alpha_x}\cos^2\varphi + \frac{2-\alpha_y}{\alpha_y}\sin^2\varphi\right) \tag{5.36}$$

if the simplified quantitative relation (5.25) is used. From Fig. 5.4, both analytical solutions and numerical solutions at different Kn show the same trend of L_s in function of φ. All MD data can be fitted perfectly with (5.35) showing excellent agreement with tensorial slip theory. On the other hand, expression (5.36) based on the quantitative estimation of $\bar{b}_x, \bar{b}_y$ shows good agreement with MD results in slip flow regime $\mathrm{Kn} < 0.1$ with average errors less than 5%. At higher Kn, considerable discrepancy is observed. The former have been reported in numerous works concerning the original Maxwell slip model and different correction coefficients (either empirically or theoretically based) have been proposed to deal with these issues [12, 19, 49].

Regarding the ratio between the slip velocities in transverse and longitudinal directions u_{sm}/u_{sn}, its dependency on the flow direction is given by (5.26):

$$\frac{u_{sm}}{u_{sn}} = \frac{(\bar{b}_y - \bar{b}_x)\sin\varphi\cos\varphi}{\bar{b}_x\cos^2\varphi + \bar{b}_y\sin^2\varphi} \tag{5.37}$$

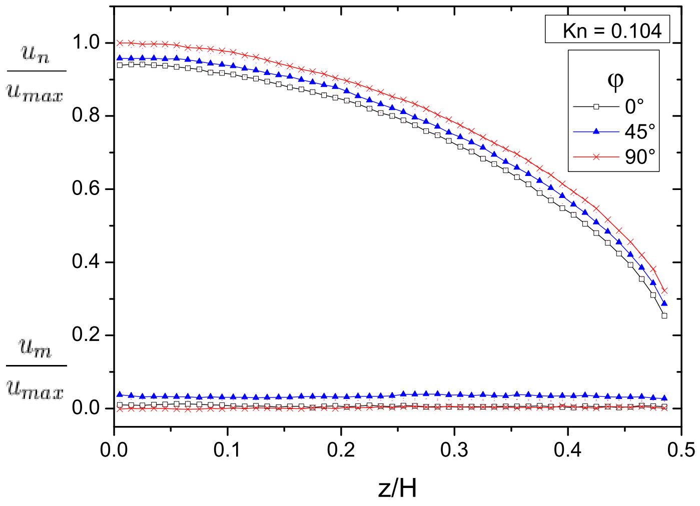

Figure 5.3: Longitudinal and transverse velocity profiles u_n, u_m for different values of φ and Kn $= 0.104$. The velocities are normalized with u_{max} - the velocity at $z = 0$ for case $\varphi = 90°$.

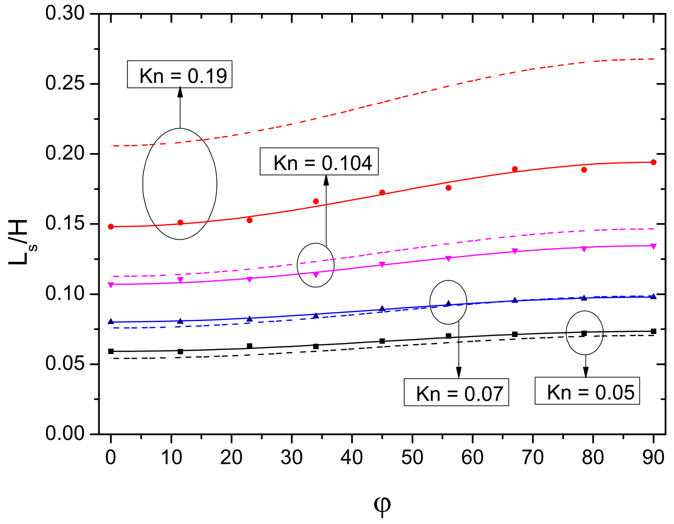

Figure 5.4: Dimensionless slip length L_s/H as a function of φ at different Kn. Points are MD data which are fitted with solid lines corresponding to the analytical expression (5.35). The dashed lines represents quantitative estimation (5.36) based on α_x, α_y.

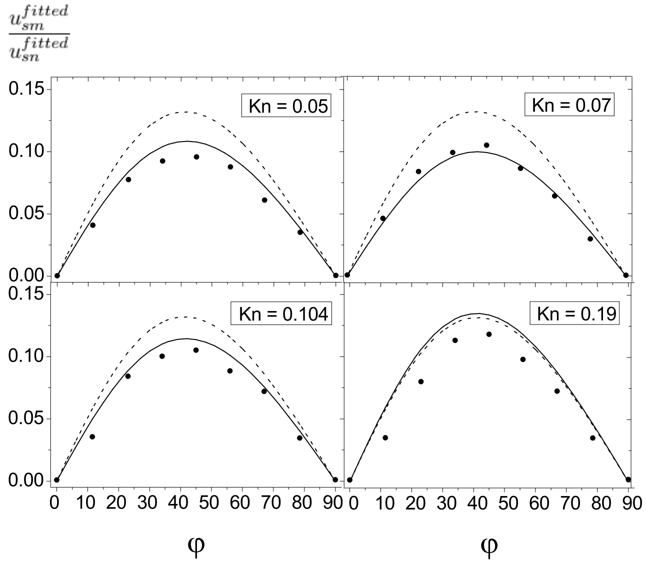

Figure 5.5: Ratio of transverse and longitudinal components of fitted slip velocity as a function of φ for various Kn. Points are MD data, the solid and dashed lines are analytical expressions (5.37) and (5.38)

using $\bar{b}_x, \bar{b}_y$ parameters from the fit of L_s by equation (5.35), or

$$\frac{u_{sm}}{u_{sn}} = \frac{\left(\frac{2-\alpha_y}{\alpha_y} - \frac{2-\alpha_x}{\alpha_x}\right)\sin\varphi\cos\varphi}{\frac{2-\alpha_x}{\alpha_x}\cos^2\varphi + \frac{2-\alpha_y}{\alpha_y}\sin^2\varphi} \tag{5.38}$$

using the approximation (5.25). It is clear that this ratio always vanishes by assuming isotropy. For anisotropic surfaces, it is a function of φ and only vanishes when $\varphi = 0°, 90°$.

Fig. (5.5) shows *fitted* slip velocities obtained from MD simulations in comparison with analytical predictions (5.37) and (5.38). Again, MD results agree very well with the analytical expression (5.37) and less well with the quantitative expression (5.38). More precisely, (5.38) overestimate the *fitted* transverse flow velocity. However, when we look into the *real* slip velocities in Fig. (5.6), there is a very good agreement and more interestingly, the ratio is quasi independent of Kn as predicted by (5.38).

According to previous works [125, 126], the ratio of averaged transverse and longitudinal flow rates is given by

$$\frac{\langle Q\rangle_m}{\langle Q\rangle_n} = \frac{6(\bar{b}_y - \bar{b}_x)\sin\varphi\cos\varphi}{1 + 6(\bar{b}_x\cos^2\varphi + \bar{b}_y\sin^2\varphi)} , \tag{5.39}$$

where $\langle Q\rangle_m$ and $\langle Q\rangle_n$ are the averaged flow rate components along the directions m and n. This ratio can be obtained by integrating the velocity profile across the channel :

$$\langle Q\rangle_m = \int_{\frac{-H}{2}}^{\frac{H}{2}} \langle u_m(z)\rangle dz , \quad \langle Q\rangle_n = \int_{\frac{-H}{2}}^{\frac{H}{2}} \langle u_n(z)\rangle dz . \tag{5.40}$$

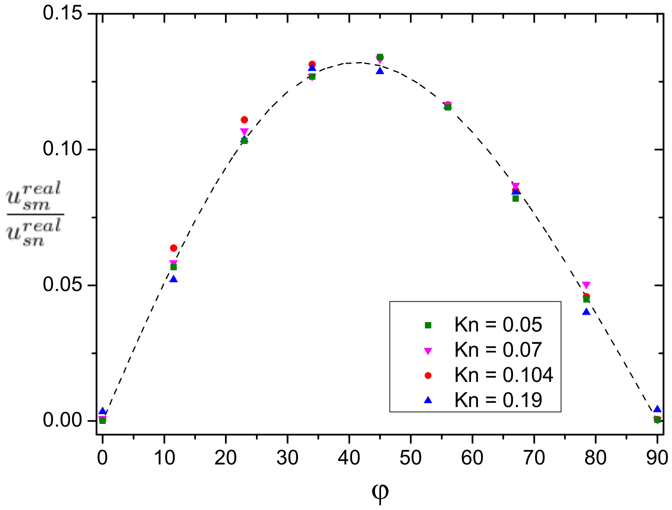

Figure 5.6: Ratio of transverse and longitudinal components of real slip velocity as a function of φ for different Kn. Points are MD data and the dashed line is for the analytical expression (5.38).

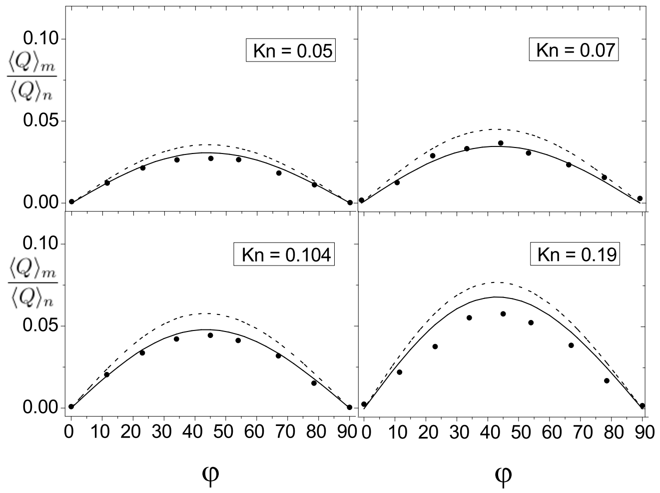

Figure 5.7: Ratio of transverse and longitudinal flow rate as a function of φ for different values of Kn. Points are MD data, the solid and dashed lines represent analytical expressions (5.39) and (5.41).

In the case of simplified model, equation (5.39) can be expressed in terms of accommodation coefficients :

$$\frac{\langle Q\rangle_m}{\langle Q\rangle_n} = \frac{6\mathrm{Kn}\left(\frac{2-\alpha_y}{\alpha_y} - \frac{2-\alpha_x}{\alpha_x}\right)\sin\varphi\cos\varphi}{1 + 6\mathrm{Kn}(\frac{2-\alpha_x}{\alpha_x}\cos^2\varphi + \frac{2-\alpha_y}{\alpha_y}\sin^2\varphi)} \ . \tag{5.41}$$

The ratio $\frac{\langle Q\rangle_m}{\langle Q\rangle_n}$ as a function of φ for different values of Kn is plotted in Fig. (5.7). The results show that the MD data and analytical solutions are closely similar : the ratio is largest at $\varphi = 45°$ and it approaches zero when φ tends to 0° or 90°. However, there are some visible discrepancies between the MD data and analytical results especially, at high Kn number, as it has been explained earlier.

5.4.2 Walls with different slip tensors

In this section, we consider the second case where the two walls are misaligned. The lower wall position is maintained while the upper wall is rotated with an angle 90° in its plane. In this case we have

$$\overline{\mathbf{b}}^+ = \overline{\mathbf{b}}^T \ , \quad \overline{\mathbf{b}}^- = \overline{\mathbf{b}} \ , \tag{5.42}$$

which leads to the following expression of $\mathbf{J}, \mathbf{K}$

$$\begin{aligned} J_x = J_y &= \frac{\overline{b}_y + \overline{b}_x + 4\overline{b}_y\overline{b}_x}{1 + \overline{b}_y + \overline{b}_x} \ , \\ K_x = -K_y &= \frac{\overline{b}_y - \overline{b}_x}{1 + \overline{b}_y + \overline{b}_x} \ . \end{aligned} \tag{5.43}$$

If the estimation (5.25) of $\overline{\mathbf{b}}$ from the accommodation coefficients is adopted, one obtains

$$\begin{aligned} J_x = J_y &= \frac{\mathrm{Kn}(N_y + N_x) + 4\mathrm{Kn}^2 N_y N_x}{1 + N_y + N_x} \ , \\ K_x = -K_y &= \frac{\mathrm{Kn}(N_y - N_x)}{1 + \mathrm{Kn}(N_y + N_x)} \ . \end{aligned} \tag{5.44}$$

Normalizing the slip velocities at two walls u_{sn}^+, u_{sn}^- (at $z = \pm H/2$) with the mid stream velocity u_{n0} (at $z = 0$) yields

$$\begin{aligned} \frac{u_{sn}^+}{u_{n0}} &= \frac{(J_x + K_x)\cos^2\varphi + (J_y + K_y)\sin^2\varphi}{0.5 + J_x\cos^2\varphi + J_y\sin^2\varphi} \ , \\ \frac{u_{sn}^-}{u_{n0}} &= \frac{(J_x - K_x)\cos^2\varphi + (J_y - K_y)\sin^2\varphi}{0.5 + J_x\cos^2\varphi + J_y\sin^2\varphi} \ . \end{aligned} \tag{5.45}$$

Figure (5.8) shows a good agreement between the analytical solutions and MD results: the longitudinal velocity profile is a shifted parabola. As expected, near the wall where the Knudsen layer dominates, the velocity distribution tends to deviate from (5.26). The normalized slip velocities at the upper and lower walls are plotted in Fig.(5.9, 5.10)as a function of φ . As can be seen, the agreement between MD results of fitted slip velocities and predicted solutions (5.45) is also observed at small Kn numbers for both two walls.

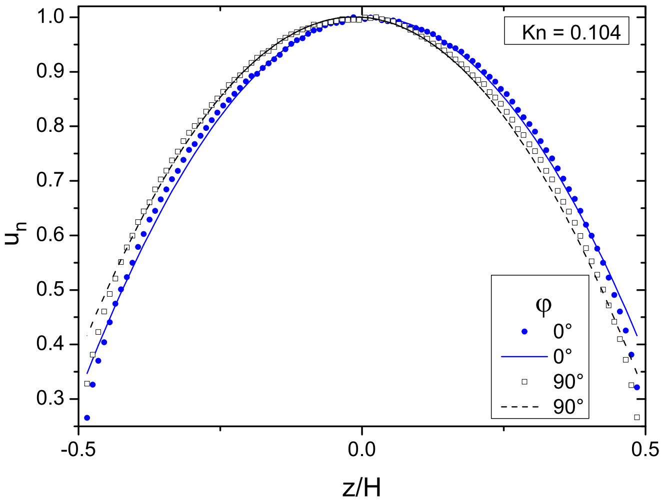

Figure 5.8: Normalized longitudinal velocity profile for two values of φ with $\mathrm{Kn} = 0.104$. Points represent MD data and the solid or dashed lines are for the analytical expression based on (5.26).

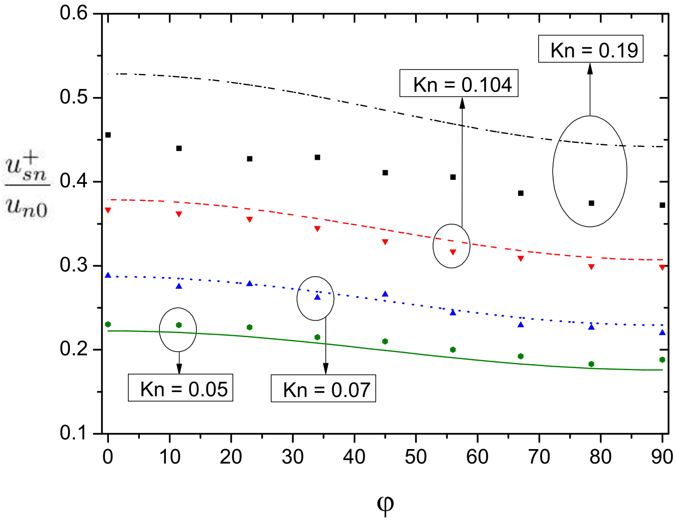

Figure 5.9: Normalized slip velocities at the upper wall as a function of φ for different Kn numbers. The lines represent the analytical expression (5.45) and the points are MD data.

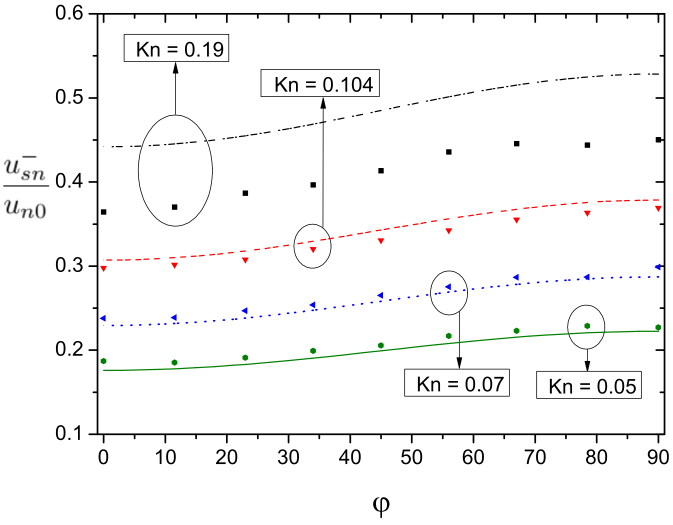

Figure 5.10: Normalized slip velocities at the lower wall as a function of φ for different Kn numbers. The lines represent the analytical expression (5.45) and the points are MD data.

5.4.3 Effects of Knudsen layer and normal tangential coefficient α_z on anisotropic flows

In the micro/nanoscale, the behavior of a gas flow near the wall is dominated by the effect of gas-surface interactions. This area is called the Knudsen layer : a thermodynamically nonequilibrium region extending a distance λ from the wall. Although the Navier-Stokes equations can accurately describe the flow behavior outside the Kn layer, they fail to predict the flow field of the Kn layer, especially for high Kn number [127].

Figures (5.11) and (5.12) show the ratio of real and fitted slip velocities for the case B - walls with different slip tensors. As shown in the figures, the *real* slip velocities are about (0.7 - 0.8) of *fitted* slip velocities at both two walls. These results agree with previous studies [128], which indicated that the ratio of these two slip velocities is approximately equal to 0.8.

Finally, we discuss the validity of slip models based on the two tangential parameters α_x, α_y by considering the effect of α_z on anisotropic flows and on slip behavior of gas at the walls. In previous sections, the normal accommodation coefficient α_z was chosen to be 0.9 for modelling anisotropic surfaces. The case A with identical walls was considered and only α_z is varied while others parameters like α_x, α_y remained unchanged. The variation of slip length with α_z is plotted in Fig.(5.13) for Kn = 0.05 and Kn = 0.104. The slip length increases slightly as α_z increases and the variation is stronger for high Kn. However, the difference between the cases is small (about 2%). We can conclude that slip models based on the two tangential parameters α_x, α_y adequately describe the phenomenon.

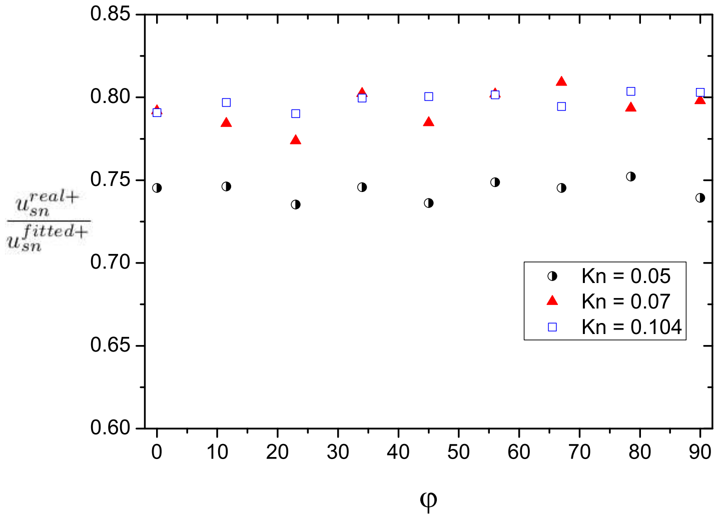

Figure 5.11: Ratio of real and fitted slip velocities at upper wall for different φ-values and Kn numbers.

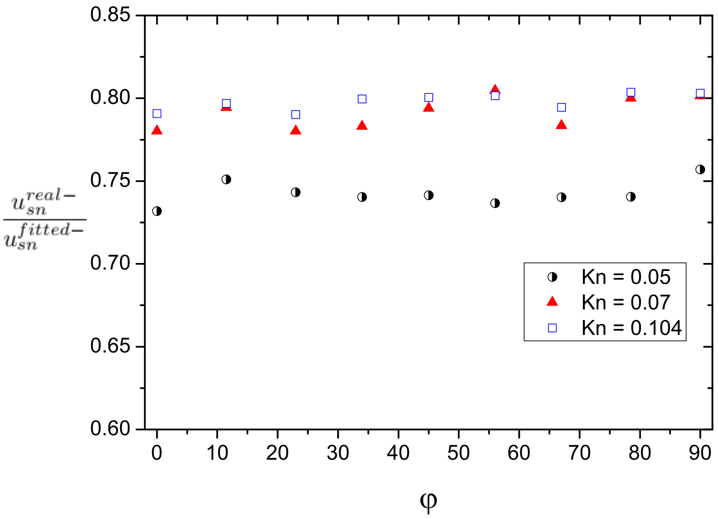

Figure 5.12: Ratio of real and fitted slip velocities at lower wall for different φ-values and Kn numbers.

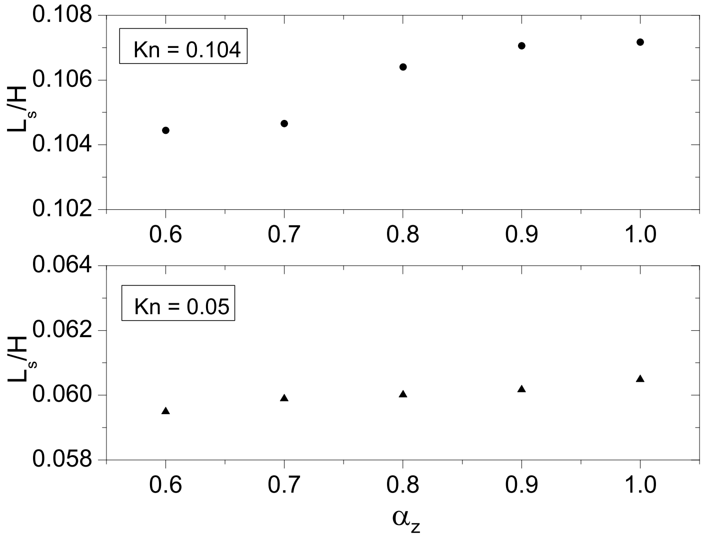

Figure 5.13: Dimensionless slip length L_s/H in term of α_z with $\varphi = 0°$ for Kn $=$ 0.05 and Kn $=$ 0.104.

Conclusion

A multiscale study of boundary conditions at gas-solid interfaces have been conducted by using the Molecular Dynamics method to represent dynamic slip phenomena.

In Chapter 2, both pressure and acceleration driven methods are used to simulate gas flows in slip and transitional regimes. In the former method, a constant gravity - like force is applied to the gas particles. The latter method controls the kinetic pressure difference between the inlet and the outlet. The main novelty lies in the modification of the periodic velocity conditions: the difference in squared velocity between the ingoing and outgoing particles of the simulation domain is maintained constant. Plane Poiseuille flows were modeled and the results compared with approximate analytical solutions of the Navier-Stokes and energy equations reported in the literature.

In Chapter 3, in order to determine which empirical Pt-Ar pairwise potentials proposed in the archival literature may be used in MD simulations, a new Pt-Ar potential has been determined from periodic DFT calculations of the interaction between an argon atom and the solid Pt(111) surface using the CRYSTAL09 code. The energies have then been fitted by a sum of Pt-Ar pairwise inter-atomic van der Waals type terms. The potential parameters, i.e. the interaction energy and the vertical Pt(111)-Ar harmonic vibrational frequency, are in good agreement with experimental data [68, 79]. This potential is very similar to the empirical one determined by Rameseyer *et al.* [82] and Kulginov *et al.* [71]. However this last one has the advantage of considering a physically correct repulsive term. The present and the Kulginov Pt-Ar potentials could be retained for future MD studies involving the Pt(111)-Ar couple. The tangential momentum accommodation coefficient of argon gas colliding with a Pt surface has been determined by MD simulations. Argon atoms impinged on atomistic Pt surface and the post collision information have been collected in order to compute the directional $\sigma_t^{dir}(\theta, \phi)$. We observed that σ_t^{dir} depends on the wall model, and on the Pt-Ar pairwise potential. We found that the well depth and the equilibrium position are the main potential characteristics that influence the value of σ_t^{dir}. The surface is almost isotropic and the average of σ_t^{dir} over θ corresponds to the the gas-solid constant, σ_t, of the Maxwell model. When averaging over the incident angle and using the new potential, a 0.42 - σ_t value has been predicted for a wall temperature T_w=300 K.
The present multi-scale approach combines the advantages of the two computational methods: quantum electronic structure and Molecular Dynamics calculations. Since the accommodation coefficient depends on the interaction strength, accurate determinations of the interaction parameters by accurate approaches are crucial. The Molecular Dynamics approach can reproduce the dynamics of the system and the collision trajectories, which allows to accurately compute the TMAC.

In Chapter 4, we have studied the effects of temperature, surface textures and anisotropy on the σ_t coefficient of Ar gas and Pt(100) surface. The computational model is based on the molecular beam experiments and constructed with the most accurate available potentials and interaction models. Unlike the previous chapter, the multi-body Quantum-Sutton Chen potential is used for the solid walls. Although its implementation is more costly than the harmonic spring potential used in Chapter 3, it better reproduces the surface effects. The MD results show that σ_t is not a simply gas/wall constant, it decreases as the temperature increases and it increases with the roughness of the wall surface. The randomly rough surface obtained from the atomic deposition simulation is also investigated and we observed that, in addition to the roughness height, the in-plane random arrangement of the atoms also plays a significant role on σ_t values. Concerning the anisotropy effect, results on systems with anisotropic surfaces show that σ_t varies significantly with orientation. Effective σ_t coefficients are obtained and compared with models recently reported in the literature.

The last chapter of the thesis examines the gaseous slip flows over anisotropic surfaces from theoretical and numerical points of view. A simplified tensorial slip model based on tangential accommodation tensor is proposed and confronted with MD simulation results. In MD model, a special gas wall interaction based on anisotropic scattering kernels is implemented to mimic the surface anisotropy. The numerical results are shown to be in good agreement with theoretical predictions for the slip flow regime.

Perspectives

The results presented in this thesis could be completed in several directions

- The new pressure driven method using in Chapter 2 proved to be realistic. Hence, it could be applied to many extended problems with non constant axial pressure gradient: flows around obstacles or in rough channels, for example. The method appears thus relevant for modeling compressibility effects as well as temperature variations along the flow direction, a domain still unfulfilled by using MD methods.
- With the data obtained from the molecular beam simulations, we will easily determine the other important coefficients characterizing the exchange between gas and surface such as the normal momentum accommodation coefficient and the energy accommodation coefficient (σ_T). The effects of the gas/wall interaction potential and the morphology of surface on these parameters could be also deduced. On the other hand, knowing the σ_T coefficient facilitate the quantification of the thermal slip in microchannels that not yet considered in this thesis.
- The current beam simulations model monoatomic gases and fixed solid walls. It is also interesting to extend for polyatomic gases and moving walls.
- Although molecular dynamics is a very powerful technique, it is limited to small domains and small time frames. Nowadays, a MD simulation can be performed on systems containing a billion atoms at best, with dimensions up to micron. A possible solution to this limitation is to combine molecular dynamics with continuum mechanics. The results presented in this thesis such as the accommodation coefficients, slip velocities could be used as boundary conditions at gas/solid interface for the continuum mechanics simulation in remainder region where the continuum description is appropriate.

Appendices

Appendix I. Anisotropic scattering kernel

For gas-wall interaction, Dadzie and Meolans [105] proposed an anisotropic scattering kernel $B(\mathbf{v}', \mathbf{v})$ defined by

$$B(\mathbf{v}', \mathbf{v}) = \sum_k \mu_k B_k(\mathbf{v}', \mathbf{v}) \ , \tag{A.1}$$

in which

$$\begin{aligned} &\mu_{ij} = \alpha_i \alpha_j (1 - \alpha_k) \ , \quad \mu_i = \alpha_i (1 - \alpha_j)(1 - \alpha_k) \ , \quad \mu_{ijk} = \alpha_i \alpha_j \alpha_k \ , \\ &\mu_0 = (1 - \alpha_i)(1 - \alpha_j)(1 - \alpha_k) \ , \quad i, j, k = x, y, z \ , \quad i \neq j \neq k \neq i \ . \end{aligned} \tag{A.2}$$

The vectors $\mathbf{v}', \mathbf{v}$ are respectively the arriving velocity and the reflected one and the constants $\alpha_x, \alpha_y, \alpha_z$ are the accommodation coefficients along the directions x, y, z. The elementary kernels B_k are given by the following expressions

$$\begin{aligned} B_0(\mathbf{v}', \mathbf{v}) &= \delta(v_z + v'_z)\delta(v_x - v'_x)\delta(v_y - v'_y) \ , \\ B_{xy}(\mathbf{v}', \mathbf{v}) &= \frac{1}{\pi C_w^2} \delta(v_z + v'_z) e^{-(v_y^2 + v_x^2)/C_w^2} \ , \\ B_{iz}(\mathbf{v}', \mathbf{v}) &= \frac{2}{\sqrt{\pi} C_w^3} v_z \delta(v_j - v'_j) e^{-(v_i^2 + v_z^2)/C_w^2} \ , \\ B_{xyz}(\mathbf{v}', \mathbf{v}) &= \frac{2}{\pi C_w^4} v_z e^{-(v_x^2 + v_y^2 + v_z^2)/C_w^2} \ , \\ B_i(\mathbf{v}', \mathbf{v}) &= \frac{1}{\sqrt{\pi} C_w} \delta(v_z + v'_z)\delta(v_j - v'_j) e^{-v_i^2/C_w^2} \ , \\ B_z(\mathbf{v}', \mathbf{v}) &= \frac{2}{C_w^2} v_z \delta(v_i - v'_i)\delta(v_j - v'_j) e^{-v_z^2/C_w^2} \ , \\ i, j = x, y \ , \quad i \neq j \ , &\quad C_w = \sqrt{2 k_B T_w / m_g} \ , \end{aligned} \tag{A.3}$$

with δ being the delta Dirac function, T_w the wall temperature, k_B the Boltzmann constant and m_g the molecular mass of gaseous particles.
The boundary conditions for particle distribution function $f(\mathbf{v})$ is then defined by

$$v_z f(\mathbf{v}) = \int_{\Omega'} |v'_z| f(\mathbf{v}') B(\mathbf{v}', \mathbf{v}) d\mathbf{v}' \ , \quad \Omega' = \mathbb{R} \times \mathbb{R} \times \mathbb{R}^- \ . \tag{A.4}$$

We use Φ_j^- and Φ_j^+ to denote the incoming flux at the wall of the momentum j component. Then

$$\Phi_j^- = \int_{\Omega'} m |v'_z| v'_j f^-(\mathbf{v}') d\mathbf{v}' \ , \quad \Phi_j^+ = \int_{\Omega} m |v_z| v_j f^+(\mathbf{v}) d\mathbf{v} \ , \quad \Omega' = \mathbb{R} \times \mathbb{R} \times \mathbb{R}^+ \ . \tag{A.5}$$

with f^- and f^+ being the velocity distribution associated with the incident molecules and reflected molecules. Dadzie and Meolans [105] proved the following relation

$$\frac{\Phi_j^- - \Phi_j^+}{\Phi_j^-} = \alpha_j \ , \quad j = x, y, z \ . \tag{A.6}$$

Their model is based on three parameters $\alpha_x, \alpha_y, \alpha_z$ defined along given directions of a system of coordinate. We are interested in the accommodation coefficients in an arbitrary direction. Hence, we consider a family of orthogonal directions $(\mathbf{n}, \mathbf{m})$ obtained by rotating xOy around Oz by an angle φ. Consequently, the n, m-components are related to x, y components by

$$\Phi_n^\pm = \cos\varphi \Phi_x^\pm + \sin\varphi \Phi_y^\pm \ , \quad \Phi_m^\pm = -\sin\varphi \Phi_x^\pm + \cos\varphi \Phi_y^\pm \ . \tag{A.7}$$

Since α_x and α_y are accommodation coefficients, we can deduce the the relation

$$\Phi_n^+ = (1 - \alpha_n)\Phi_n^- + \beta_{nm}\Phi_m^- \ , \quad \Phi_m^+ = (1 - \alpha_m)\Phi_m^- + \beta_{nm}\Phi_n^- \ , \tag{A.8}$$

with

$$\begin{aligned} &\beta_{nm} = (\alpha_x - \alpha_y)\cos\varphi \sin\varphi \ , \\ &\alpha_n = \alpha_x \cos^2\varphi + \alpha_y \sin^2\varphi \ , \\ &\alpha_m = \alpha_y \cos^2\varphi + \alpha_x \sin^2\varphi \ , \end{aligned} \tag{A.9}$$

and compute the accommodation coefficient along any direction n. For example, by setting the component $\Phi_m^- = 0$ (e.g we beam atoms along direction n only), we can recover the expression for α_n in Eq. (4.8). The ratio between the reflected components m, n can also be computed by the expression

$$\Phi_m^+/\Phi_n^+ = \frac{\beta_{nm}}{1 - \alpha_n} = \frac{(\alpha_x - \alpha_y)\cos\varphi \sin\varphi}{1 - \alpha_x \cos^2\varphi - \alpha_y \sin^2\varphi} \ . \tag{A.10}$$

It is clear that for isotropic model $\alpha_x = \alpha_y$, this ratio is always zero for all φ. Thus for anisotropic surface $\alpha_x \neq \alpha_y$, the ratio Φ_m^+/Φ_n^+ is a function of φ, only vanishes at $\varphi = 0^\circ, 90^\circ$. For example, at $\varphi = 45^\circ$, we obtain

$$\Phi_m^+/\Phi_n^+ = \frac{\alpha_x - \alpha_y}{2 - \alpha_x - \alpha_y} \ . \tag{A.11}$$

Appendix II. Slip length tensor

We consider a control surface near and parallel to the immobile wall and study the collisions at this surface. During a unit period of time, there are N gas atoms crossing the surface: N^- atoms go downward and N^+ atoms go upward with tangential velocity $\mathbf{v}_t' = (v_x', v_y')$ and $\mathbf{v}_t = (v_x, v_y)$. The gas velocity $\mathbf{u}_s$ at the wall can be obtained by the average

$$mN\mathbf{u}_s = mN^+\langle \mathbf{v}_t \rangle + mN^-\langle \mathbf{v}_t' \rangle \ . \tag{A.12}$$

The notation $\langle\rangle$ indicates the average over the atoms. It is clear that $mN^+\langle \mathbf{v}_t \rangle$ and $mN^-\langle \mathbf{v}_t' \rangle$ are equivalent to the tangential momentum vector fluxes $\mathbf{\Phi}_t^+$ and $\mathbf{\Phi}_t^-$. Using the linear relation (5.8), we can write

$$mN\mathbf{u}_s = mN^-(2\mathbf{I} - \mathbf{A})\langle \mathbf{v}_t' \rangle \ . \tag{A.13}$$

Since the velocity of a gas atom is unchanged between collisions, it is possible to think that $\langle \mathbf{v}_t' \rangle$ is equal to the velocity average at one mean free path λ from the wall, hence the stream velocity $\mathbf{u}_\lambda$ at that location. By assuming that $N^- = N^+ = N/2$, the slip velocity $\mathbf{u}_s$ can be deduced as follows

$$2\mathbf{u}_s = (2\mathbf{I} - \mathbf{A})\mathbf{u}_\lambda \; . \tag{A.14}$$

We remark that the Taylor development of $\mathbf{u}$ at the wall yields the expression

$$\mathbf{u}_\lambda = \mathbf{u}_s + \lambda \frac{\partial \mathbf{u}}{\partial z} + \frac{\lambda^2}{2} \frac{\partial^2 \mathbf{u}}{\partial z^2} + \ldots \; . \tag{A.15}$$

Considering the first order λ approximation, i.e $\mathbf{u}_\lambda = \mathbf{u}_s + \lambda \frac{\partial \mathbf{u}}{\partial z}$, the final slip equation becomes

$$\mathbf{u}_s = \lambda (2\mathbf{A}^{-1} - \mathbf{I}) \frac{\partial \mathbf{u}}{\partial z} = \lambda \mathbf{N} \frac{\partial \mathbf{u}}{\partial z} \; , \tag{A.16}$$

The term standing before $\frac{\partial \mathbf{u}}{\partial z}$ is equivalent to the slip length tensor $\mathbf{b}$ and identical to (5.23).

List of Figures

List of Tables

List of publications

Refereed journal publications

T. T. Pham, Q. D. To, G. Lauriat, C. Léonard, V. H. Vo. *Effects of surface morphology and anisotropy on the tangential momentum accommodation coefficient between Pt(100) and Ar.* Physical Review E, 86(5), 051201 (2012).

T. T. Pham, Q. D. To, G. Lauriat, C. Léonard. *Tensorial slip theory for gas flows and comparison with molecular dynamics simulations using an anisotropic gas-wall collision mechanism.* Physical Review E, 87, 053012 (2013).

Q. D. To, T. T. Pham, G. Lauriat, C. Léonard. *Molecular Dynamics Simulations of Pressure-Driven Flows and Comparison with Acceleration-Driven Flows.* Advances in Mechanical Engineering, Volume 2012, , ID 580763, doi:10.1155/2012/580763.

C. Leonard, V. Brites, T.T. Pham, Q. D. To, G. Lauriat. *Influence of the Pairwise Potential on the Tangential Momentum Accommodation Coefficient: a Multi-Scale Study applied to the Argon on Pt(111) System.* European Physical Journal B, 86:164 (2013), DOI: 10.1140/epjb/e2013-30809-9.

Refereed conference proceedings

T. T. Pham, Q. D. To, G. Lauriat, C. Leonard. *Multiscale study of gas slip flows in nanochannels.* ASME 2013 4th Micro/Nanoscale Heat and Mass Transfert International Conference (submitted).

T. T. Pham, Q. D. To, G. Lauriat, C. Léonard, V. H. Vo. *Temperature, surface roughness and anisotropy effects on the tangential momentum accomodation coefficient between Pt(100) and Ar.* Proceedings of the 3rd European Conference on Microfluidics. Heidelberg, December 3-5, 2012.

T. T. Pham, Q. D. To, C. Léonard, G. Lauriat, V. Brites. *Tangential momentum accommodation coefficient of Argon on Pt(111): a multi-scale study.* First International Conference on Computational Science and Engineering, Vietnam. December 2011.

Bibliography

[1] P. Tabeling. *Introduction to microfluidics.* OUP Oxford, 2005.

[2] C.-M. Ho F. Tseng, C.-J. Kim. In *ASME Int. Mechanical Engineering Congress and Exposition, Anaheim*, 1988.

[3] H. Struchtrup. *Macroscopic Transport Equations for Rarefied Gas Flows: Approximation Methods in Kinetic Theory.* Springer, 2005.

[4] W. W. Liou and Y. Fang. *Microfluid Mechanics.* McGraw-Hill, 2003.

[5] S. Chapman and T. G. Cowling. *The mathematical theory of non-uniform gases: an account of the kinetic theory of viscosity, thermal conduction and diffusion in gases.* Cambridge university press, 1991.

[6] N. Metropolis, A. W. Rosenbluth, M. N. Rosenbluth, A. H. Teller, and E. Teller. Equation of state calculations by fast computing machines. *The journal of chemical physics*, 21:1087, 1953.

[7] B. J. Alder and T. E. Wainwright. Phase transition for a hard sphere system. *Journal of Chemical Physics*, 27(5):1208–1209, 1957.

[8] G. A. Bird. *Molecular Gas Dynamics and the Direct Simulation of Gas Flows.* Clarendon Press, 1994.

[9] P. L. Bhatnagar, E. P. Gross, and M. Krook. A model for collision processes in gases. i. small amplitude processes in charged and neutral one-component systems. *Physical Review*, 94:511–525, May 1954.

[10] S. Chapman and T. G. Cowling. The mathematical theory of nonuniform gases. 1970.

[11] H. Grad. Principles of the kinetic theory of gases. In *Thermodynamics of Gases*, pages 205–294. Springer, 1958.

[12] G. Karniadakis, A. Beskok, and N. Aluru. *Microflows and Nanoflows: Fundamentals and Simulation.* Springer, New York, 2005.

[13] W. M. Zhang, G. Meng, and X. Wei. A review on slip models for gas microflows. *Microfluidics and Nanofluidics*, 13:845–882, 2012.

[14] B. Y. Cao, J. Sun, M. Chen, and Z. Y. Guo. Molecular momentum transport at fluid-solid interfaces in MEMS/NEMS: A Review. *International Journal of Molecular Sciences*, 10(11):4638, 2009.

[15] C. L. M. H. Navier. Mémoire sur les lois du mouvement des fluides. *Mémoires de Académie Royale des Sciences de Institut de France*, 6:389–440, 1823.

[16] J. C. Maxwell. On stresses in rarified gases arising from inequalities of temperature. *Philosophical Transactions of the Royal Society of London*, 170:231–256, 1879.

[17] M. von Smoluchowski. Über wärmeleitung in verdünnten gasen. *Annual Review of Physical Chemistry*, 64:101–130, 1898.

[18] R. Schamberg. *The fundamental differential equations and the boundary conditions for high speed slip flow, and their application to several specific problems.* PhD thesis, California Institute of Technology, 1947.

[19] S. Albertoni, C. Cercignani, and L. Gotusso. Numerical evaluation of the slip coefficient. *Physics of Fluids*, 6(7):993–996, 1963.

[20] R. G. Deissler. An analysis of second-order slip flow and temperature-jump boundary conditions for rarefied gases. *International Journal of Heat and Mass Transfer*, 7(6):681 – 694, 1964.

[21] S. K. Loyalka. Approximate method in the kinetic theory. *Physics of Fluids*, 14(11):2291–2294, 1971.

[22] Y. T. Hsia and G. A. Domoto. An experimental investigation of molecular rarefaction effects in gas lubricated bearings at ultra-low clearances. Technical report, DTIC Document, 1981.

[23] S. K. Loyalka and K. A. Hickey. Plane poiseuille flow: Near continuum results for a rigid sphere gas. *Physica A: Statistical Mechanics and its Applications*, 160(3):395–408, 1989.

[24] Y. Mitsuya. Modified Reynolds Equation for Ultra-Thin Film Gas Lubrication Using 1.5-Order Slip-Flow Model and Considering Surface Accommodation Coefficient. *Journal of Tribology*, 115(2):289–294, 1993.

[25] L. S. Pan, G. R. Liu, B. C. Khoo, and B. Song. A modified direct simulation monte carlo method for low-speed microflows. *Journal of Micromechanics and Microengineering*, 10(1):21, 2000.

[26] G. E. Karniadakis and A. Beskok. Micro flows- fundamentals and simulation(book). *New York, Springer-Verlag, 2002.*, 2002.

[27] L. Wu and D. B. Bogy. New first and second order slip models for the compressible reynolds equation. *Journal of Tribology*, 125(3):558–561, 2003.

[28] N. G. Hadjiconstantinou. Comment on cercignani second-order slip coefficient. *Physics of Fluids*, 15:2352, 2003.

[29] C. Cercignani and S. Lorenzani. Variational derivation of second-order slip coefficients on the basis of the boltzmann equation for hard-sphere molecules. *Physics of Fluids*, 22(6):062004, 2010.

[30] Q. Li, Y. L. He, G. H. Tang, and W. Q. Tao. Lattice boltzmann modeling of microchannel flows in the transition flow regime. *Microfluidics and Nanofluidics*, 10:607–618, 2011.

[31] C. Cercignani. *The Boltzmann Equation and Its Applications.* Springer-Verlag: New York, NY, USA, 1988.

[32] D. Jie, X. Diao, K. B. Cheong, and L. K. Yong. Navier-Stokes simulations of gas flow in micro devices. *Journal of Micromechanics and Microengineering*, 10(3):372, 2000.

[33] C. Aubert and S. Colin. High-order boundary conditions for gaseous flows in rectangular microducts. *Microscale Thermophysical Engineering*, 5(1):41–54, 2001.

[34] D. A. Lockerby, J. M. Reese, D. R. Emerson, and R. W. Barber. Velocity boundary condition at solid walls in rarefied gas calculations. *Physical Review E*, 70:017303, Jul 2004.

[35] L. Wu. A slip model for rarefied gas flows at arbitrary knudsen number. *Applied Physics Letters*, 93(25):253103, 2008.

[36] R. A. Buckingham. The Classical Equation of State of Gaseous Helium, Neon and Argon. *Proceedings of the Royal Society of London. Series A, Mathematical and Physical Sciences*, 168:264–283, 1938.

[37] A. R. Leach. *Molecular modelling: principles and applications.* Pearson College Division, 2001.

[38] L. Verlet. Computer "experiments" on classical fluids. I. Thermodynamical properties of Lennard-Jones molecules. *Physical Review*, 159(1):98, 1967.

[39] W. G. Hoover. Canonical dynamics: Equilibrium phase-space distributions. *Physical Review A*, 31:1695–1697, Mar 1985.

[40] H. J. C. Berendsen, J. P. M. Postma, W. F. van Gunsteren, A. DiNola, and J. R. Haak. Molecular dynamics with coupling to an external bath. *The Journal of Chemical Physics*, 81(8):3684–3690, 1984.

[41] H. C. Andersen. Molecular dynamics simulations at constant pressure and/or temperature. *The Journal of Chemical Physics*, 72(4):2384–2393, 1980.

[42] X. Yong and L. T. Zhang. Thermostats and thermostat strategies for molecular dynamics simulations of nanofluidics. *The Journal of Chemical Physics*, 138(8):084503, 2013.

[43] A. L. Kuzemsky. Theory of transport processes and the method of the nonequilibrium statistical operator. *International Journal of Modern Physics B*, 21(17):2821–2949, 2007.

[44] J. H. Irving and J. G. Kirkwood. The statistical mechanical theory of transport processes. iv. the equations of hydrodynamics. *Journal of Chemical Physics*, 18:817, 1950.

[45] B. D. Todd, D. J. Evans, and P. J. Daivis. Pressure tensor for inhomogeneous fluids. *Physical Review E*, 52(2):1627, 1995.

[46] D. J. Evans and G. Morriss. *Statistical mechanics of nonequilibrium liquids.* Cambridge University Press, 2008.

[47] D. C. Rapaport. *The Art of Molecular Dynamics Simulation.* Cambridge University Press, 2004.

[48] B. D. Todd and D. J. Evans. Temperature profile for poiseuille flow. *Physical Review E*, 55(3):2800, 1997.

[49] D. K. Bhattacharya and G. C. Lie. Molecular dynamics simulations of nonequilibrium heat and momentum transport in very dilute gases. *Physical Review Letters*, 62(8):897–900, Feb 1989.

[50] J. L. Barrat and L. Bocquet. Large slip effect at a nonwetting fluid-solid interface. *Physical Review Letters*, 82(23):4671–4674, 1999.

[51] Q. D. To, C. Bercegeay, G. Lauriat, C. Léonard, and G. Bonnet. A slip model for micro/nano gas flows induced by body forces. *Microfluidics and Nanofluidics*, 8(3):417–422, 2010.

[52] M. Lupkowski and F. van Swol. Computer simulation of fluids interacting with fluctuating walls. *Journal of Chemical Physics*, 93:737, 1990.

[53] J. Li, D. Liao, and S. Yip. Coupling continuum to molecular-dynamics simulation: Reflecting particle method and the field estimator. *Physical Review E*, 57(6):7259, 1998.

[54] M. Sun and C. Ebner. Molecular-dynamics simulation of compressible fluid flow in two-dimensional channels. *Physical Review A*, 46(8):4813, 1992.

[55] E. B. Arkilic, M. A. Schmidt, and K. S. Breuer. Gaseous slip flow in long microchannels. *Journal of Microelectromechanical Systems*, 6(2):167–178, 1997.

[56] L. D. Landau and E. M. Lifshitz. Fluid mechanics, 1987.

[57] C. Cai, Q. Sun, and I. D. Boyd. Gas flows in microchannels and microtubes. *Journal of Fluid Mechanics*, 589(589):305–314, 2007.

[58] W. G. Hoover, C. G. Hoover, and J. F. Lutsko. Microscopic and macroscopic stress with gravitational and rotational forces. *Physical Review E*, 79(3):036709, 2009.

[59] J. P. Hansen and I. R. McDonald. *Theory of simple liquids.* Academic press, 2006.

[60] M. P. Allen and D. J. Tildesley. *Computer Simulation of Liquids.* Oxford University Press, 1989.

[61] D. Frenkel and B. Smit. *Understanding molecular simulation: from algorithms to applications*, volume 1. Academic Press, 2001.

[62] M. Han and J. S. Lee. Method for calculating the heat and momentum fluxes of inhomogeneous fluids. *Physical Review E*, 70(6):061205, 2004.

[63] Y. Zheng, A. L. Garcia, and B. J. Alder. Comparison of kinetic theory and hydrodynamics for poiseuille flow. *Journal of Statistical Physics*, 109(3):495–505, 2002.

[64] K. Xu. Super-burnett solutions for poiseuille flow. *Physics of Fluids*, 15(7):2077–2080, 2003.

[65] B. Y. Cao, M. Chen, and Z. Y. Guo. Temperature dependence of the tangential momentum accommodation coefficient for gases. *Applied Physics Letters*, 86:091905, 2005.

[66] G. W. Finger, J. S. Kapat, and A. Bhattacharya. Molecular dynamics simulation of adsorbent layer effect on tangential momentum accommodation coefficient. *Journal of Fluids Engineering*, 129:31–39, 2007.

[67] J. E. Hurst, L. Wharton, K. C. Janda, and D. J. Auerbach. Direct inelastic scattering Ar from Pt(111). *Journal of Chemical Physics*, 78(3):1559–1581, 1983.

[68] M. Head-Gordon, J. C. Tully, C. T. Rettner, C. B. Mullins, and D. J. Auerbach. On the nature of trapping and desorption at high surface temperatures. Theory and experiments for the Ar–Pt (111) system. *Journal of Chemical Physics*, 94:1516, 1991.

[69] R. J. Smith, A. Kara, and S. Holloway. A molecular dynamics study for the trapping and scattering of Ar/Pt(111). *Surface Science*, 281(3):296 – 308, 1993.

[70] R. J. W. E. Lahaye, S. Stolte, A. W. Kleyn, R. J. Smith, and S. Holloway. Site dependent energy loss in Ar scattering from Pt(111). *Surface Science*, 307-309:187–192, January 1st 1994.

[71] D. Kulginov, M. Persson, C. T. Rettner, and D. S. Bethune. An empirical interaction potential for the Ar/Pt (111) system. *Journal of Chemical Physics*, 100(19):7919–7927, 1996.

[72] M. Svanberg, N. Markovic, and J. B. C. Pettersson. Scattering of large argon clusters from a Pt(111) surface with low collision velocities. *Chemical Physics*, 220(1):137–153, 1997.

[73] T. Kimura S. Maruyama. A molecular dynamics simulation of a bubble nucleation on solid surface. *Proceedings of the 5th ASME-JSME Thermal Engineering Joint Conference, San Diego, USA*, 1999.

[74] S. Maruyama and T Kimura. A study on thermal resistance over a solid-liquid interface by the molecular dynamics method. *Thermal Science and Engineering*, 7:63–68, 1999.

[75] K. Yamamoto. Slip flow over a smooth platinum surface. *JSME International Journal Series B Fluids and Thermal Engineering*, 45(4):788–795, 2002.

[76] P. Spijker, A. J. Markvoort, S. V. Nedea, and P. A. J. Hilbers. Computation of accommodation coefficients and the use of velocity correlation profiles in molecular dynamics simulations. *Physical Review E*, 81(1):011203, Jan 2010.

[77] J. Sun and Z. X. Li. Three-dimensional molecular dynamic study on accommodation coefficients in rough nanochannels. *Heat Transfer Engineering*, 32(7-8):658–666, 2011.

[78] S. K. Prabha and S. P. Sathian. Molecular-dynamics study of poiseuille flow in a nanochannel and calculation of energy and momentum accommodation coefficients. *Physical Review E*, 85(4):041201, 2012.

[79] P. Zeppenfeld, U. Becher, K. Kern, R. David, and G. Comsa. Van Hove anomaly in the phonon dispersion of monolayer Ar/Pt (111). *Physical Review B*, 41(12):8549, 1990.

[80] P. Zeppenfeld, U. Becher, K. Kern, and G. Comsa. Structure of monolayer Ar on Pt (111): Possible realization of a devil staircase in two dimensions. *Physical Review B*, 45(10):5179, 1992.

[81] M. Svanberg and J. B. C. Pettersson. Survival of noble gas clusters scattering from hot metal surfaces. *Chemical Physics Letters*, 263(5):661–666, 1996.

[82] M. Han. Thermally-driven nanoscale pump by molecular dynamics simulation. *Journal of Mechanical Science and Technology*, 22(1):157–165, 2008.

[83] R. Dovesi, R. Orlando, B. Civalleri, C. Roetti, V. R. Saunders, and C. M. Zicovich-Wilson. CRYSTAL: a computational tool for the ab initio study of the electronic properties of crystals. *Zeitschrift für Kristallographie*, 220(5/6/2005):571–573, 2005.

[84] J. P. Perdew, A. Ruzsinszky, G. I. Csonka, O. A. Vydrov, G. E. Scuseria, L. A. Constantin, X.n Zhou, and K. Burke. Restoring the density-gradient expansion for exchange in solids and surfaces. *Physical Review Letters*, 100(13):136406, 2008.

[85] K. Doll. CO adsorption on the Pt (111) surface: a comparison of a gradient corrected functional and a hybrid functional. *Surface science*, 573(3):464–473, 2004.

[86] R. Nada, J. B. Nicholas, M. I. McCarthy, and A. C. Hess. Basis sets for ab initio periodic Hartree-Fock studies of zeolite/adsorbate interactions: He, Ne, and Ar in silica sodalite. *International Journal of Quantum Chemistry*, 60(4):809–820, 1996.

[87] K. A. Gschneidner Jr. Physical properties and interrelationships of metallic and semimetallic elements. *Solid State Physics*, 16:275–426, 1964.

[88] E. A. Colbourn and A. E. Douglas. The spectrum and ground state potential curve of Ar2. *Journal of Chemical Physics*, 65(5):1741–1745, 1976.

[89] D. Eichenauer, U. Harten, J. P. Toennies, and V. Celli. Interaction potential for one-phonon inelastic he–cu (111) and he–ag (111) scattering. *Journal of Chemical Physics*, 86:3693, 1987.

[90] P. Yi, D. Poulikakos, J. Walther, and G. Yadigaroglu. Molecular dynamics simulation of vaporization of an ultra-thin liquid argon layer on a surface. *International Journal of Heat and Mass Transfer*, 45(10):2087–2100, 2002.

[91] T. Schlick. *Molecular Modeling and Simulation: an Interdisciplinary Guide*. Springer Verlag, 2010.

[92] A. Agrawal and S. V. Prabhu. Survey on measurement of tangential momentum accommodation coefficient. *Journal of Vacuum Science & Technology A: Vacuum, Surfaces, and Films*, 26(4):634–645, 2008.

[93] S. M. Cooper, B. A. Cruden, M. Meyyappan, R. Raju, and S. Roy. Gas transport characteristics through a carbon nanotubule. *Nano Letters*, 4(2):377–381, 2004.

[94] E. B. Arkilic, K. S. Breuer, and M. A. Schmidt. Mass flow and tangential momentum accommodation in silicon micromachined channels. *Journal of Fluid Mechanics*, 437:29–43, 2001.

[95] Q. D. To, T. T. Pham, G. Lauriat, and C. Léonard. Molecular dynamics simulations of pressure-driven flows and comparison with acceleration-driven flows. *Advances in Mechanical Engineering*, 2012, 2012.

[96] C. T. Rettner. Thermal and tangential-momentum accommodation coefficients for N 2 colliding with surfaces of relevance to disk-drive air bearings derived from molecular beam scattering. *IEEE Transactions on Magnetics*, 34(4):2387–2395, 1998.

[97] M. Kalweit and D. Drikakis. Multiscale methods for micro/nano flows and materials. *Journal of Computational and Theoretical Nanoscience*, 5(9):1923–1938, 2008.

[98] M. Kalweit and D. Drikakis. Coupling strategies for hybrid molecularcontinuum simulation methods. *Journal of Mechanical Engineering Science*, 222(5):797–806, 2008.

[99] M. Kalweit and D. Drikakis. On the behaviour of fluidic material at molecular dynamics boundary conditions used in hybrid molecular-continuum simulations. *Molecular Simulation*, 36(9):657–662, 2010.

[100] M. Z. Bazant and O. I. Vinogradova. Tensorial hydrodynamic slip. *Journal of Fluid Mechanics*, 613:125–134, 2008.

[101] L. Bocquet and J. L. Barrat. Hydrodynamic boundary conditions, correlation functions, and kubo relations for confined fluids. *Physical Review E*, 49:3079–3092, Apr 1994.

[102] L. Bocquet and J. L. Barrat. Flow boundary conditions from nano-to micro-scales. *Soft Matter*, 3(6):685–693, 2007.

[103] F. Feuillebois, M. Z. Bazant, and O. I. Vinogradova. Effective slip over superhydrophobic surfaces in thin channels. *Physical Review Letters*, 102(2):026001, Jan 2009.

[104] F. Feuillebois, M. Z. Bazant, and O. I. Vinogradova. Transverse flow in thin superhydrophobic channels. *Physical Review E*, 82(5):055301, Nov 2010.

[105] S. K. Dadzie and J. G. Meolans. Anisotropic scattering kernel: Generalized and modified Maxwell boundary conditions. *Journal of Mathematical Physics*, 45:1804, 2004.

[106] C. Léonard, V. Brites, T. T. Pham, Q. D. To, and G. Lauriat. Influence of the pairwise potential on the tangential momentum accommodation coefficient: a multiscale study applied to the argon on Pt(111) system. *The European Physical Journal B*, 86(4):1–11, 2013.

[107] A. P. Sutton and J. Chen. Long-range Finnis–Sinclair potentials. *Philosophical Magazine Letters*, 61(3):139–146, 1990.

[108] S. K. R. S. Sankaranarayanan, V. R. Bhethanabotla, and B. Joseph. Molecular dynamics simulation study of the melting and structural evolution of bimetallic Pd-Pt nanowires. *Physical Review B*, 74(15):155441, 2006.

[109] G. Arya, H. C. Chang, and E. J. Maginn. Molecular simulations of Knudsen wall-slip: effect of wall morphology. *Molecular Simulation*, 29:697–709(13), 2003.

[110] N. Asproulis and D. Drikakis. Wall-mass effects on hydrodynamic boundary slip. *Physical Review E*, 84:031504, Sep 2011.

[111] N. Asproulis and D. Drikakis. Boundary slip dependency on surface stiffness. *Physical Review E*, 81:061503, Jun 2010.

[112] B. Bhushan. *Modern Tribology Handbook*, volume 1. CRC, 2001.

[113] A. Majumdar and B. Bhushan. Role of fractal geometry in roughness characterization and contact mechanics of surfaces. *Journal of Tribology*, 112:205, 1990.

[114] B. B. Mandelbrot. *The Fractal Geometry of Nature*. W. H. Freeman, 1983.

[115] B. B. Mandelbrot, D. E. Passoja, and A. J. Paullay. Fractal character of fracture surfaces of metals. *Nature*, 308:721–722, 1984.

[116] V. V. Hoang and Q. D. To. Free surface effects on thermodynamics and glass formation in simple monatomic supercooled liquids. *Physical Review B*, 84(17):174204, 2011.

[117] T. T. Pham, Q. D. To, G. Lauriat, C. Léonard, and V. V. Hoang. Effects of surface morphology and anisotropy on the tangential-momentum accommodation coefficient between Pt(100) and Ar. *Physical Review E*, 86:051201, Nov 2012.

[118] C. Cercignani and M. Lampis. Kinetic models for gas-surface interactions. *Transport Theory and Statistical Physics*, 1(9):101–114, 1971.

[119] C. Cercignani. *Rarefied gas dynamics: from basic concepts to actual calculations*, volume 21. Cambridge University Press, 2000.

[120] R. G. Lord. Some extensions to the Cercignani-Lampis gas-surface scattering kernel. *Physics of Fluids A*, 3(4):706–710, 1991.

[121] S. K. Dadzie and J. G. Meolans. Temperature jump and slip velocity calculations from an anisotropic scattering kernel. *Physica A*, 358:328 – 346, 2005.

[122] D. L. Morris, L. Hannon, and A. L. Garcia. Slip length in a dilute gas. *Physical Review A*, 46(8):5279–5281, 1992.

[123] A. V. Belyaev and O. I. Vinogradova. Effective slip in pressure-driven flow past super-hydrophobic stripes. *Journal of Fluid Mechanics*, 652:489–499.

[124] N. V. Priezjev. Molecular diffusion and slip boundary conditions at smooth surfaces with periodic and random nanoscale textures. *Journal of Chemical Physics*, 135(20):204704, 2011.

[125] O. I. Vinogradova and A. V. Belyaev. Wetting, roughness and flow boundary conditions. *Journal of Physics: Condensed Matter*, 23:184104, 2011.

[126] J. Zhou, A. V. Belyaev, F. S., and O. I. Vinogradova. Anisotropic flow in striped superhydrophobic channels. *Journal of Chemical Physics*, 136(19):194706, 2012.

[127] N. Dongari, Y. Zhang, and J. M. Reese. Modeling of knudsen layer effects in micro/nanoscale gas flows. *Journal of Fluids Engineering*, 133(7):071101, 2011.

[128] D. A. Lockerby, J. M. Reese, and M. A. Gallis. A wall-function approach to incorporating Knudsen-layer effects in gas micro flow simulations. *AIP Conference Proceedings*, 762(1):731–736, 2005.